Rydberg spectroscopy and dressing in an ultracold strontium gas

JACKSON, NIAMH,CHRISTINA

Rydberg spectroscopy and dressing in an ultracold strontium gas

Niamh Jackson

A thesis submitted in partial fulfilment
of the requirements for the degree of
Doctor of Philosophy

Department of Physics
Durham University

Rydberg spectroscopy and dressing in an ultracold strontium gas

Niamh Jackson

This thesis describes Rydberg spectroscopy and dressing experiments in an ultracold strontium gas. The strontium atoms are cooled to sub-μK temperatures in a narrowline magneto-optical trap, where Rydberg atoms are created using a two-photon excitation scheme. This required the development of a high-power ultraviolet laser system at 319 nm. The laser has a large tuning range for access to triplet Rydberg states from principal quantum numbers of 35 to > 300. By performing Rydberg spectroscopy in a magneto-optical trap, we show that narrow spectra can be obtained where the line centre is determined to ~ 10 kHz. A frequency comb is then employed to make absolute frequency measurements of optical transitions to accuracies of < 2 MHz. Techniques are outlined for improving the accuracy further, showing that overall uncertainties on the order of 10 kHz can be obtained. The reliable measurement of Rydberg levels is important for studying the variation in quantum defect across Rydberg series, and hence improving the accuracy of atomic models.

In this work we also develop a novel system in which to realise Rydberg dressing. By resonantly coupling the excited state of the cooling transition to a high lying Rydberg state, we create a Rydberg-dressed magneto-optical trap. We demonstrate that the atoms acquire Rydberg properties, while undergoing continuous cooling at ~ 1 μK. The lifetime of the trap is proved to be sufficiently long to observe interactions, however the interaction strength is currently limited by the non-uniform spatial profile of the dressing beam. Straightforward methods to overcome this limitation are presented. As such this work should lead to future experiments, whereby tuneable long-range interactions can be observed in the dynamics of the dressed magneto-optical trap.

Contents

List of Figures

List of Tables

Declaration

I confirm that no part of the material offered has previously been submitted by myself for a degree in this or any other University. Where material has been generated through joint work, the work of others has been indicated.

Niamh Jackson

Durham, October 9, 2018

Acknowledgments

I am extremely grateful to all of my colleagues, friends and family for their support during my time as a Ph.D. student. First and foremost, I offer my sincerest thanks to my supervisor Matt Jones, as without his encouragement, patience and knowledge this thesis would not have been possible.

I was lucky to work with a variety of amazing people during my time on the strontium experiment. I would like to thank Liz Bridge and Dan Sadler for introducing me to the experiment, and showing me the ropes. Both Alistair Bounds and Ryan Hanley have been an absolute pleasure to work with. A lot of the work in this thesis would not have been possible without Alistair, and he always had ideas for any technical problem I faced in the lab. Ryan was a constant source of optimism in my final year, and is currently bringing the experiment to exciting new places. Paul Huillery was always encouraging, and his help in the lab was invaluable for my last few months of data taking. I would also like to thank Riccardo Faoro for all his help on the project. The entire research group of AtMol has been a lovely place to work and I would like to give an all inclusive thanks to everyone. Specifically I would like to thank Teodora for her support and friendship. I hope to be able to provide you with the same level of support as you write up your thesis.

None of this with be possible without my loving family to who I would like to express my deepest gratitude. My parents, who give me continuous support in all that I attempt. I would never have gotten this far without their belief in me. My sisters, Aoife, Clíona and Louise, whose frequent calls always cheer me up. I would also like to thank Tony, Vessy, Alex and Antony for all their support.

Last, but definitely not least, I would like to thank my husband Bobby. I am immensely grateful for all you have done over the past few years. For moving to Durham without a second thought, your patience when I was frustrated, for being there whenever I needed you, and taking my mind off work when I needed it most.

Chapter 1

Introduction

1.1 General Introduction

Rydberg atom physics has been a subject of continued interest for more than one hundred years. In 1890, Johannes Rydberg derived the well known Rydberg formula in order to describe the spectrum of atoms beyond hydrogen [1]. The field then began with the spectroscopical observations of Rydberg atoms [2], and since this the developments in experimental techniques has allowed for a more complete understanding of their structure [3].

A number of recent advances in Rydberg physics have resulted in a revival of activity in this research community. In particular, major developments in laser cooling and trapping techniques opened up new avenues of research using Rydberg atoms [4, 5]. The renewed interest is driven by the long-range interactions that exist between Rydberg atoms, leading to ideal systems in which to investigate few- and many-body effects. In an ultracold atomic gas the atoms are essentially frozen during the radiative lifetime of the Rydberg states [6]. As such the strong interactions between the Rydberg atoms exceeds their kinetic energy, allowing for the direct observation of interaction effects. Consequently, ultracold Rydberg systems have been exploited for a variety of applications including many-body quantum simulations [7–9], quantum non-linear optics [10–12] and quantum information processing [13–17].

While the strong interactions between Rydberg atoms produce suitable systems for studying interacting dipolar gases, the experimental realizations mentioned above have focused on timescales shorter than the lifetime of the Rydberg state. The lifetime of Rydberg atoms is typically of the order of tens of microseconds, which is much shorter than the dynamical timescale of ultracold atom experiments. For this reason Rydberg dressing has been proposed as method for overcoming this mismatch in timescales. The technique involves weakly dressing an atomic ground state with a small fraction ϵ of the Rydberg state, enhancing the overall lifetime of the system by by ϵ^{-2} [18, 19]. Theory predicts that this approach could lead to a number of interesting phenomena, including the realization of supersolids [18–20], three dimensional solitons [21], the creation of exotic spin and magnetic states [22, 23], and spin-squeezing for enhanced metrology [24, 25]. Rydberg dressing has been demonstrated for two-atoms [26] and in a two-dimensional lattice [27, 28]. However both these systems use limited dimensionality for controlled interactions, and it has proved more challenging to observe Rydberg dressed interactions away from this regime, in three-dimensional, disordered systems [29–32].

In this thesis an alternative and novel scheme for Rydberg dressing is introduced, using the properties that are unique to divalent atoms. Therefore we now provide an overview of these properties, which are useful for our experiments.

1.2 Strontium Rydberg Atoms

While many of the already mentioned advances in Rydberg physics have been achieved in alkali-metal atoms, there is an increased interest in using ultracold alkaline-earth Rydberg atoms, such as strontium [33]. This is due to the fact that they offer opportunities of studying different aspects of Rydberg physics, as should become clear throughout this work. An energy level diagram for strontium showing the main cooling and Rydberg excitation transitions is presented in Fig. 1.1.

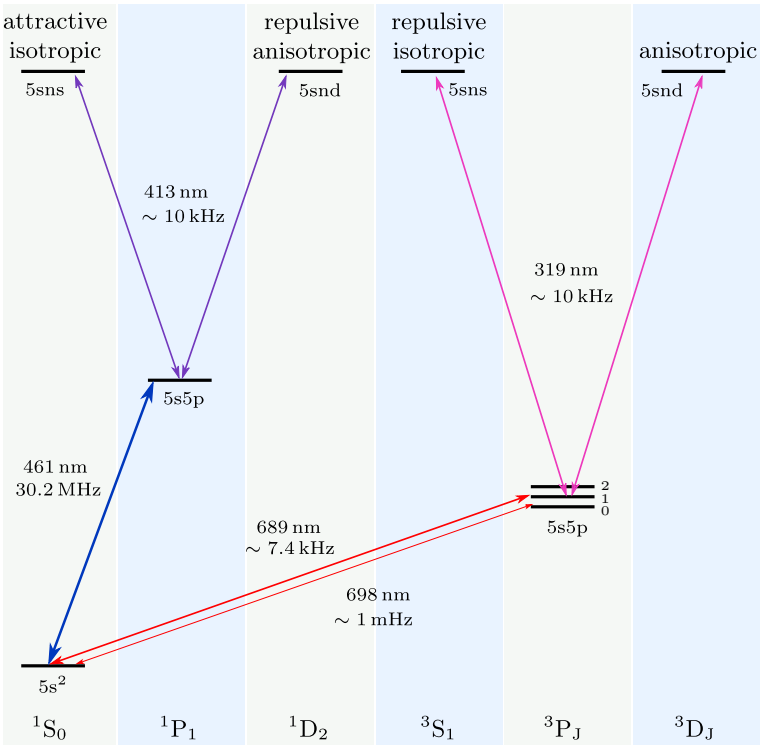

Figure 1.1: Atomic energy level scheme in strontium. Here we show the main cooling transitions at 461 nm and 689 nm, the clock transition at 698 nm, and the Rydberg excitation schemes via the 5s5p ^{1}P$_1$ state and 5s5p ^{3}P$_1$ state.

An important property of strontium for the work in this thesis, is that the atom has two valence electrons. This divalent nature means that strontium supports both singlet and triplet electronic spin states. Although the transitions between the singlet and triplet states are forbidden, state mixing effects make them weakly allowed. For pure LS coupling, the three 5s5p ^{3}P$_J$ states are forbidden, however spin-orbit interactions breaks down the LS coupling, allowing for mixing of states with the same total angular momentum, J, and different spin, S. The $^3P_0$ state is not affected by the spin-orbit interaction, and as such the $^1S_0 \rightarrow {}^3P_0$ clock transition is completely forbidden, unless a magnetic field is applied, mixing a fraction of the $^3P_1$ state into the $^3P_0$ state [34].

In our experiments the 5s^2 ^{1}S$_0$ $\rightarrow$ 5s5p ^{3}P$_1$ transition is used for creating an ultracold sample of atoms. As the 5s5p ^{3}P$_1$ state has a linewidth of only $2\pi\times7.4$ kHz, it allows for optical cooling in a narrow-line magneto-optical

trap (MOT), where minimum temperatures of 400 nK have been achieved [35].

Another advantage that arises from the presence of two valence electrons, is the possibility to access both singlet and triplet Rydberg series. As shown in Fig. 1.1 these Rydberg series feature a variety of attractive or repulsive interactions. The benefit of this for our experiments is that it allows a choice in the type of interactions we require for a given experiment.

The second valence electron also leads to the possibility of using alternative Rydberg detection schemes. The divalent structure of strontium allows the formation of doubly excited states, leading to rapid ionisation. This ionisation technique allows detection of Rydberg atoms with spatial, temporal, and atomic-state resolution [36]. Also, the presence of the core electron allows optical detection of Rydberg atoms as demonstrated in [37].

Finally, as presented in [38] the polarizability of the extra valence electron could be used to realize a magic-wavelength optical lattice for both ground state and Rydberg atoms. In the fututre, such a system could be used to study excitation transfer between Rydberg atoms [39].

1.3 Context of this Work

The aim of this thesis is to use the properties unique to divalent atoms for studying Rydberg physics in an ultracold strontium gas. The majority of previous work in our group has been conducted on the singlet Rydberg transitions, and here we move to performing experiments on the triplet Rydberg states. In order to perform spectroscopic measurements of these states, a laser system operating at 319 nm was developed. An optical frequency comb was used for absolute frequency measurements of the Rydberg energy levels. The development of femtosecond frequency combs revolutionized the field of high-resolution spectroscopy [40], enabling better measurement precision and accuracy. As combs are now commercially available, they have become routine instruments for performing precision spectroscopy, while the extension of frequency combs to shorter wavelengths [41] has made it possible to

measure absolute frequencies of Rydberg states with sub-MHz precision [42–45]. For the triplet Rydberg series in strontium, we find that very narrow Rydberg spectra can be obtained, owing to the kHz linewidth transitions. This allows high precision measurements of the Rydberg states, on the order of a few kHz.

Previously measured strontium Rydberg energy levels were predominantly taken during the 1970's and 80's, and it is therefore useful to revisit such measurements following such significant advances in the field of laser spectroscopy. A review of the literature shows that measurements of the energy levels of strontium are available for the triplet S, P, D and F states [46–49, 49–52]. The highest precision measurements are taken at low n, giving errorbars of $\sim$100 MHz on the reported values, with other measurements having much greater errors.

There are a number of motivations for taking improved absolute measurements of strontium Rydberg series. Firstly, the updated measurements can be used to test the theories which describe the Rydberg states in multi-electron atoms, where the highly correlated doubly excited perturber states complicate the picture [53, 54]. The measured energies were previously fitted with the Rydberg-Ritz formula [53] to obtain the zero-field energy at all principal quantum numbers. Therefore more accurate measurements of the energies in strontium would produce tighter constraints on the fitting parameters. The need for this reduced uncertainty was mentioned in [55], for comparing experimental and calculated Stark maps, in an effort to reduce stray DC fields. Finally, enhanced measurements of the Rydberg states could also lead to prospects of testing new physics e.g. beyond standard model forces [56].

Following spectroscopy and characteristation of the triplet Rydberg states, we move on to consider the possibility of Rydberg dressing in strontium. Previous work of dressing in strontium was studied in [29, 57]. A two-photon dressing scheme was used, where the ground state was coupled to the Rydberg state via the 5s5p ^{3}P$_1$ intermediate state. This configuration was found to produce fast loss mechanisms, similar to other ground state

dressing experiments [30–32]. For this reason, an alternative dressing scheme is presented in this work for the observation of dressed interactions. Here we use the $5s^2\ {}^1S_0 \rightarrow 5s5p\ {}^3P_1$ transition line in strontium to perform Rydberg dressing directly in a MOT. The excited MOT transition is coupled to the Rydberg state, and results in a system where the dressed interaction strength can be of similar magnitude to both the transition linewidth and kinetic energy of the atoms. As Rydberg dressing is applied to an excited state undergoing spontaneous emission, we find the trap lifetime is not limited by the same loss mechanisms seen in other ground-state dressing experiments. As such the work presented in this thesis represents important advances for the study of Rydberg atoms in alkaline-earth elements. A number of future applications should arise directly from this work. This includes enhanced precision spectroscopy, along with a clear method for producing a Rydberg-dressed system in which to study many-body physics. Furthermore, by building on the dressing scheme outlined in this thesis, a similar approach could be used for generating squeezed states for enhanced precision in atomic clocks [24].

1.4 Thesis Outline

The work presented in this thesis first required the production of a cold gas of strontium atoms. For excitation of the cold atoms to the triplet Rydberg series in strontium, a laser source at 319 nm was then constructed. As previous work took place on the singlet Rydberg series, this laser system was initially used in order to identify and characterise triplet Rydberg states. Through performing Rydberg spectroscopy in the cold atom cloud, we show it is possible to measure the Rydberg energy levels to a significantly higher accuracy compared to former measurements. Following this we move towards the prospect of Rydberg dressing in a MOT. Here we show promising steps towards creating a system in which both laser cooling and long-rage interactions are present. The general outline is as follows:

- In chapter 2 background information applicable to the work in this thesis is provided. This includes a discussion on narrow-line laser cooling dynamics, along with an introduction to Rydberg physics and Rydberg dressing.

- In chapter 3 the experimental setup is introduced, along with the main techniques used for acquiring experimental data.

- In chapters 4 and 5 we focus on Rydberg spectroscopy. Here we detail the apparatus used for performing high precision measurements of the Rydberg states, methods for characterising the Rydberg states, and finally our technique for obtaining frequency measurements. Part of the results presented in these chapters are available in [58, 59]

- Chapter 6 gives details on Rydberg dressing a narrow-line MOT, presenting our experimental results. These results have been published in [60].

- Finally in chapter 7 we conclude the main findings of this thesis and give an outlook towards future work.

1.5 Publications

Below are the two main publications arising from this work:

- E. M. Bridge, N. C. Keegan, A. D. Bounds, D. Boddy, D. P. Sadler, and M. P. A. Jones, *Tunable CW UV laser with* $< 35\,\mathrm{khz}$ *absolute frequency instability for precision spectroscopy of Sr Rydberg states*, Opt. Express, 24(3), 2281-2292 (2016).

- A. D. Bounds, N. C. Jackson, R. K. Hanley, R. Faoro, E. M. Bridge, P. Huillery, and M. P. A. Jones, *Rydberg-Dressed Magneto-optical Trap*, Physical Review Letters, 120, 183401 (2018).

Chapter 2

Background

This chapter aims to provide the background information necessary for the experiments conducted throughout this thesis. Firstly, narrow line cooling dynamics are discussed in detail, due to the significant differences compared to conventional Doppler cooling. We then give a brief overview of Rydberg physics, before focusing on Rydberg dressing techniques. Finally, the discussion then leads into Rydberg-dressing a narrow line MOT, as the goal of this work was to find a regime where the long-range interaction between Rydberg dressed atoms influence the MOT dynamics.

2.1 Laser Cooling Strontium

For the experiments outlined in this thesis, strontium is first cooled to temperatures of a few hundred nK in a magneto-optical trap (MOT). The MOT is formed on the narrow linewidth 689 nm transition, where the cooling dynamics on this narrow transition are much different from conventional Doppler cooling. This section therefore reviews the dynamics of narrow line cooling, and then introduces a semi-classical Monte Carlo simulation which we use for modeling the narrow-line MOT.

2.1.1 Narrowline Cooling Dynamics

Laser cooling and trapping in a MOT is a well established technique, where the experimental configuration for narrow-line MOTs is the same as for a conventional MOT. The main difference in cooling dynamics arises from the ratio $\eta = \Gamma/\omega_{\mathrm{r}}$, where Γ is the natural linewidth of the cooling transition and $\omega_{\mathrm{r}} = 4\pi^2\hbar/2m\lambda^2$ is the frequency shift due to the atomic recoil following absorption or emission of a photon.

In a conventional MOT that operates on strong dipole-allowed transition $\eta >> 1000$, whereas in comparison for narrow-line MOTs (operating on dipole-forbidden transitions) the value $\eta \sim 1$. The consequence of this is that a single photon recoil can dominate the MOT dynamics. The minimal attainable temperature is then set by the recoil temperature, rather than the Doppler temperature [61].

In general the narrow line trap dynamics can be separated into three different regimes. These regimes depend on the scaled detuning $|\delta|/\Gamma_{\mathrm{E}}$ [62], where δ is the laser detuning and Γ_{E} is the power broadened linewidth,

$$\Gamma_E = \Gamma\sqrt{1+s}. \tag{2.1}$$

Here the saturation parameter, $s = I/I_{sat}$, where I is the single beam intensity of the cooling light and I_{sat} the transition saturation intensity.

Regime I is most similar to a conventional MOT, and occurs when $|\delta|/\Gamma_{\mathrm{E}} \sim 1$ and $s >> 1$. Here atoms scatter from all MOT beams and the cloud forms close to the quadrupole centre. In this case the power-broadened linewidth determines the temperature.

Regime II considers the case for $|\delta|/\Gamma_{\mathrm{E}} >> 1$ and $s > 1$. Here it is helpful to consider the region in which atoms interact with the MOT light. The far-detuned light will only be resonant with the atomic transition in regions where the Zeeman shift induced by the quadrupole magnetic field balances the detuning:

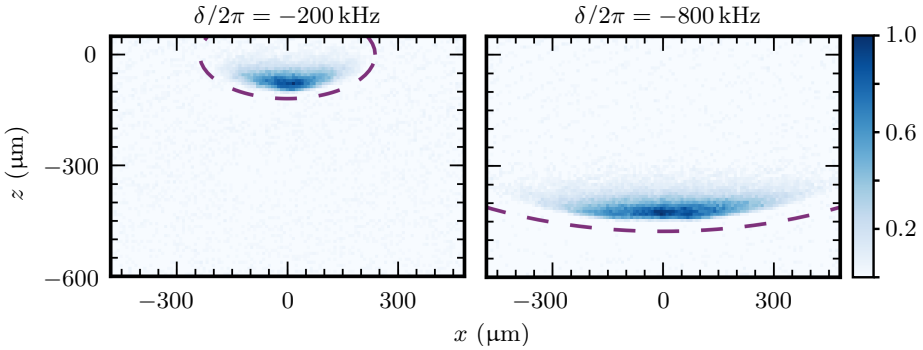

Figure 2.1: Absorption images of the MOT at two different values of δ operating in the regime II. The dashed purple line shows the resonance condition where δ balances the Zeeman shift. The colourbar shows the optical depth (OD) normalised by the peak OD.

$$\delta = m_j g_j \mu_\mathrm{B} B \tag{2.2}$$

where the Lande g-factor $g_j = 1.5$ and μ_B is the Bohr magneton. The resulting resonance condition is an elliptical shell around the quadrupole centre. Additionally the maximum scattering force ($\Gamma\hbar k/2m$) is ~ 16 times that of gravity. Therefore the atoms fall under gravity until the resonance condition is met, and the atoms predominately interact with the MOT beam which directly opposes gravity. This results in an elliptical shaped cloud whose position and shape is largely determined by δ. Fig. 2.1 shows a narrow-line MOT, operating in regime II, for two different detunings. Here it is clear that by increasing δ a shape change is observed along with a shift to lower vertical positions.

Finally, regime III occurs when $|\delta|/\Gamma_\mathrm{E} >> 1$ and $s \leq 1$. The sensitivity to detuning and magnetic field gradient is similar to the previous case. However in this regime a photon recoil is sufficient to tune an atom out of resonance with the MOT beams. Therefore the cooling is limited by the photon recoil limit, and enables the lowest temperatures of $\sim 400\,\mathrm{nK}$ to be obtained.
Note that the data shown in this thesis is mainly taken in a narrow line MOT operating in regime II or III.

2.1.2 Monte Carlo Model

A quantitative model for magneto-optical traps operating on narrow transitions was developed by R. Hanley [63] to aid in better understanding of the cloud dynamics. Here this model is briefly introduced, as a modified version is used later, for understanding the effects of applying the Rydberg dressing laser.

The simulation is typically performed for ~ 5000 atoms, which are initially placed in an ellipsoid with a particular temperature, and assigned a random velocity. The total simulation time is the carried out in steps of length δt, where for each δt the probability of each atoms to scatter a photon, for all six MOT beams and three transitions, is calculated from the steady state optical Bloch equations. From this probability it is then determined whether or not a scattering event occurs in order to find the resulting position and velocity of each atom. For each time step the atomic positions and velocities are recorded and following the simulation it is possible to obtain the spatial, thermal and temporal dynamics of the cloud as required.

Note that the model treats each Zeeman transition as an independent two-level system. This approximation is not valid for regimes where the Zeeman shift is small compared to the transition width, or large in comparison to δ. Therefore the model breaks down for the regime I MOT considered earlier, when Γ_E becomes comparable to the Zeeman splitting of the excited state, and similar to conventional MOTs the linewidth is dominant and the atoms form near the quadrupole zero. Therefore the assumption that atoms scatter independently from each Zeeman transition does not hold. However it is a good approximation outside this regime, where the MOT position, shape, temperature and cooling rate can accurately be reproduced.

Comparisons between the experiment and theory are shown in Fig. 2.2. The images in Fig. 2.2(a) consider regime II, where the MOT position and width depend on δ. In this case excellent agreement is observed between the experimental and theoretical images. The dependence of the narrowline MOT temperature on δ for two different values of s is shown in Fig. 2.2(b). When

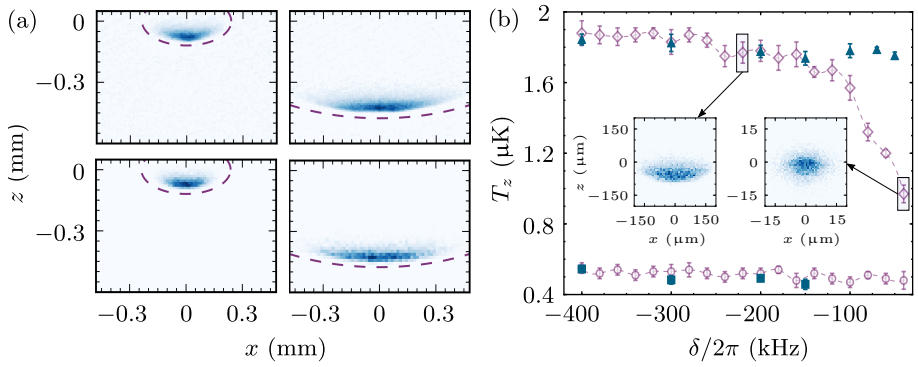

Figure 2.2: (a) Images show experimental (top row) and theoretical (bottom row) absorption image for $\delta/2\pi = -200\,\text{kHz}$ (left) and $\delta/2\pi = -800\,\text{kHz}$ (right) and $s = 9$. (b) The blue squares and purple circles represent the measured and simulated narrowline MOT temperatures for $s = 1.9$. The blue triangles and purple diamonds represent the measured and simulated temperatures for $s = 60$. Insets show theoretical absorption images at beam detunings of $-2\pi\times220\,\text{kHz}$ and $-2\pi\times40\,\text{kHz}$.

$s = 1.9$, close to regime III, the temperature is found to be independent of δ. Here the model is in excellent agreement with the measurements, for no adjustable parameters. At the higher intensity of $s = 60$ the MOT operates in regime II. As expected the cloud is observed to be hotter in this regime, while the temperature is still largely independent of δ. For large enough values of δ the model agrees with the experiment, but significant deviations are observed closer to resonance. This is due to the MOT crossing over into regime I, where the linewidth becomes dominant and the MOT forms near the quadrupole zero, as highlighted by the insets in Fig. 2.2(b). As already discussed within the regime the assumptions of the model are no longer valid.

The model therefore provides quantitative agreement between theory and experiment, in the absence of fitting parameters. More details are available in the previously published work [63], where the model is shown to replicate the spatial, thermal and temporal dynamics of the system. Extensions to this model are considered later, in order to understand the effect of the Rydberg dressing laser on the MOT dynamics. We show that good agreement

is obtained in the non-interacting regime. Therefore we then add density-dependent interactions to the simulation, to gain insight into the types of interaction effects we could expect to observe in the Rydberg dressed MOT.

2.2 Rydberg Atoms

Before introducing the concept of Rydberg dressing, we first give an overview of the properties of Rydberg atoms. Rydberg atoms are atoms where a single electron is excited to energy levels of high principal quantum number n [3]. The Rydberg series was first measured in atomic hydrogen, where the energy E_n scaled as [1]

$$E_n = -\frac{R_\mathrm{y}}{n^2}, \tag{2.3}$$

where $\mathrm{R_y}$ is the Rydberg constant. Following this Bohr's model of the atom [64] defined R_y in terms of fundamental constants:

$$R_\mathrm{y} = \frac{Z^2 e^4 m_e}{16\pi^2 \epsilon_0^2 \hbar^2}. \tag{2.4}$$

For non-hydrogenic atoms, equation 2.3 is not accurate in calculating E_n. In this case the additional charge on the nucleus is screened by the surrounding closed electron shells, however for low orbital momentum states l, the electron orbit can penetrate (or pass close to) the core leading to two effects. Firstly the valence electron is exposed to a greater nuclear charge resulting in a modified potential (from the Coulomb potential). Secondly the inner electrons can be polarised by the valence electron. Deviations of the binding energy from equation 2.3, due to these effects, are described by the quantum defect δ. Electron states which have the highest probability of being close to the core (low l) will have a larger δ, where for high enough l the electron no longer penetrates the core and the value for δ is solely due to core polarisation [65]. The resulting energy levels for a Rydberg series are well described by the equation

Property	Scaling
Orbital Radius	n^2
State energy	n^{-2}
Energy spacing	n^{-3}
Radiative lifetime	n^3
van der Waals interaction	n^{11}
Polarizability	n^7

Table 2.1: Rydberg atom scaling laws with principal quantum number [3].

$$E_n = -\frac{R_y}{(n-\delta)^2}. \tag{2.5}$$

The value δ varies slowly with n and can be written as a Ritz expansion [3]

$$\delta = \delta_0 + \frac{\delta_2}{(n-\delta_0)^2} + \frac{\delta_4}{(n-\delta_0)^4} + ... \tag{2.6}$$

From equation 2.5 the energy depends on the principal quantum number, and δ gives the difference in behavior compared to the case where only one electron interacts with the nucleus. Many other atomic properties have also been shown to scale with n, and table 2.1 shows some of these scaling laws. As already discussed in the introduction, the interactions between Rydberg atoms has resulted in a large number of applications. The long-range interactions between Rydberg atom is characterised by the van der Waals formula, $V = C_6/r^6$, where r is the internuclear distance. The C_6 coefficient scales as n^{11} resulting in strong and tuneable interactions, where its sign indicates whether the interaction is repulsive or attractive. An important consequences of the strong interactions is the well-known Rydberg excitation blockade [3, 7, 66].

Consider the two-atom case, for atoms in state $|g\rangle$ coupled to the Rydberg state $|r\rangle$. When no interactions are present the laser will excite both atoms to the Rydberg state. However, for close interatomic spacings the long-range interactions result in a energy shift in the doubly excited Rydberg state $|rr\rangle$.

If this shift is greater than the linewidth of the excitation laser, one atom in the Rydberg state will prevent the excitation of a second atom within a certain radius R_b. This minimum separation is called the blockade radius and is given by:

$$R_b = \left(\frac{|C_6|}{\gamma_b}\right)^{1/6} \tag{2.7}$$

where γ_b is the combined linewidth due to the Rabi frequency of the driving field and the linewidth of the excitation lasers. This blockade effect must be included in the calculation of the dressing potential, outlined in the next section.

2.3 Rydberg Dressing

In chapter 1 the concept of Rydberg dressing was introduced as a means for adding tuneable long-range interactions to a many-body system. Here the theory behind Rydberg dressing is introduced in more detail, along with the current state-of-the-art. Finally, the dressing scheme considered in this work is presented, including the possibility of observing interactions for such a system.

2.3.1 Rydberg Dressing Theory

As already discussed, the strong interactions between Rydberg atoms results in a suppression of further excitation within a certain volume, set by the blockade radius (R_b). In the case of Rydberg dressing this effect results in a modification of the optical AC Stark shift of the atoms. This section introduces the dressed potential for two atoms, where further treatment of the problem is found in the following references [18, 19, 67–69].

The basic idea of Rydberg dressing is to weakly dress the atomic ground state $|g\rangle$ with a small fraction of the Rydberg state $|r\rangle$. The resulting wave function is given as

$$|\widetilde{g}\rangle = \alpha\,|g\rangle + \epsilon\,|r\rangle\,. \tag{2.8}$$

For a coupling laser of Rabi frequency Ω_d and laser detuning Δ_d the dressing fraction, ϵ^2, is given as:

$$\epsilon^2 = \frac{{\Omega_\mathrm{d}}^2}{4{\Delta_\mathrm{d}}^2}. \tag{2.9}$$

The resulting dressed state has an enhanced lifetime τ_d, compared to the Rydberg state τ_r of

$$\tau_\mathrm{d} = \frac{\tau_\mathrm{r}}{\epsilon^2}, \tag{2.10}$$

extending the lifetime out to a few milliseconds. Furthermore as bare Rydberg-Rydberg interactions are large in energy scale in our experiments, dressed interactions should still be observable for small ϵ ($\sim 10^{-3}$). This technique also allows straightforward control over the interaction strength, as the dressing fraction ϵ can be tuned through the laser parameters Ω_d and Δ_d.

In considering a simple model of the dressed potential, where the interaction between the atoms $V(r)$ are van-der Waals type, the Hamiltonian in the dressed state basis $|gg\rangle$, $1/\sqrt{2}(|gr\rangle + |rg\rangle)$ and $|rr\rangle$ can be expressed as:

$$H = h\begin{pmatrix} 0 & \Omega_\mathrm{d}/\sqrt{2} & 0 \\ \Omega_\mathrm{d}/\sqrt{2} & \Delta_\mathrm{d} & \Omega_\mathrm{d}/\sqrt{2} \\ 0 & \Omega_\mathrm{d}/\sqrt{2} & 2\Delta_\mathrm{d} + C_6/r^6 \end{pmatrix} \tag{2.11}$$

Note that here the eigenstate $1/\sqrt{2}(|gr\rangle - |rg\rangle)$ is not included, as it is not coupled by Ω_d. We consider only van-der-Waals type interactions, $U(r)$, between the atoms. The dressed state energy levels are obtained by diagonalizing the matrix H and the resulting dressed interaction potential experienced by two atoms in the dressed state, separated by a distance r, is given by the following equation [18, 19, 68]:

$$V(r) = \frac{\hbar {\Omega_\mathrm{d}}^4}{8\left|\Delta_\mathrm{d}\right|^3}\left(1+\left(\frac{r}{R_c}\right)^6\right)^{-1}. \tag{2.12}$$

This potential is shown in Fig. 2.3, where to avoid Rydberg pair excitation only the case where the sign of Δ_d is opposite to that of the interactions is presented. Here R_c is the dressed blockade radius. It is defined as the distance where the effective Rabi frequency, $\Omega_\mathrm{eff} = \sqrt{\Omega_\mathrm{d} + (2\Delta_\mathrm{d})^2} \approx 2\left|\Delta_\mathrm{d}\right|$, is equal to the Rydberg-Rydberg interaction (C_6/r^6) giving the expression:

$$R_c = \left|\frac{C_6}{\hbar 2\Delta_\mathrm{d}}\right|^{1/6}. \tag{2.13}$$

The dressed potential in Fig. 2.3 can be described in terms of R_c. At large distances when $r > R_c$, the probability to find both atoms in the Rydberg state is given by $\epsilon^4 \approx {\Omega_\mathrm{d}}^4/16{\Delta_\mathrm{d}}^4$. Here the system is described as two independent atoms in the laser field where both individually experience an AC stark shift, δ_ac. In this non-interacting case, the eigenvalues from equation 2.11 determines δ_ac as:

$$\delta_\mathrm{ac} = \frac{\hbar}{2}\left(\Delta_\mathrm{d} \pm \sqrt{\Delta_\mathrm{d}^2 + \Omega_\mathrm{d}^2}\right). \tag{2.14}$$

However at $r = R_c$ the Rydberg-Rydberg interactions tune the doubly excited state out of resonance. As the distance between the atoms reduces further, the probability to dress both atoms decreases and the potential saturates. The difference in energy from the non-interacting to the strongly interacting regime is:

$$V_0 = \frac{\hbar {\Omega_\mathrm{d}}^4}{8{\Delta_\mathrm{d}}^3}. \tag{2.15}$$

Therefore the parameters which determine the magnitude of the interaction are Ω_d and Δ_d. In Fig. 2.3 the Rydberg fraction, ϵ^2, remains constant for both calculations of the dressed potential. However as the dressed potential from equation 2.15 scales stronger with Ω_d than Δ_d, by increasing the Rabi frequency the resulting magnitude of the dressed potential is larger. This

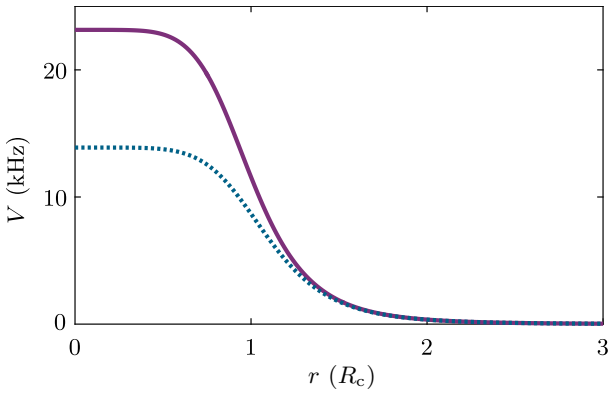

Figure 2.3: The interaction potential of a pair of Rydberg dressed atoms as a function of the interatomic separation in units R_c, for the 5s36d $^3D_2$ state. Two different combinations of Rabi-frequency and coupling laser detuning are shown for $\Omega_d/2\pi$ =5 MHz, $\Delta_d/2\pi$ =15 MHz (solid purple line) and $\Omega_d/2\pi$ =3 MHz, $\Delta_d/2\pi$ =9 MHz (dashed blue line).

means the interaction strength can be scaled while the Rydberg fraction ϵ^2 remains constant. However the length scale of the interaction potential depends only on R_c (equation 2.13). Typically in our experiment this can range from $\sim 1 \rightarrow 5\,\mu$m.

From this simple two atom description of Rydberg dressing, we now consider the case of N Rydberg dressed atoms. Here we begin by following the treatment outlined in [69]. At low densities, where $r > R_c$, the atoms are independent, and the energy of the system is given as the number of atoms, N, times the light shift a single atom from equation 2.14. However in the high density limit ($r < R_c$), the Rydberg blockade results in all N atoms sharing one Rydberg excitation, forming a collective state. This state is coupled by the dressing laser to the ground state with a collectively enhanced Rabi frequency $\sqrt{N}\Omega_d$. In this regime the atoms experience a collective energy shift $V = N(N-1)V_0/2$. The N atom dressed potential is then described by [18, 68]:

$$V(r) = \frac{N(N-1)V_0}{2}\left(1 + \left(\frac{r}{R_c}\right)^6\right)^{-1} \tag{2.16}$$

where equation 2.12 is recovered for the case when $N = 2$.

However, the correct description of Rydberg dressing in a dense gas is still an active area of study. Much remains to be understood on the complex dynamics in dense Rydberg gases, and a variety of experiments as outlined in the next section have attempted to answer some of these open questions.

2.3.2 State-of-the-Art

Rydberg dressed interactions have been demonstrated for two atoms [26] and in an optical lattice [27]. So far the challenge of dressing a randomly distributed ensemble remains, where the first experiments have measured uncontrollable loss mechanisms [29–32, 57, 70]. An overview of these experiments is outlined in this section, giving the reader some knowledge of the current state of the art before moving on to describe our system.

The first successful dressing experiment was carried out for a system of two atoms [26]. In this experiment two cesium atoms were held a few µm apart using optical tweezers. The atoms were then moved towards one another, where at some target distance a dressing laser at 319 nm was pulsed on coupling atoms directly from the ground to the Rydberg state. During the dressing stage tweezers were turned off so as not to cause any light shifts from the dipole trap laser. After pulsing on the dressing laser, the optical tweezers were then used to catch the atoms and translate them back to their original position for state detection. Using this method the interaction strength was measured as a function of the interatomic distance, showing quantitative agreement with the two body potential in Fig. 2.3. This result was an important first step for dressing, but avoided many complications as seen in other experiments by only using a system of two atoms.

The other successful dressing experiment was performed in an optical lattice [27]. In this experiment ∼200 rubidium atoms were loaded into a two dimensional lattice with near unity filling, where a 297 nm laser was used to couple the ground state atoms directly to the Rydberg state. A Ramsey spin-echo sequence was then used to probe the resulting long range interactions, combined with single atom sensitive detection. The measurements

confirmed the presence of Rydberg dressed interactions, where the tunability and anisotropy of the interactions was also demonstrated. However the coherence was found to be limited by a fast avalanche-like loss process. This experiment avoids complications by working with limited dimensionality, where our interest lies in the realization of long-range interactions in a randomly distributed ensemble.

Rydberg dressing experiments in the many-body regime have been pursued in both 3D optical lattices and dipole traps [29–32, 57, 70]. Here coherent off-resonant dressing has proved to be more of a challenge due to observed loss mechanisms. The work in [32] focused on understanding the dephasing mechanisms in more detail and finding possible solutions to overcome such trap loss. The reported results suggest that the loss is largely attributed to blackbody induced transitions to nearby Rydberg states, which have large resonant dipole-diplole interactions with the state of interest. This effect triggers an avalanche-like process where the production of the first atoms in such contaminant states facilitates the creation of more Rydberg atoms. To overcome this problem which prevents the observation of dressed interactions we now present an alternative system for studying such effects.

2.3.3 A Rydberg dressed MOT

The experiments outlined in the rest of this thesis involve adding Rydberg character to a narrow-line magneto-optical trap. The main differences between broadline and narrow-line MOTs was introduced earlier in this, and here we show these differences result in an ideal platform for performing Rydberg dressing experiments. The main properties of narrow-line MOTs which are important for this discussion are as follows:

- Temperatures as low 400 nK are possible as the temperature is dominated by the single photon recoil temperature.
- The reduced scattering rate leads to higher MOT densities of $\sim 1 \times 10^{12}\,\mathrm{cm}^{-3}$.

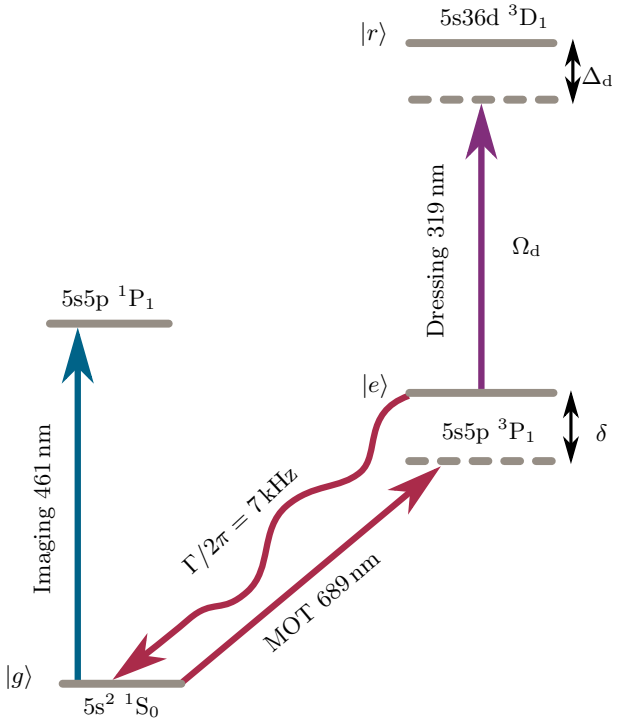

Figure 2.4: Schematic diagram for Rydberg dressing a MOT. The MOT operates on the 689 nm transition is dressed by off-resonantly coupling the state $|e\rangle$ to a Rydberg state $|r\rangle$. The strong 461 nm transition is used for absorption imaging

- The MOT beam detuning δ determines the cloud shape and positions with a sensitivity of $\sim$10 kHz

Dressing Scheme

The dressing scheme used in our experiments is shown in Fig. 2.4. In this scheme the Rydberg dressing is applied to an excited state $|e\rangle$ undergoing spontaneous emission. Experiments begin with the formation of a MOT operating on the 689 nm intercombination line. To form a Rydberg-dressed MOT the excited state $|e\rangle = 5s5p\ ^3P_1$ is coupled to a Rydberg state $|r\rangle$. The coupling laser, described later in chapter 4, has a detuning of Δ_d from the Rydberg state, and a Rabi frequency Ω_d. Following the experiments the cloud was imaged on the strong 461 nm transition.

For reasonable choices of Ω_d and Δ_d the peak magnitude of the dressed interactions, V_0, typically range from $0 \rightarrow 100$ kHz. For most cooling tran-

sitions this is far smaller than the linewidth, however the linewidth of the $5s^2\ {}^1S_0 \rightarrow 5s5p\ {}^3P_1$ transition is only $2\pi\times7.4\,\mathrm{kHz}$. This means V_0 is comparable to both the linewidth ($\hbar\Gamma$) and kinetic energy (k_BT). Additionally, we find that R_c can exceed the mean atom spacing in the excited state, $\langle r_e \rangle$.

Comparing MOT and dressing parameters

A comparison of the dressed potential to the properties of the narrow-line MOT are important for understanding whether interactions should effect the MOT dynamics. Here to test the viability of dressing in a MOT we consider the $5s36d\ {}^3D_2$ state, where a large portion of the experimental results in chapter 6 were obtained. The reason for using this state is due to the reduced atom loss seen in our experiments, where more details are gives in chapter 6.

For considering the interaction potential in the MOT the mean fraction of atoms in the state $|e\rangle$, η, is an important parameter. For our experiments we calculate η to be in the range of $0.05 \rightarrow 0.07$, which is used to calculate the number of atoms per dressed blockade radius N_c:

$$N_c = \frac{\eta\rho 4\pi {R_c}^3}{3} \tag{2.17}$$

where ρ is the MOT density. The dressed potential $V_c(r)$ is then described by equation 2.16, where $N = N_c$. To reach the strongly interacting regime in our experiment, we therefore need the condition $V_c/N_c \geq \hbar\Gamma, k_bT$, where $N_c \geq 1$.

To calculate achievable dressed potentials we now consider some typical experimental values. For the $5s36d\ {}^3D_2$ state we have measured the value $\Omega_d/2\pi \sim 5\,\mathrm{MHz}$ (see chapter 5). Note that the Rabi frequency of the coupling laser scales with principal quantum number n as $n^{-3/2}$. The dressed potentials shown in Fig. 2.5 are calculated for this state and Ω_d, where $N_c = 2.5$ (equation 2.17), and the detuning is $\Delta_d/2\pi = 15\,\mathrm{MHz}$. The high achievable densities of the narrow-line MOT lead to an atom distribution shown by the purple shaded area in Fig. 2.5. Here the interparticle spacing

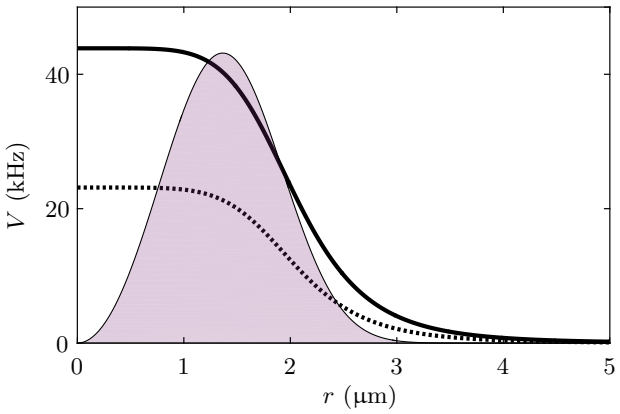

Figure 2.5: The dressed potential for two atoms, $V(r)$, (equation 2.12, dashed black line) and for N_c atoms, $V_c(r)$, (equation 2.16, solid black line) for the 5s36d $^3D_2$ state, where $\Omega_d/2\pi$ =5 MHz and $\Delta_d/2\pi$ =15 MHz. The atom distribution (purple shaded area) is also shown for comparison, where the method for calculating the distribution is described in the main text.

is calculated using the Wigner-Seitz radius, $a = (3/4\pi\rho)^{1/3}$, where ρ is the density [71]. The atom distribution $P(r)$ can then be obtained from the following equation [72]:

$$P(r) = \frac{3r^2}{a^3} e^{-\left(\frac{r}{a}\right)^3} \tag{2.18}$$

For our achievable densities of $\sim 5 \times 10^{11}$ cm^{-3} considered in Fig. 2.5 the calculated distribution shows that atoms should be able to explore the dressed potential.

From choice of Rydberg state it is possible to change the length scale of the dressed potential. For high n states, or states close to a Förster resonance a dressed blockade radius of ~ 4 μm is possible [73]. We expect a Förster resonance to occur in the 5snd $^3D_2$ series, and as the C_6 coefficients rise near a Förster resonance we should see stronger interactions for the 5s36d $^3D_2$ and 5s37d $^3D_2$ states [73]. Note that at the Förster resonance we would observe resonant dipole-dipole interactions, rather than van der Waals interactions. Furthermore, with our currently ongoing upgrades to the UV system outlined in chapter 4, it will be possible to reach higher Rabi frequencies, allowing an increase in the magnitude of the dressed potential. However the take away message from Fig. 2.5 is that for reasonable experimental parameters

we expect to be able to probe the dressed interactions. Exact parameters for the different states we used are considered in chapter 6.

Another important question is what are the expected trap lifetimes, and whether they are sufficiently long for the interactions to modify the dynamics. For this to be the case the lifetime must be greater than the equilibration time of the MOT, which is typically a few ms. In our experiment $\sim 10\%$ of the atoms are in the dressed state, and typical Rydberg lifetimes are on the order of 50 µs. By modifying equation 2.10 to include η, i.e. $\tau_{\mathrm{d}} = \tau_{\mathrm{r}}/\epsilon^2\eta$, the expected trap lifetime would be 18 ms. This value is promising as it is long compared to the MOT equilibration time, assuming that loss mechanisms, such as those observed in other experiments, do not lead to a reduced lifetime. The measured lifetimes are discussed in detail in chapter 6, along with any observed loss mechanisms.

Interaction Observables

The intended method for observing Rydberg-dressed interactions in the MOT is through a modification of the MOT dynamics. Here we first attempt to model the effect of the interactions. Full treatment of the system is rather challenging, and would require the inclusion of correlations between the atoms. Therefore we also discuss spatial and dynamical effects that may not be captured by our model. In the model, the main effect we expect to arise comes from the detuning sensitivity of narrow-line MOTs. The trap forms where the detuning δ matches the Zeeman shift from the quadrupole magnetic field and the gravitational sag. As such δ determines the cloud shape and position with sensitivities on the order of 10 kHz. The expected interaction strengths from Fig. 2.5 are on the order of tens of kHz, which would shift the excited state of the MOT transition, hence altering the MOT beam detuning. This in turn leads to a shift in the MOT position.

As discussed previously in this chapter, the dynamics of the MOT can be modeled accurately using a Monte Carlo simulation [63]. By adapting the model to include the effect of the dressing beam, the dressed MOT dynam-

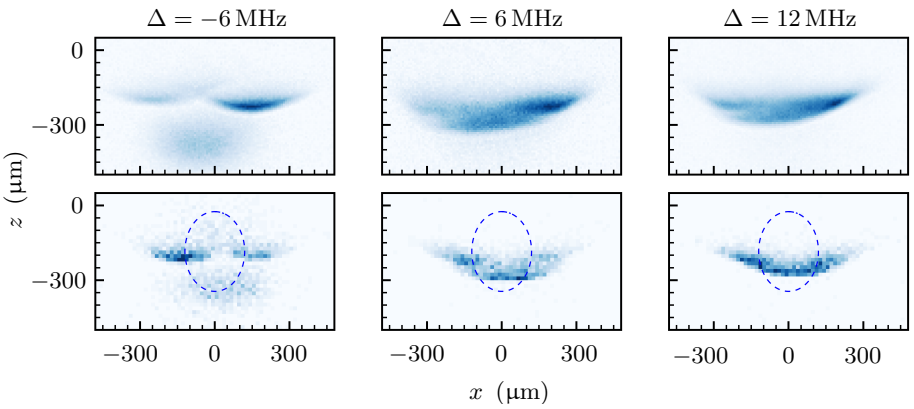

Figure 2.6: The top (experimental) and bottom (theoretical) rows show images of dressed MOT at the 5s36d $^3D_1$ state for different Δ_d. Here $\Omega_d/2\pi = 2.1\,\text{MHz}$, $\delta/2\pi = -400\,\text{kHz}$. The coupling beam position is shown in the experimental images.

ics in the absence of interactions can be predicted. The upgraded model was the work of R. Hanley, where later work will provide more details. The adaptation to the model required solving the three-level optical Bloch equations analytically to include the AC Stark shift of the MOT transition. The probability that an atom is lost from the MOT due to the direct excitation of a Rydberg atom is given by

$$P = \Gamma_r \rho_{rr} \delta t \tag{2.19}$$

where Γ_r is the Rydberg state decay rate, ρ_{rr} is the Rydberg state population and δt is the simulation timestep.

Experimental results in the non-interacting regime are compared to this model in Fig. 2.6. The data was taken at the 5s36d $^3D_1$ Rydberg state, for which the interactions are relatively weak [53].

As the coupling beam was much smaller than the MOT when taking the experimental data, this accounts for the changes in shape between the wings and centre of the MOT. Here the only initial free parameter is the position of the coupling beam on the MOT. However once this parameter is obtained for one image, it remains fixed for further simulations at different detunings. The position of the coupling beam is shown by the dashed line in Fig. 2.6.

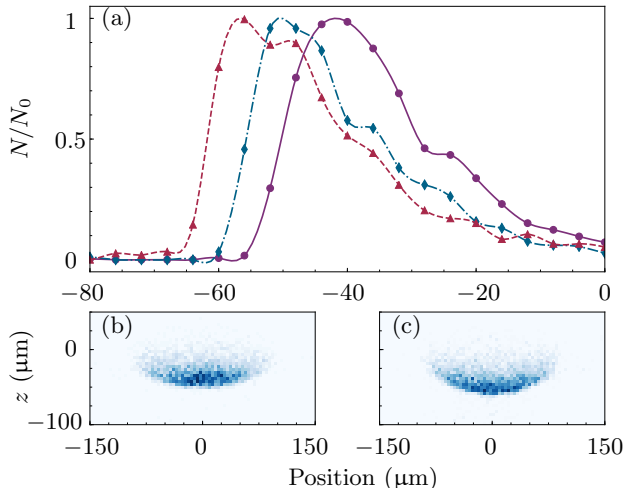

Figure 2.7: (a) Vertical slices through the center ($z = 0$) of the simulated density distribution for parameters: non-interacting ($V_0 = 0$ (purple circles)), $\{\Omega/2\pi = 16\,\text{MHz}, \Delta/2\pi = -96\,\text{MHz}, V_0 = 9.26\,\text{kHz}$ (blue diamonds), $\{\Omega/2\pi = 16\,\text{MHz}, \Delta/2\pi = -68\,\text{MHz}, V_0 = 26.05\,\text{kHz}$ (red triangles). The lines are a guide to the eye. Images show the full 2D density distribution for the (b) non-interacting ($\bar{V}_0 = 0$) (c) interacting ($V_0 = 26.05\,\text{kHz}$) clouds.

There is excellent agreement between the theoretical and experimental images for the spatial distribution of atoms in the MOT. This provides confidence that we have a good understanding of the non-interacting regime, allowing us to include density dependent interactions into the model. This extension to the model for predicting possible signatures of the dressed interaction is now considered.

In this case the Rydberg-dressed potential is approximated as:

$$V\left(N_c\left(\boldsymbol{r'}\right), \boldsymbol{r}\right) = \frac{N_c\left(\boldsymbol{r'}\right) - 1}{2} V_0 \qquad \text{for } \left|\boldsymbol{r} - \boldsymbol{r'}\right| < R_c\,, \tag{2.20}$$

$$V\left(N_c\left(\boldsymbol{r'}\right), \boldsymbol{r}\right) = 0 \qquad \text{for } \left|\boldsymbol{r} - \boldsymbol{r'}\right| > R_c\,, \tag{2.21}$$

where $N_c\left(\boldsymbol{r'}\right) = \eta\pi R_c^2 \rho_{2D}\left(\boldsymbol{r'}\right)$, and $\rho_{2D}\left(\boldsymbol{r'}\right)$ is the local atomic density. This leads to an additional energy shift $V\left(N\left(\boldsymbol{r'}\right)\right)/\hbar$ of $|\tilde{e}\rangle$ that depends on $\rho_{2D}\left(\boldsymbol{r'}\right)$. The additional energy shift is included in the model, leading to a change in the scattering dynamics.

Results from the simulation are shown in Fig. 2.7 for the 5s36d $^3D_2$ state. Here we assume the dressing beam is 300 × 100 μm with uniform intensity

and a power of 1 W, so that the AC stark shift is uniform across the cloud. The results are simulated for our expected densities, dressing state fractions, η, and Rydberg dressed fractions, determined from the experimental results of chapter 6. A larger Rydberg fraction is also considered by decreasing the detuning. From Fig. 2.7 it is clear that the interaction causes a significant density-dependent shift in the vertical position of the cloud. In addition to the shift there is a "bending" of the cloud, as the effect of interactions is larger in the center than in the wings due to the density-dependence of the mean-field interaction. The effects are large enough to be observed and measured in future experiments as the position shift is on the order of the cloud size. Note that a full treatment would require including correlations between the atoms, but this a challenge theoretically. This is due to the fact that for the Rydberg-dressed MOT the interaction strength, dissipation and kinetic energy are comparable in scale, limiting the usefulness of commonly used approximations [74–79].

As we expect that our mean-field description will not provide a complete description, we now consider the possibility of beyond mean-field effects due to correlations. A more complete theory would be required for quantifying the likelihood of observing such effects. However in the future we hope to investigate experimentally whether or not such effects emerge in this system.

For instance we could expect that the dressed interactions lead to shape changes in the atom distribution. In the case of repulsive interactions, a reduced scattering rate near Rydberg-dressed atoms may result in the formation of dense clusters. Another interesting mechanism could arise from the presence of cooling along with mechanical effects from the interactions. For atoms moving along the dressed potential a system is formed where it is possible to add potential energy while removing kinetic energy, following the decay of an atom to the ground state. This is depicted in Fig. 2.8, where in (a) it is shown that the added Rydberg character in the excited state results in a value δ that is density dependent. Therefore an atom excited to the dressed state can move along the dressing potential due to interactions

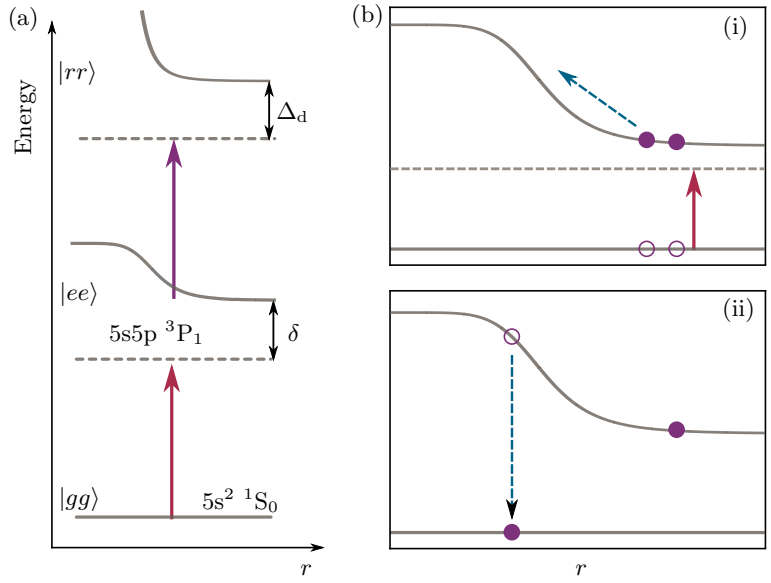

Figure 2.8: (a) Here we show the dressing scheme, highlighting that the added Rydberg character in the excited state results in a value δ that is density dependent. (b) Illustrates the fact that cooling mechanism may arise from the dressed interactions. (i) From the density dependance of δ, it is more likely to excite atoms near the bottom of the potential. (ii) An atom moves along the potential before decaying back to the ground state, resulting in cooling.

between the dressed pairs, before decaying to the ground state as illustrated in Fig. 2.8(b). There is a higher probability of the MOT light exciting pairs of atoms that will experience cooling rather than heating. This effect is similar to a Sisyphus-like cooling mechanism [80, 81], where the modification of scattering probability is induced by the dressed potential.

All these effects are easily measurable in our experiment through imaging on the 461 nm transition (Fig. 2.5). The position and shape of the MOT can be determined directly from the absorption images, while measuring a ballistic expansion of the cloud width determines the temperature.

Chapter 3

Experimental Methods

All the experiments outlined in this thesis required first creating a MOT on the narrow $5s^2\ {}^1S_0 \rightarrow 5s5p\ {}^3P_1$ transition in strontium. This chapter provides detail on the apparatus used in the experiment, along with the methods for preparing the sample of cold atoms. Finally the measurement techniques for acquiring the data shown in this thesis are discussed.

3.1 Experimental Apparatus

More information on the main apparatus and laser systems are available in several prior theses from this project [82–85]. Here I provide a general overview of the main apparatus, where any changes and improvements made during the course of this work are highlighted.

3.1.1 Vacuum System

The main vacuum chamber is presented in Fig 3.1, which was developed during the thesis of J. Millen [82]. An atomic vapor of strontium is produced by heating the oven to $\sim 400\,^{\circ}\mathrm{C}$. The atomic beam is first slowed by passing through a 'spin-flip' Zeeman slower, which is based upon work in [86]. The slowing beam is counter-propagating to the atomic beam and operates on the $5s^2\ {}^1S_0 \rightarrow 5s5p\ {}^1P_1$ (461 nm) transition. Typical powers of $\sim$45 mW are

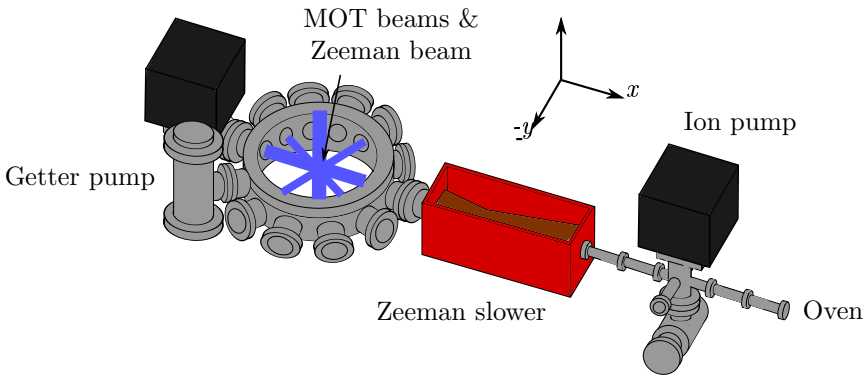

Figure 3.1: Vacuum chamber used in the experiments. Strontium atoms from an oven are heated to $\approx 400\,^{\circ}\mathrm{C}$ producing an atomic beam. The atoms are decelerated as they pass through a Zeeman slower, then cooled and trapped using the MOT beams and a quadrupole magnetic field. Image taken from [84].

used, where the beam is red detuned by $\sim 16\Gamma$.

The slowed atomic beam then enters the main science chamber for further cooling and trapping. Both the oven and science chamber have a 20 l/s ion pump, where the chamber is further pumped by a 200 l/s non-evaporable getter. The main chamber also contains a pair of in-vacuum anti-Helmholtz coils which produces a quadrupole magnetic field (up to $25\,\mathrm{Gcm}^{-1}$). An additional coil, referred to as the 'quantisation coil', sits outside the chamber below the bottom viewport, allowing uniform magnetic fields to be applied to the chamber. To compensate stray magnetic fields in our experiment three pairs of external coils, with orthogonal axes, are installed around the chamber. These coils are referred to as the 'compensation coils' throughout this work. The control over the electric field in the chamber is achieved through a set of four pairs of electrodes in a split-ring configuration.

Both a top-down view and cross-section through the chamber are shown in Fig. 3.2. The top-down view in Fig. 3.2(a) highlights the paths for each of the laser beams used in our experiments. This is with the exception of the vertically propagating MOT beam and the 689 nm probe beam, where both enter the chamber through the top viewport. Note that the blue MOT beams follow the same path as shown for the red MOT. The 408 nm laser

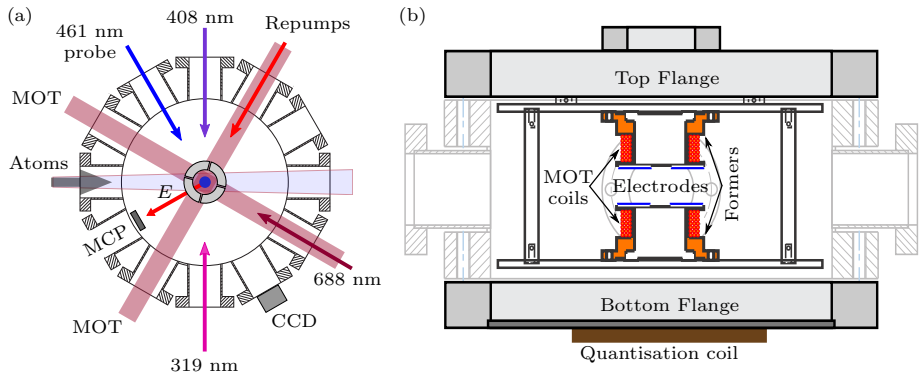

Figure 3.2: (a) Top-down view of the vacuum chamber, along the axis of vertical MOT beams. The different beam paths for the lasers relevant to this work are shown. The split-ring electrode geometry is shown in the centre. The arrow labeled E shows the direction of the electric field used to direct ions to the MCP. (b) A cross-section through the main chamber taken from [82]. The internal MOT coil former assembly is mounted to the top flange. Electrical connections to the MOT coils and electrodes are made through electrical feed-throughs on the top flange (not shown).

addresses the Rydberg autoionisation transition, and the 688 nm laser is used to shelve atoms in the 5s5p $^3P_2$ state. Both these techniques are discussed later in the chapter.

Since finishing the experiments outlined in this thesis there has been a major upgrade to the vacuum system. The two main changes compared to the design in Fig. 3.2(b), are a new electrode configuration along with in-vacuum lenses. The electrode configuration is now a hexagonal split ring, rather than a set of four pairs. The advantage of this change is the ability to produce uniform longitudinal electric fields along any laser beam direction. In particular this will be useful for future absolute frequency measurements of Rydberg states, as it will make it easier to precisely null any stray DC electric fields in the chamber. The two high numerical aperture lenses placed inside the vacuum chamber were added for future experimental directions of the project outlined in chapter 7. These lenses will allow a laser beam to be focused to a waist of $\sim 1\,\mu$m at the centre of the vacuum chamber. As this design was mainly the work of current PhD student R. Hanley, a later

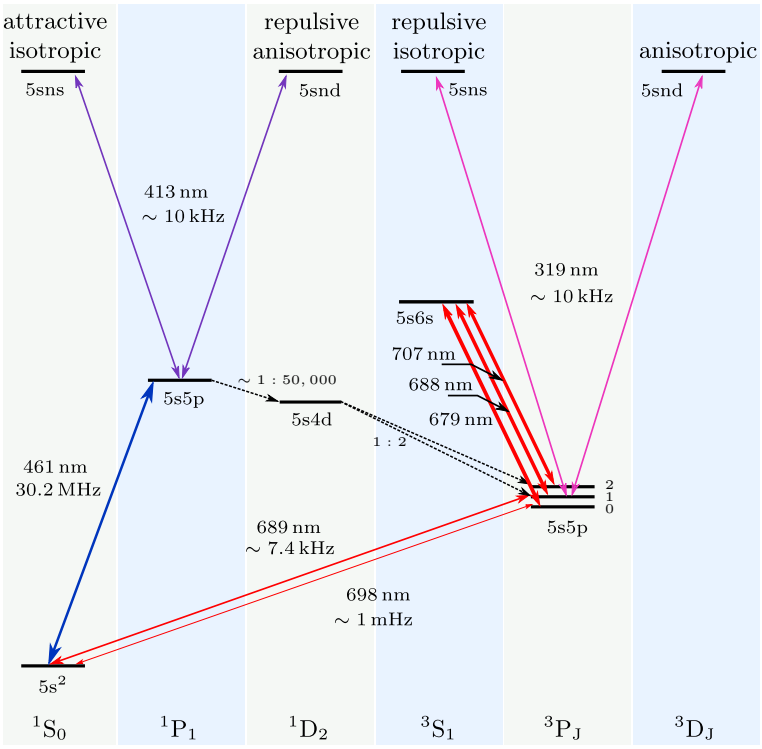

Figure 3.3: Energy level diagram showing the cooling, repump and Rydberg excitation transitions in the ^{88}Sr isotope.

work will provide more detail on the new system.

3.1.2 Laser Systems

The wavelengths of the different lasers required for our experiment are presented in the energy level diagram in Fig. 3.3. In order to generate these wavelengths a mixture of home built and commercial diode laser systems are used. This section outlines how each laser wavelength is generated and stabilised for our experiments. This is with the exception of the Rydberg excitation laser at 319 nm which is discussed in depth in chapter 4.

461 nm Laser System

The primary cooling transition in strontium is the dipole allowed $5s^2\ {}^1S_0 \rightarrow 5s5p\ {}^1P_1$ transition. The laser source is a commercial Toptica DL100-TA-SHG system which produces up to 300 mW of 461 nm light, where the laser

frequency is stabilised using modulation transfer spectroscopy [87]. The output from the laser is split into several beam paths. The Zeeman light ($\sim$ 45 mW) is picked off first, before sending the remaining light to a single-mode polarisation maintaining fibre. The beam at the fibre output is then split between the laser lock ($\sim$2 mW), MOT beams ($\sim$10 mW) and the absorption imaging beam ($\sim$2 mW). The frequency and on/off control of each beam are set using acoustic-optic modulators (AOMs), where mechanical shutters are used in both the Zeeman and MOT beams to eliminate heating due to light leakage.

Repump Lasers

Atoms in the 5s5p $^1P_1$ state can decay to the lower lying 5s4d $^1D_2$ state as depicted in Fig. 3.3. From here the lost atoms decay to both the 5s5p $^3P_1$ and $^3P_2$ states, the latter of which is metastable. This means atoms can escape the cooling cycle during the blue MOT loading time, and although the decay rate is slow (50,000:1 branching ratio) [88], we observe a reduction in the MOT atom number, density and trap lifetime.

To bring atoms back into the cooling cycle we use two repump lasers at wavelengths of 707 nm and 679 nm. The 707 nm laser addresses the 5s5p $^3P_2 \rightarrow$ 5s6s $^3S_1$ state, from which they decay back into the 5s5p $^3P_{0,1,2}$ states. The 679 nm laser then addresses the 5s5p $^3P_0 \rightarrow$ 5s6s $^3S_1$ transition. The resulting atoms populating the 5s5p $^3P_1$ state can then decay quickly back to the ground state, returning to the cooling cycle.

The two repump lasers are homebuilt external cavity diode lasers (ECDLs) with piezos for wavelength control. The frequency is stablilised to a HighFinesse WS7 wavemeter, and typically 2 mW of each beam enters the chamber during the blue MOT load. While different repumping schemes are possible which only require a single laser [89, 90], these techniques are more costly and complex.

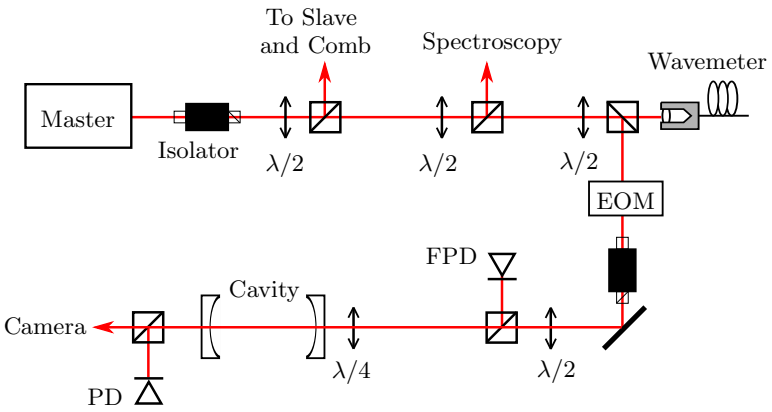

Figure 3.4: Optical set–up of the 689 nm laser system as described in the main text. The master light is used for injection locking the slave diode, and a pick-off is sent to the frequency comb. The master light is locked to a high finesse cavity, where the cavity length is stabilised through saturated fluorescence spectroscopy.

689 nm System

The 689 nm system was developed during the thesis of D. Boddy [84], and further details of this system are available in [85, 91]. The 689 nm light is used for a second stage of cooling following the blue MOT, performed on the $5s^2\ {}^1S_0 \rightarrow 5s5p\ {}^3P_1$ transition. The transition linewidth is only $2\pi\times7.4$ kHz and therefore we require a narrow-linewidth laser, on the same order as that of the transition.

The 689 nm system is a master-slave set-up using home built lasers, and the optical set-up is shown in Fig. 3.4. The master system is an ECDL, where the short-term laser linewidth is reduced using the phase locking technique developed in [92, 93]. This requires a high-finesse optical cavity to provide a narrow reference signal, and details of our cavity are available in the thesis of D. Boddy [84]. The laser is stabilised to the cavity using a commercial fast feedback circuit (Vescent D2-125 Laser Servo). This technique is discussed in more detail in chapter 4 as the Rydberg excitation laser is locked using similar methods. Long-term frequency drifts are suppressed by using two piezo-electric transducers to stabilise the cavity length. This involves using saturated fluorescence spectroscopy to lock to a sub-Doppler resonance feature in a thermal beam of strontium.

Light from the stabilised master diode is then used to injection lock a slave laser, for attaining the required optical power. The slave system produces up to 40 mW, which is delivered to the experiment via single-mode polarisation maintaining fibre. An AOM is used for modulating the beams (discussed later in section 3.2.2), and for switching on/off control. A small pick-off is taken from the slave light, which is used for performing Rydberg spectroscopy.

One of the difficulties encountered with the system during this work was a high cavity drift rate due to piezo relaxation. The effect was more apparent at lower voltages, leading to increased frequency noise on the 689 nm laser. The laser was observed to drift, while locked to the cavity, on the order of 100 MHz per hour, with higher drift rates of $\sim$ 1 GHz per hour at lower piezo voltages. This affected measurements in the narrowline MOT, as the frequency fluctuations reduce the MOT lifetime, while leading to increased shot-to-shot noise in the cloud position. The piezo was driven by a Thorlabs 150 V driver, and to deal with the issue a 50 V battery pack was connected in series with the driver. Here the maximum voltage of 200 V was still within the piezo specification, and the added voltage greatly reduced the drift rate to <100 MHz per hour, provided the piezo voltage was operating at >100 V. Since finishing taking the data presented in this thesis, the frequency stability has been improved by switching the cavity to a commercial ultra-low-expansion (ULE) cavity. As a result there is currently no need to use the saturated fluorescence spectroscopy for locking, and in the future any long-term drift can be minimised by continuously measuring a beat note between the laser and frequency comb, and compensating the laser frequency accordingly. Another recent improvement to this system was to rebuild the master ECDL laser system following the Steck laser design [94], where the standard diode was replaced with an AR coated diode. Since implementing these changes the observed frequency stability of the laser is much better than for the old system (see chapter 4). Additionally the laser can remain locked to the cavity for a long time (> 1 day), which was never the case before the upgrades ($\sim$ 1 hour). The long and short-term frequency stability of both

the old and new systems are discussed in chapter 4, when considering the stability of the Rydberg excitation laser.

408 nm Laser

A laser at 408 nm is used to address the the Rydberg autoionising transition. This laser is a homebuilt ECDL, which autoionises Rydberg atoms through a process known as 'isolated core excitation' [95]. The frequency is stabilised to a HighFinesse WS7 wavemeter which is usually set to give the maximum autoionising signal as described in [83]. The detection of Rydberg atoms using this signal is described in further detail later. The light is sent to the main chamber via a single-mode polarisation maintaining fibre.

688 nm Laser

A 688 nm laser was added to the experiment partway through this work. The laser operates on the 5s5p $^3P_1 \rightarrow$ 5s6s $^3S_1$ transition. The purpose of this laser was to apply a short of pulse of both 688 nm light just before imaging, to shelve the atoms in a longer lived state (see Fig. 3.3). The reason for this additional laser was to reduce the optical depth when imaging, aiding in determining the atom number, density and width of dense clouds more accurately (see section 3.3). The laser system is a homebuilt ECDL following the Steck design [94], and 4 mW of power was produced directly before the chamber.

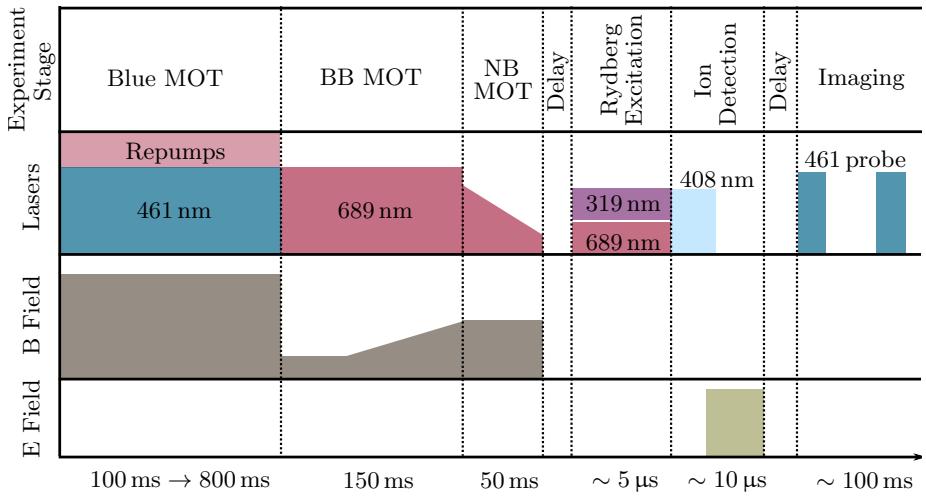

Figure 3.5: A typical experimental sequence for a standard Rydberg excitation experiment. There are some deviations throughout this thesis from this sequence which will be mentioned as required. A change in the height of a timing block corresponds to a change in the relative magnitude of the laser intensity or field gradient in question.

3.2 Preparing the Atomic Sample

All the strontium Rydberg experiments in this thesis require first preparing a sample of cold atoms. The process involves two main stages. First the Zeeman slowed atoms are captured and cooled in a MOT operating on the broad 461 nm transition. Following this the atoms then undergo a second stage of cooling in a MOT operating on the narrow intercombination line. The second stage of cooling involves both broadband (BB) cooling (where the light is frequency-broadened), before transferring the atoms into a narrowband (NB) MOT. This is discussed in further detail later in this chapter. Previous studies of these cooling techniques in strontium are available in a number of publications [62, 84, 96]. In this section it is shown that the process allows control over final density, temperature and size of the cold atom cloud. A typical experimental sequence required for laser cooling, with subsequent Rydberg excitation and detection is presented in Fig. 3.5.

Table 3.1 summarises the densities, atom numbers, temperatures and cloud size we can expect following each cooling stage in the experimental sequence.

Cooling Stage	Atom Number	Density (cm^{-3})	w_z (μm)	Temperature (μK)
Blue MOT	2×10^7	2×10^9	1×10^3	5×10^3
Broadband MOT	1×10^7	1×10^{11}	150	20
Narrowband MOT	2×10^6	1×10^{12}	20	0.8

Table 3.1: A comparison of atom number, density, width ($1/e^2$ radius in z direction) and temperature following each cooling stage outlined in this chapter.

There is some level of control over the narrow-line MOT density and size, and the parameters used are identified throughout the work as appropriate.

3.2.1 First Stage MOT

Both the construction and characterisation of the first stage MOT was carried out in prior works by J. Millen [82] and G. Lochead [83]. The MOT operates on the $5s^2\ {}^1S_0 \rightarrow 5s5p\ {}^1P_1$ transition. Here the 461 nm MOT light typically operates with a total power of 12 mW, $1/e^2$ waist of 5 mm and detunings of $\sim 1.2\Gamma$. The MOT light is split into three beams which intersect orthogonally, and are then retro–reflected to produce a six beam MOT which forms in the centre of the chamber. An axial gradient of 25 Gcm^{-1} is used during loading of the blue MOT.

Usually a loading time < 100 ms is standard, resulting in atoms numbers of 2×10^7, temperatures of 5 mK and densities of around $2 \times 10^9\ cm^{-3}$. However the blue MOT loading deteriorated over time leading to lower atom numbers. This was attributed to a significant build-up of strontium on the Zeeman viewport causing attenuation in the Zeeman beam. Over time a number of improvements allowed us to retain the same atom numbers and densities. This included adding the repump lasers during the MOT load, increasing the power in the Zeeman beam to 60 mW and using longer MOT load times of ~ 800 ms.

Following the experiments outlined in this thesis the Zeeman viewport has

been changed. It is now possible to load the blue MOT in 100 ms. Also, in order to reduce future problems with the build-up of strontium on the viewport the oven flux was reduced.

3.2.2 Second Stage MOT

The 5 mK temperature following the blue MOT is sufficient for atoms to be captured in the second stage MOT. This second stage of cooling operates on the $5s^2\ {}^1\mathrm{S}_0 \rightarrow 5\mathrm{s}5\mathrm{p}\ {}^3\mathrm{P}_1$ intercombination line, and operates in two main steps.

Initially to increase the fraction of atoms which are transferred to the red MOT, the light is frequency-broadened to match the velocity distribution of the atoms. This is achieved by modulating the RF drive field to the slave AOM with a sinusoidal waveform to produce a comb of discrete frequencies. Here a modulation deviation of 2 MHz with a modulation frequency 50 kHz is applied. During the start of this phase, the magnetic field is reduced to $3\,\mathrm{Gcm}^{-1}$, increasing the size of the resonance ellipse, to enable high transfer efficiency from the blue MOT. After 50 ms of cooling the magnetic field is then linearly ramped over 100 ms to $8\,\mathrm{Gcm}^{-1}$ to increase the confinement. In this broadband stage of cooling a total MOT beam power of 15 mW with detuning 350Γ is applied. The light used for MOT beams is spatially overlapped with the blue MOT trapping light on a dichroic mirror after the fibre output. This phase is referred to throughout the rest of the text as the broadband MOT. For some experiments in this work the broadband MOT is used when lower temperatures and higher densites are not required. Typical values following this stage are atoms numbers of 10^7, densities $1 \times 10^{11}\,\mathrm{cm}^{-3}$ with temperatures of 20 μK.

For the final stage of cooling the atoms are transferred into the narrowband MOT by switching off the modulation to the AOM. A linear sweep of the single frequency MOT increases the transfer efficiency. The starting frequency is chosen to match the detuning of the broadband sideband closest to resonance ($\delta/2\pi$ =300 kHz), and the final frequency is typically in the

range of 100 to 140 kHz. Additionally this stage sometimes includes a power ramp when requiring low final powers, which results in larger atom numbers following the narrowband stage. Compared to the broadband stage, the narrow-line MOT results in lower temperatures down to 400 nK and higher densities of $1 \times 10^{12}\,\mathrm{cm}^{-3}$.

3.3 Imaging Techniques

Imaging the MOT following each experimental sequence allows the atom numbers, density, cloud width and position to be determined. In this thesis absorption imaging on the $5s^2\ {}^1S_0 \rightarrow 5s5p\ {}^1P_1$ is used throughout, using a resonant 461 nm probe beam. The probe beam has a $1/e^2$ radius of 2.5 mm and 2 mW of power, while the camera used for imaging is a PixelFly QE camera. Florescence images of the MOT can also be obtained using the 461 nm MOT beams, however the high density narrow-line MOT is optically thick meaning only atoms in the outer shell are imaged with this technique.

A standard absorption image with the probe beam still does not allow the true optical depth (OD) to be obtained. We find that an OD of > 5 cannot be accurately measured due to the noise floor of the camera. Strong saturation absorption imaging has been used in other experiments investigating dense clouds [97]. However as the transition saturation intensity is $40\,\mathrm{mW\,cm}^{-2}$, sufficient probe light is not available in our experiment. Instead two alternative methods can be employed to deal with the high optical depth.

The first technique relies on the assumptions that the cloud has a Gaussian distribution and is radially symmetric. The saturation of the camera can then be accounted for through fitting to the wings of the cloud. This method was developed in [85], and an example of such fitting is shown in the top row of Fig. 3.6.

Another method for imaging dense clouds is to first shelve a fraction of atoms by pulsing on the 688 nm laser and 689 nm probe. As shown in Fig. 3.3 this shelves atoms in the $5s5p\ {}^3P_J$ states before imaging. This reduces the optical

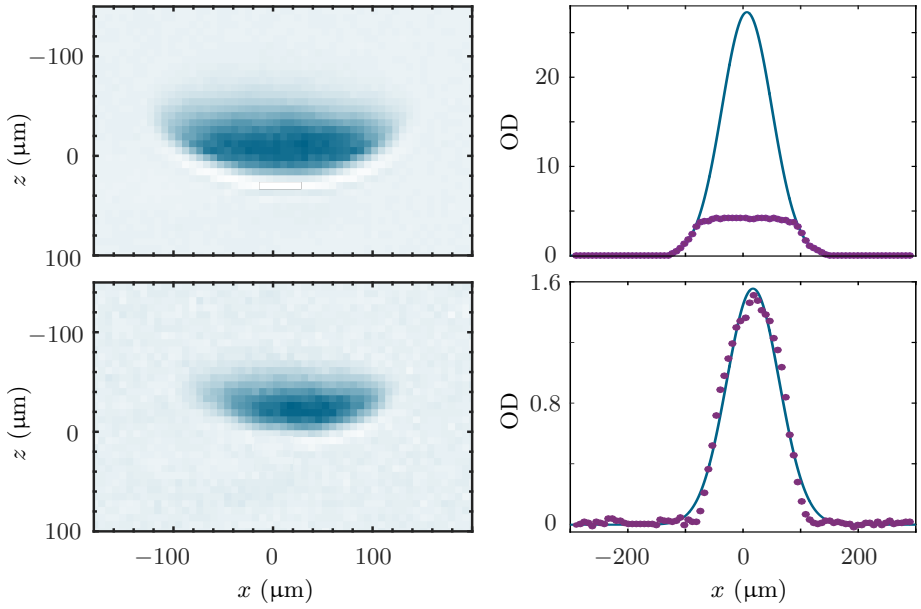

Figure 3.6: Top row shows both an absorption image of a dense MOT alongside a cross section taken through the centre of the distribution (purple circles), where b is the optical depth. The blue lines show a Gaussian fit to the wings of this cross section. The bottom row shows an absorption image for the same density following shelving with the 688 and 689 nm lasers, where again a cross section through the cloud is fitted to a Gaussian distribution.

depth, allowing standard analysis of the images without relying on the fitting method outlined above. Comparisons of a MOT with and without a shelving pulse in Fig. 3.6 show this technique can lead to a cloud which is no longer optically thick.

The shelving fraction depends critically on both the pulse length and laser power. We typically work with powers of around 4 mW at 688 nm and 2 mW at 689 nm, and select the shelving ratio by varying the pulse length. Fig. 3.7(a) shows the peak OD (obtained from the wing-fitting method at high densities) for different pulse lengths. We find that for our highest achievable densities, a pulse length of $\sim 1\,\mu$s sufficiently reduces the OD.

To determine the shelving fraction, the atom number/peak OD in a low density MOT, both with and without shelving are compared. Here the density should be low enough that the wing fitting method is not required. The top graph in Fig. 3.7(b) shows a cross-section of the OD through the

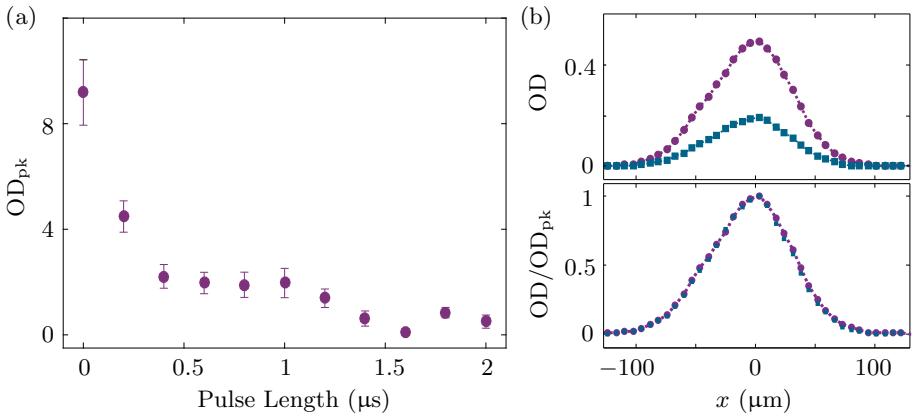

Figure 3.7: (a) Peak optical depth (OD_{pk}) as a function of the shelving pulse length. (b) Top: Calibration experiment in a low density MOT. Taking a cross-section through the cloud the OD is shown both without (purple circles) and with (blue squares) a 1 μs shelving pulse. Bottom: The OD is normalised by OD_{pk}, and the same cross-section is plotted as in the top graph (with and without the shelving pulse).

cloud both with and without a 1 μs shelving pulse. From this the shelving ratio can be obtained, where in this case $\sim 40\,\%$ of the atoms were shelved. As the shelving ratio varies with both beam power and pulse length, the shelving fraction is measured before each experimental run. The bottom graph in Fig. 3.7(b) show same cross-sections as in (a) normalised by the peak OD. From this it is clear that the cloud shape remains unchanged after applying the shelving pulse. We find that at high densities the atom numbers obtained using both techniques (shelving and wing fitting) agree within the uncertainties of the measurement.

However, the shelving method is particularly useful for the dressing experiments of chapter 6, when the cloud may no longer have a Gaussian distribution. Instead the atom number, N, can be determined directly from the summed optical depth as

$$N = \frac{A_{\text{pixel}}}{\sigma_0} \sum OD, \tag{3.1}$$

rather than relying on the fitted widths. Here A_{pixel} is the area per pixel and $\sigma_0 = 3\lambda^2/2\pi$ is the absorption cross-section. Throughout this thesis both

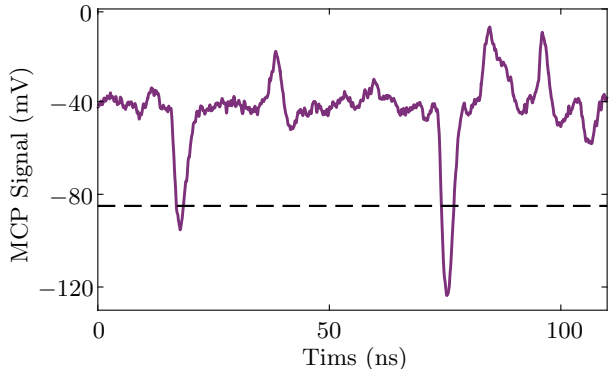

Figure 3.8: MCP signal voltage as a function of time is given by the purple trace. The black dashed line shows the voltage threshold level at which an ion event is recorded.

techniques are used, where chapter 5 mainly uses the wing fitting technique, and chapter 6 uses both methods as required.

3.4 Ion Detection

To detect Rydberg atoms, the atoms are ionisied following Rydberg excitation, and the resulting ions are detected on an MCP. While it is possible to employ field ionisation using the chamber electrodes (as in most other alkali Rydberg groups [98]), instead we use a method known as autoionisation. This technique involves using the second valence electron in strontium. After exciting the first electron to a Rydberg state, the second electron is excited using the 408 nm laser. This process is known as 'isolated core excitation' [95], and results in a doubly excited state with more energy than the first ionisation threshold. Following 'isolated core excitaition' the Rydberg atom quickly ionises ($\sim$ 10 ps) with a high probability. In addition to driven ionisation (autoionisation), uncontrolled ionization also occurs in our experiment. The are many causes for the production of these ions, as the Rydberg atoms are close in energy to the ionisation threshold, hence only a small perturbation is required for them to ionise. Throughout this thesis this process is referred to as spontaneous ionisation.

Following autoionisation a voltage is applied to five of the electrodes to steer

the ions towards the MCP. The MCP front plate is held at −100 V, while the back plate is held at −2 kV. This is all shielded by a charged grid (−20 V), which helps to reduce the stray field generated by the MCP. On reaching the MCP individual ions create voltage spikes, which are counted using a fast oscilloscope (LeCroy 610Zi). Events are recorded as the number of times the MCP voltage crosses a certain threshold. Two such events are shown in Fig. 3.8, where the voltage threshold is around −80 mV. The oscilloscope also allows time-resolved ion detection, where different arrival times let us distinguish between the spontaneous and autoionising signals. Turning on the guiding field before application of the 408 nm laser means that spontaneously ionised atoms arrive before the autoionised signal is detected.

It is also important to note the maximum detection efficiency for this system. The efficiency is firstly limited by the grid which is only 40 % transmissive, and is further limited by the threshold at which ions are recorded. Ions which reach the MCP have a 60 % probability to be recorded, leading to an overall efficiency of 24 %. Further details on the autoionising process can be found in [82, 83, 91].

Chapter 4

Rydberg Spectroscopy Apparatus

In this chapter we describe and characterize the apparatus required for absolute frequency measurements of strontium Rydberg states. The development of a laser source at 319 nm for Rydberg excitation and spectroscopy of the triplet Rydberg series is described in detail. In order to obtain a transition energy we use a frequency comb to measure our laser frequencies. The frequency comb is a commercially available system from Toptica Photonics, and here an overview of the system is given along with the method for detecting beat notes with our lasers. Finally the long-term frequency stability of both our 689 and 319 nm laser systems is measured through Allan deviation measurements with the comb.

4.1 Rydberg Excitation Laser

A description of the UV laser system described in this section was published in [58]. The laser system allows two-step excitation of strontium Rydberg states from either the 5s5p $^3P_0$ and 5s5p $^3P_1$ intermediate states. For our purposes we required a narrow linewidth laser, on the order of 10 kHz, to coherently drive narrow transitions. The laser system needed to be suitable

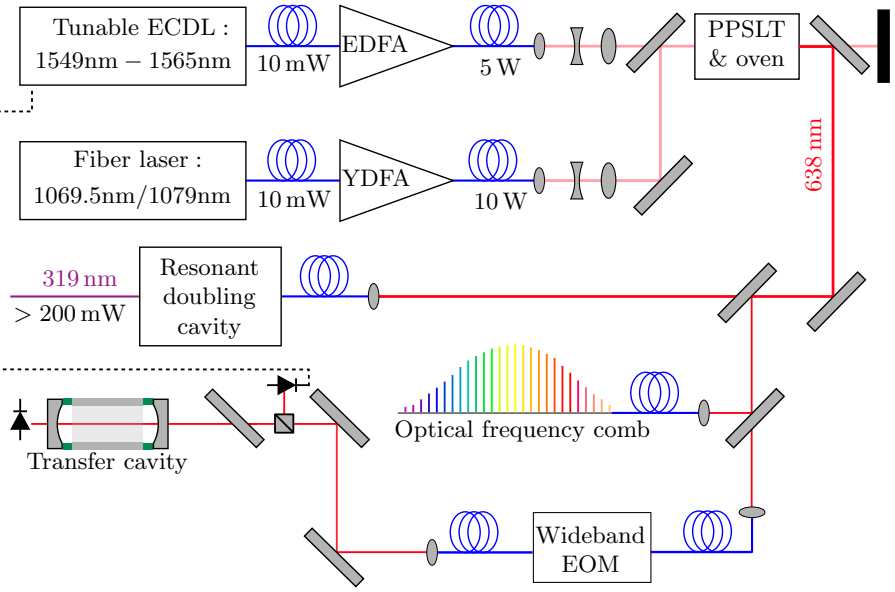

Figure 4.1: Schematic of 319 nm laser system. A PPSLT crystal is used to sum the frequencies of two infra-red lasers, to generate light at 633 nm – 639 nm. This is subsequently frequency doubled to produce > 300 mW in the UV. The laser frequency is locked to an optical transfer cavity stabilized to the $5s^2\ {}^1S_0 \rightarrow 5s5p\ {}^3P_1$ intercombination line in Sr at 689 nm. A wideband electro-optic modulator (EOM) is used to bridge the frequency gap between the cavity mode and the Rydberg transition. The laser frequency is measured on a GPS-referenced optical frequency comb.

for exciting to a large range of Rydberg states in the triplet series of strontium (i.e. have a large tunability). Furthermore, high powers of > 100 mW were necessary for off-resonant Rydberg dressing, since the coupling matrix elements are weak. The approach we used for achieving these requirements is presented in the following sections.

4.1.1 Laser Construction

The overall design of the laser system is shown in Fig. 4.1 and is based on a similar system described in [99]. Here two infra-red seed lasers are amplified and combined using sum frequency generation (SFG) in a periodically-poled stoichiometric lithium tantalate (PPSLT) crystal to produce 1.6 W of red light from 633 nm to 639 nm. Subsequently, UV light is produced using

resonantly-enhanced second harmonic generation (SHG). A small amount of the 638 nm light (<1 mW) is used to lock to a high finesse optical cavity producing narrow linewidths. Additionally we pick off $\sim$ 5 mW for frequency measurements with a GPS-referenced optical frequency comb.

As shown in Figure 4.1 we use two commercial fiber amplifier systems, with central wavelengths of 1560 nm and 1079 nm, to generate high fundamental power over our required range of wavelengths. The Er-doped amplifier (Manlight[1]) produces up to 5 W over the wavelength range 1549 nm $\rightarrow$ 1565 nm, while a Yb-doped amplifier (Nufern[2]) produces up to 10 W over 1064 nm $\rightarrow$ 1083 nm.

In order to switch between the 5s5p $^3P_0$ and 5s5p $^3P_1$ intermediate states, which have a 5.6 THz frequency difference, we employ two different seed lasers. These are centered at 1069.5 nm or 1079.0 nm respectively, where both have a narrow linewidth of $\sim$10 kHz. These lasers are high stability fiber lasers (NP Photonics) with polarization-maintaining single-mode optical fiber outputs. Our required tunability is achieved by using a highly tunable external cavity diode laser (Toptica ECDL) as the other 1550 nm seed laser. This seed laser has a broader linewidth of $\sim$100 kHz, but the frequency can be tuned over the whole usable gain bandwidth of the fiber amplifier.

4.1.2 Sum Frequency Generation

Frequency conversion in a nonlinear optical material allows for SFG of the infra-red wavelengths generating light at 633 nm – 639 nm, which can be subsequently doubled to our required UV wavelength. For the SFG process, both infra-red beams are spatially overlapped and make a single pass through the PPSLT crystal. Before the crystal, the beams are independently mode-matched using a combination of lenses, and then overlapped

[1] ML5-EYFA-CW-SLM-P-TKS

[2] NuAMP high power, polarization maintaining fiber amplifier: NUA-UUUU-PV-0010-YZ

using a dichroic optic. The mode-matching lenses have focal lengths of $f_{1a} = -50\,\text{mm}$ and $f_{1b} = 50\,\text{mm}$ for the 1550 nm beam and $f_{2a} = -100\,\text{mm}$ and $f_{2b} = 100\,\text{mm}$ at 1079 nm. After the crystal, the output beam and IR beams are separated using dichroic mirrors, and the unused IR power is sent to a beam-dump.

The PPSLT crystal (Laser 2000) we employ for SFG of the infra-red beams contains five channels, each with a different poling period across its 15 mm width. The crystal has a length of 50 mm, with a thickness of 1 mm, and is mounted in a heater to allow control of the crystal temperature to 0.1 °C. In order to maximize the efficiency of the nonlinear frequency conversion, the process should be quasi-phased-matched over the range of wavelengths required for our experiment. The phase mismatch as a function of temperature [100] is calculated using the extraordinary refractive index [101], n_i as:

$$\Delta k(T) = 2\pi \left(\frac{n_{out}}{\lambda_{\text{out}}} - \frac{n_2}{\lambda_2} - \frac{n_1}{\lambda_1} - \frac{1}{\Lambda} \right), \tag{4.1}$$

where $\lambda_{1,2}$ refer to input wavelengths, λ_{out} the generated wavelength and Λ describes the poling period of the crystal. Note both n_i and Λ are temperature dependent. From this equation we find that for poling periods between 13.05 µm and 13.45 µm, crystal temperatures in the range of 100 °C to 140 °C provide quasi-phase-matching across the full Rydberg series for $n > 32$. Table 4.1 highlights the wavelength tuning range of the laser, along with the Rydberg states accessible from both the 5s5p $^3P_0$ and 5s5p $^3P_1$ intermediate states.

As described in [102], for optimal frequency conversion the confocal parameter inside the crystal, b, of the input beams should be related to the length of the nonlinear crystal L as $\epsilon = \text{L/b} = 2.84$. Here $b = 2z_r$ where $z_r = \pi n \omega_0^2/\lambda_0$, n is the material refractive index, ω_0 is the beam waist and λ_0 the beam wavelength. Therefore due to the high refractive index n of the crystal, the value for b is quite different to that of the beam in air. A cage system was set-up for the lenses to allow some adjustment of the ϵ value, but we have observed the conversion efficiency to be relatively insensitive

Intermediate State	Rydberg n	λ_1 (nm)	λ_2 (nm)	λ_{uv} (nm)
$^3P_0$	32 - 320	1549 - 1565	1069.5	316.3 - 317.7
$^3P_1$	35 - ∞	1549 - 1565	1079	318 - 319.3

Table 4.1: The principal quantum numbers n of the strontium Rydberg states accessible from both intermediate states. Here wavelengths λ_1 and λ_2 are combined using SFG. Following this the light is frequency doubled to give the desired wavelength, λ_{uv}.

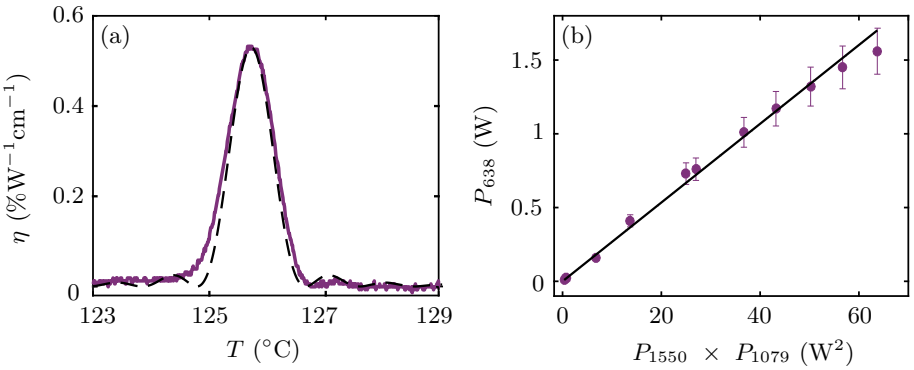

Figure 4.2: (a) Dependence of the SFG efficiency on PPSLT crystal temperature. The measured data (purple) is shown with the prediction from equations 4.1 and 4.2 (black dashes). A small temperature offset (0.55 °C) has been added to the prediction plot to match the experimental data. (b) Output power (P_{638}) of the SFG process for a range of input powers ($P_{1550} \times P_{1079}$). Data points are shown as purple circles, and the black line shows the least squares linear fit to the data.

to this parameter. In our case we work with a lower value of $\epsilon = 1.56$ in order to reduce the constraint on the overlap of the beam waists in the axial direction. The overall SFG conversion efficiency, η, depends on both the phase mismatch Δk, and the crystal length L, from the following relation:

$$\eta \propto \frac{\sin^2(\Delta k L/2)}{(\Delta k L/2)^2}. \tag{4.2}$$

From equation 4.1, Δk is shown to have a temperature dependance, therefore the conversion efficiency critically depends on the crystal temperature. The relation in equation 4.2 predicts that η will follow a sinc^2 function with

temperature. This is demonstrated in Fig. 4.2(a) for our laser system, where the black dashed line is the expected curve from equations 4.1 and 4.2, and the purple line is the experimental data. The temperature dependence describes a crystal temperature acceptance bandwidth, where we observe a feature with a full width half maximum (FWHM) of $\sim 1\,^{\circ}\mathrm{C}$. This shows the need for our precise control over the crystal temperature, where in our case the temperature resolution of $0.1\,^{\circ}\mathrm{C}$ is sufficient to stabilize the temperature for optimal conversion efficiency i.e. on the peak of Fig. 4.2(a).

Our system obtains a maximum output power of 1.6 W from the SFG process as shown in Fig. 4.2(b), illustrating the output power, P_{638}, as a function of the product of input powers, P_{1550} and P_{1079}. From this graph the conversion efficiency of the crystal can be calculated using the following equation:

$$\eta = \frac{P_{638}}{P_{1550}P_{1079}L}. \tag{4.3}$$

The output power is seen to have a linear dependance on the product of input powers, and the least squares fit to the data in Fig. 4.2(b) (black line) results in a normalized conversion efficiency $\eta = 0.53 \pm 0.02\,\%\mathrm{W}^{-1}\mathrm{cm}^{-1}$. This value is favourable compared to other reported conversion efficiencies for PPSLT, which typically range from 0.3 to $0.4\,\%\mathrm{W}^{-1}\mathrm{cm}^{-1}$ [103–105]. However higher powers could be achieved by instead using a periodically-poled lithium niobate (PPLN) crystal where typical conversion efficiencies are $2.8\,\%\mathrm{W}^{-1}\mathrm{cm}^{-1}$ [106, 107]. The reason we initially decided on a PPSLT crystal was due to the lower light-induced infra-red absorption and higher photo-refractive damage threshold when compared to PPLN [103, 108]. However due to our requirement for high power the system is currently undergoing an upgrade to a PPLN crystal. Following this upgrade the generated power at 638 nm should be $> 5\,\mathrm{W}$ leading to a final UV power of $> 2\,\mathrm{W}$. This will be particularly useful for the Rydberg dressing experiments of chapter 6, as it results in much higher Rabi frequencies.

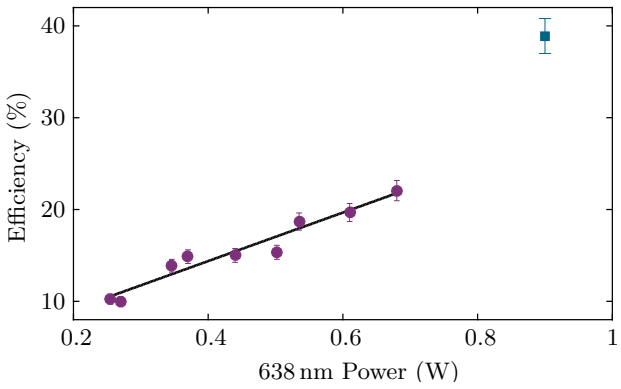

Figure 4.3: Efficiency of power conversion from 638 nm light to 319 nm as a function of input power following second harmonic generation in a nonlinear crystal. Before a cavity and fibre upgrade (purple circles) the trend shows linear dependence. After upgrading the system (blue square) a maximum efficiency of $\sim 40\,\%$ was achieved.

4.1.3 Frequency Doubling

We require the output light from the SFG process to be frequency doubled to generate the required UV wavelength. Most of the light following SFG is sent into a high power, polarization maintaining, single-mode optical fiber. Around $\sim 5\,\mathrm{mW}$ is picked off before the fibre, where $< 200\,\mu\mathrm{W}$ is used for locking to a high finesse cavity and the rest is sent to another laboratory for measurements with an optical frequency comb.
The output from the high power fibre is sent to a commercial frequency doubling unit from Toptica Photonics. The system contains a nonlinear crystal optimised for second harmonic generation (SHG), where the crystal is placed in a hermetically sealed bow-tie cavity. Here Pound-Drever-Hall (PDH) locking sets the cavity length through feedback to a piezo-mounted mirror.

The power conversion efficiency as a function of the input power at 638 nm is shown in Fig. 4.3. As expected, there is a linear trend in the conversion to UV, and typically for maximum input power $> 20\,\%$ was converted to UV power following SHG. During this work the frequency doubling system suffered some problems, where the maximum conversion dropped to $\sim 10\,\%$ and a maximum UV power of 80 mW. As a result a new cavity was in-

stalled which greatly increased the conversion efficiency beyond what had been measured before. The maximum achieved efficiency from the new cavity is shown as an additional data point in Fig. 4.3, and resulted in a power of 350 mW.

During this time the high power fibre at 638 nm was also changed as we observed large fluctuations at the output when running the system at maximum power. This problem was associated with the process of Brillouin scattering, which arises from the interaction between an optical and an acoustic wave [109]. The threshold power above which Brilloun scattering occurs is strongly influenced by the fibre geometry [110]. It has been shown that there is a higher threshold power associated with photonic crystal fibres, compared to conventional single-mode fibres [110–112]. For this reason a photonic crystal fibre was implemented into our set-up, which successfully reduced the power fluctuations to <10 % at maximum power.

4.1.4 Short-term Frequency Stabilisation

In our experiment, a high-finesse optical cavity narrows the linewidth of our 689 nm ECDL laser as outlined in chapter 3, and is used to cool atoms in a narrow-line MOT. For the UV laser system, we use the same cavity for frequency stabilisation of the 638 nm light before frequency doubling. In this section the locking techniques and frequency stability of both lasers are detailed.

PDH Locking

Both cavity locks at 689 nm and 638 nm use the Pound-Drever-Hall (PDH) locking method. However the 638 nm lock uses a slight modification from the standard PDH known as electronic sideband locking. Both methods have been explained in detail in other references [92, 93, 113]. Here an overview of the locking methods and frequency stability of both lasers are given.

The cavity lock at 689 nm, briefly introduced in chapter 3, uses standard PDH locking. The method first relies upon phase modulating the light in-

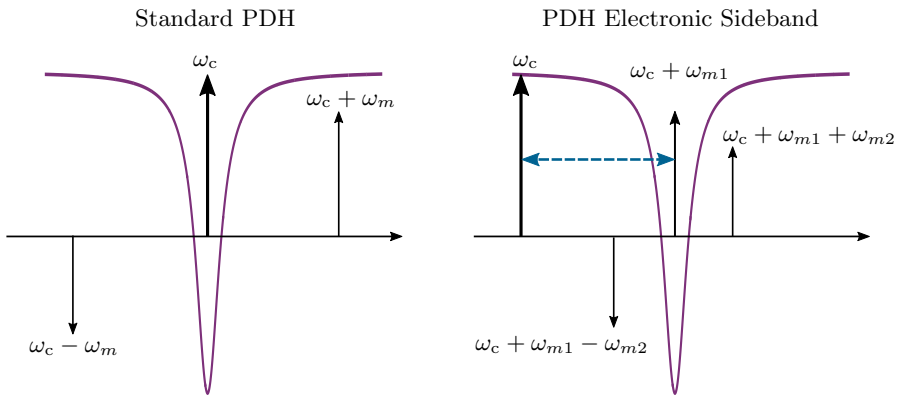

Figure 4.4: The two PDH methods used for locking the 689 nm (left) and 638 nm (right) lasers to the optical reference cavity. The arrow direction shows the relative phase, and the solid line (purple) shows the reflected power. For the electronic sideband technique the adjustable frequency spacing is highlighted by the dashed line (blue). Note that only the frequency components to the right of the main carrier ω_c are shown in this case.

cident on the cavity so that sidebands are created to either side of the main carrier frequency. This is achieved using an electric-optic modulator (EOM) with a modulation frequency of ω_m. The lock then requires examining the reflected light from the cavity on a photodiode. The resulting PDH error signal is obtained by demodulating the output at ω_m.

The cavity length is stabilised using a saturated fluorescence signal on the 5s5p $^3P_1$ transition, where feedback is provided to the cavity via piezo mounted mirrors. For this reason if we use the standard PDH technique for our 638 nm light, the atom-referenced cavity mode will not necessarily be at a frequency suitable for driving a Rydberg transition. This is why the electronic side-band technique is employed [113], and the main differences between both techniques are highlighted in Fig. 4.4.

For locking the UV laser frequency, a small pick-off of light at 638 nm is overlapped with the 689 nm beam on a dichroic filter (as in Fig. 4.1) providing alignment into the same optical cavity. Frequency stabilisation of the light using the electronic side-band method requires locking a tuneable sideband at detuning ω_{m1} to cavity resonance, rather than the main carrier frequency at ω_c. A fiber-coupled wideband EOM is used to offset-lock the

laser frequency from that of the cavity mode. The carrier frequency of the EOM ω_{m1} can range from 0.1 to 5 GHz, and is phase modulated at a frequency $\omega_{m2} = 8$ MHz to produce modulation sidebands for PDH locking. The different modulation frequencies at 689 and 638 nm (10 and 8 MHz) prevent cross-talk between the locks. The standard PDH error signal is the obtained through demodulation at ω_{m2}, locking the laser at a frequency ω_{m1} away from ω_c (cavity mode). The error signal is sent to a fast analogue servo module (Toptica[3]) which is integrated into the control electronics.
Using this method the frequency can be shifted while remaining locked to the cavity by adjusting the main drive frequency of the EOM (ω_{m1}). Varying ω_{m1} in small steps (~ 25 kHz) during an experimental sequence allows us to obtain the Rydberg spectra shown in this thesis. Following optimisation of the locking parameters, laser frequency shifts of ~ 5 MHz are observed with the light remaining locked to the cavity (or quickly re-locking).

Fine Tuning Lock Parameters

For optimising the locking parameters of the fast analogue servo module (FALC 110) the in-loop locked error signal is observed on a spectrum analyser. This requires picking off the error signal at the input to the FALC using a directional coupler, where the resulting spectrum is shown in Fig. 4.5. When the laser is stabilised to the cavity, the noise from the laser is deposited away from ω_{m1}, and results in a central peak with sidebands at a particular frequency that depends on the loop parameters. Increasing the loop gain results in pushing the sidebands further away from ω_{m1}, increasing the lock bandwidth. However too much gain results in loop instabilities, with the sidebands decreasing in amplitude. By optimising the loop parameters we ensure that the bandwidth is a large as possible, where Fig. 4.5 shows the optimal spectrum achieved. Here the bandwidth obtained is 0.25 MHz. Note that this bandwidth changes with the laser's operating parameters, such as the TEM_{mn} mode used for locking, power on the photodiode and the laser

[3] Fast Analog Linewidth Control Module: FALC 110

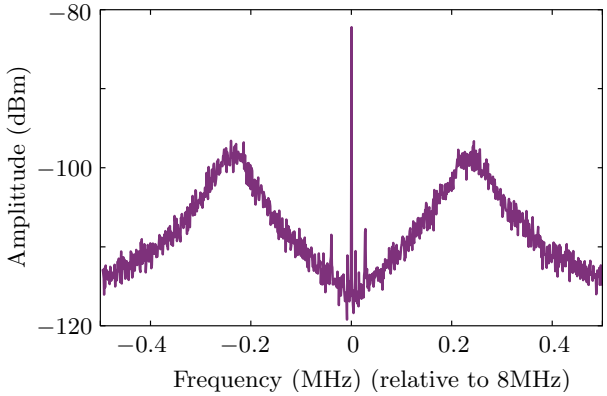

Figure 4.5: In–loop locked error signal noise observed on an RF spectrum analyser centred about the modulation frequency of 8 MHz. The noise sidebands peak at a frequency of $\sim \pm$ 0.25 MHz, indicating the servo bandwidth.

mode hop free range.

Cavity Finesse

In [84] the finesse, F of the cavity for 689 nm light was measured as a high finesse is desirable to ensure we can obtain the narrow linewidths needed for our experiment. A finesse measurement at 638 nm was carried out for comparison, where F depends on mirror quality, i.e. mirror reflectivity R. The reflectivity R and hence the finesse will vary for different wavelengths. F is defined as:

$$F = \frac{\pi\sqrt{R}}{1-R}. \tag{4.4}$$

R $\sim$ 1 for our cavity, where we use mirrors from Layertec which have a reflectivity of >99.99 % at our required wavelengths. The finesse is related to the cavity resonance linewidth δv and free spectral range Δv_{FSR} of the cavity,

$$\delta v = \frac{\Delta v_{\mathrm{FSR}}}{F}. \tag{4.5}$$

Here $\Delta v_{\mathrm{FSR}} = c/2nL$, where n is the refractive index of the gas between the mirrors, c is the speed of light and L the cavity length. Our cavity has a $\Delta_{\mathrm{FSR}} \sim 1.5$ GHz as determined in [84]. Determining the finesse of a cavity is possible by performing a cavity ring-down measurement, which measures

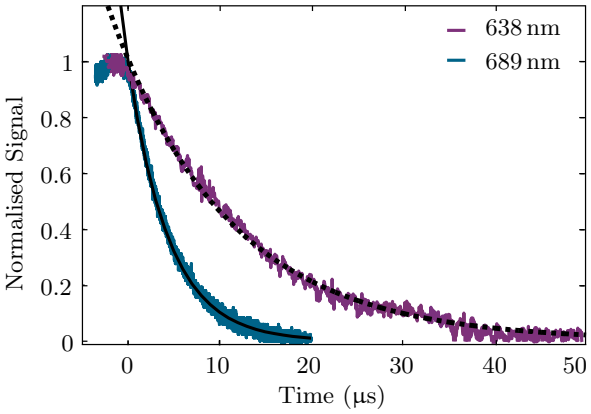

Figure 4.6: Cavity ring-down measurement of the high-finesse optical cavity at 638 nm (purple) and 689 nm (blue), the latter taken from [84]. Also shown are exponential fits for both cases (black dashed and black solid line) with decay times of 12.62 ± 0.05 μs and 4.39 ± 0.05 μs for 638 nm and 689 nm respectively.

the average photon lifetime inside the cavity. By quickly turning off the light source to the optical cavity, the intensity of the trapped light pulse decreases by a fixed amount during each round trip, where the decay time, τ, is the time taken for the power to become 1/e of its original value. The decay rate of light intensity from the cavity takes the form of exponential decay where

$$I(t) = I_0 e^{-\frac{t}{\tau}} \tag{4.6}$$

As the cavity resonance linewidth δv, can be written in terms of τ as $\delta v = 1/2\pi\tau$ we can rewrite equation 4.5 as

$$F = 2\pi\tau\Delta v_{\mathrm{FSR}} \tag{4.7}$$

The results from ring-down measurements at 689 nm and 638 nm are shown in Fig. 4.6. Here decay times of 4.39 ± 0.05 μs at 689 nm and 12.62 ± 0.05 μs at 638 nm are calculated from fits to the data. This leads to a finesse of $(413 \pm 6) \times 10^2$ and $(118.9 \pm 0.5) \times 10^3$ respectively. The larger finesse at 638 nm is a result of the mirrors having a slightly higher reflectivity at this wavelength. From equation 4.4 this corresponds to a change in reflectivity of just 5×10^{-5} between the two wavelengths. Our cavity has a $\Delta_{\mathrm{FSR}} \sim 1.5$ GHz leading to cavity resonance widths δv (equation 4.5) of 35 kHz and

13 kHz. As a result a locked laser linewidth of < 10 kHz is feasible at both 689 and 638 nm. Performing the same measurement at 689 nm, but with the new ULE cavity (see chapter 3) yields a finesse of $(236.1 \pm 0.5) \times 10^3$, with $\delta v = 6.4$ kHz.

Short-term Laser Linewidth

For our laser system it is difficult to measure an absolute laser linewidth on short–interrogation times. The usual method requires a beat measurement in the frequency domain to diagnose and reduce the dominant noise sources. Two methods can be used for making such a beat measurement. The first is the self-heterodyne measurement [114], requiring a 10 km single-mode polarisation maintaining delay fibre, to mix the optical field with a delayed replica of itself. The linewidth is then inferred from the recorded power spectrum of the fluctuations in the detected signal. The second method relies on having two identical laser systems in order to make a beat measurement between them. Both methods are not feasible as we do not have access to the necessary equipment.

An alternative method described in [84] was used to determine the performance of the 689 nm laser system, estimating the short-term linewidth as $\sim$ 1.5 kHz. This approach involved measuring the short-term frequency noise by looking at the spectrum of the in-loop PDH error signal. Here we use this same method to estimate the short-term frequency instability for the 638 nm laser. For more detail on the procedure refer to [84].

Here we start by assuming the laser noise is Gaussian, and hence the noise ν_n can be estimated as [93] :

$$\nu_n = \frac{2.355 V_{\text{rms}}}{D} \tag{4.8}$$

where D is the PDH discriminator gradient and V_{rms} the root-mean-square of the locked error signal. We calculate D as V_{pp}/δ_v, with V_{pp} the peak-to-peak amplitude of the PDH error signal. Estimating the laser noise at different sample times using equation 4.8 results in fractional frequency in-

stabilities of $< 4 \times 10^{-12}$, corresponding to frequency deviations of $< 4\,\mathrm{kHz}$ in the UV.

For long-term frequency stability analysis, Allan deviation measurements are performed using the GPS referenced frequency comb. This analysis is discussed in a later section after first introducing the frequency comb system.

4.2 Frequency Comb System

By referencing our Rydberg excitation lasers to an optical frequency comb we can perform absolute frequency measurements of Sr Rydberg states. Recently, frequency comb systems have become commercially available devices [115, 116], where frequency doubling allows visible operation. The frequency comb we use was developed by Toptica Photonics and allows absolute measurement at our required frequencies through hetrodyne beat measurements between our lasers and a nearby comb line [59].

4.2.1 Measuring Optical Frequencies

The general output of a frequency comb generated by a mode-locked femtosecond laser is shown in both the time and frequency domain in Fig. 4.7. The short pulses are usually generated either using Ti:Sapphire oscillators [117, 118] or erbium doped fiber oscillators [119, 120]. An offset, $\Delta\phi$, arises due to to dispersion and nonlinearities causing a slip of the carrier envelope offset. After each round trip the phase slip between the carrier and the pulse envelope increases as depicted in the Fig. 4.7(a). Measuring this offset frequency usually involves a f-to-$2f$-interferometer approach [121]. However, in our system f_{ceo} is eliminated through a technique known as difference frequency generation (see section 4.2.2).

The repetition frequency of the pulses, f_{rep}, is related to the round trip time of the laser cavity, $T_r = 1/f_{\mathrm{rep}}$. The light from the mode-locked laser contains strong frequency components spaced by f_{rep} (Fig. 4.7(b)), where the n^{th} tooth of the frequency comb is defined as:

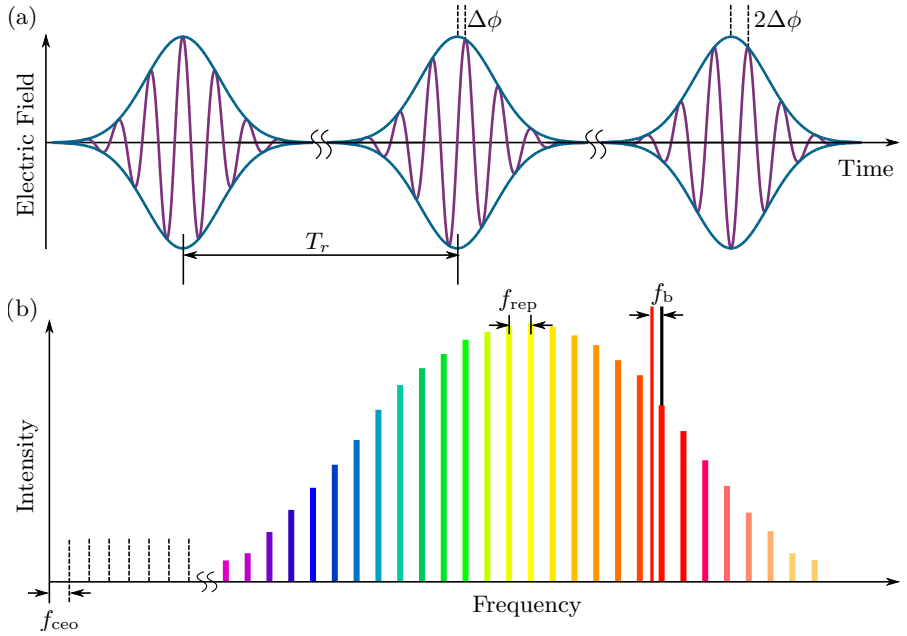

Figure 4.7: (a) Pulse train emitted by a mode-locked laser with the phase slip $\Delta\phi$, between the carrier phase (purple) and the pulse envelope (blue) . (b) Spectral representation of a frequency comb in the frequency domain. The spectrum is defined by f_{rep} and f_{ceo}. To measure an optical frequency f_b is obtained by beating a laser with a comb tooth.

$$f_n = n f_{\text{rep}} + f_{\text{ceo}} \tag{4.9}$$

where f_{ceo} is the carrier offset frequency. This means that once f_{rep} and f_{ceo} are known, the absolute frequency of the comb lines can be obtained. Using such a system unknown optical frequencies can then be determined by measuring the beat note, f_{b}, between a laser and comb line.

4.2.2 The Difference Frequency Comb

The Toptica frequency comb uses a technique known as difference frequency generation (DFG) in order to eliminate the f_{ceo} term in the expression for the frequencies of the comb modes (see equation 4.9) [115]. The general layout of the comb is shown in Fig. 4.8. This comb relies on first generating a more than octave-spanning super-continuum with a low noise Er-fiber

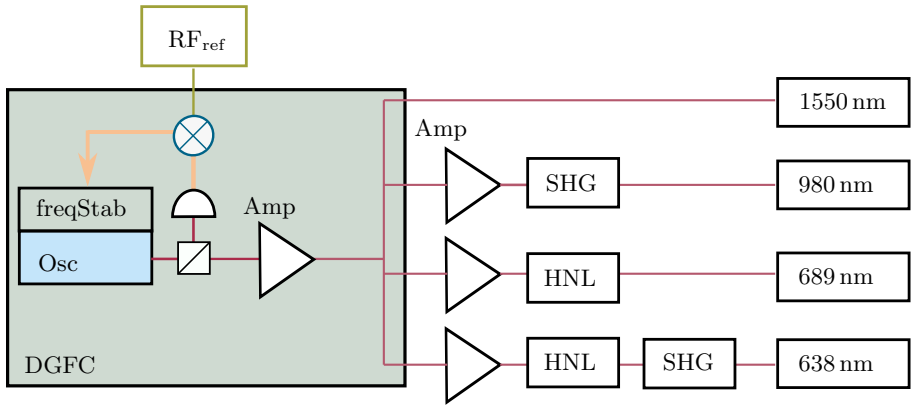

Figure 4.8: Frequency comb setup taken from [59]. The difference frequency comb (DFG-FC) delivers an f_{ceo} free spectrum that can be locked to an RF reference providing an absolutely stable frequency comb. The stable frequency comb can subsequently be converted to the desired wavelength outputs through a combination of second harmonic generation (SHG) and highly non-linear frequency shifting (HNL).

oscillator. The spectrum is then amplified and broadened in a highly non-linear fiber to include 850 nm and 1880 nm. Performing DFG between these two extreme parts of the supercontiuum results in an f_{ceo}-free spectrum at 1550 nm. DFG is achieved though spatially and temporally overlapping the beams in a PPLN nonlinear crystal. More detail on the setup can be found in [115]. The process generates coherent mixing of two sets of multiple comb lines with integer multiples n and m of f_{rep}. Therefore from equation 4.9 the contribution to a single line of the DFG spectrum is given as:

$$f_n - f_m = (n - m) f_{rep} + f_{ceo} - f_{ceo} \tag{4.10}$$

therefore

$$f_{\bar{n}} = \bar{n} f_{rep}. \tag{4.11}$$

This method has distinct advantages when compared with the conventional f-to-$2f$-interferometer approach where high frequency noise components of f_{ceo} cannot be canceled [122]. The f_{rep} at 80 MHz is locked to ultra-low-noise oven-controlled RF oscillator at the 10^{th} harmonic at 800 MHz. This is in turn locked to a GPS disciplined RF oscillator [123]. The stable frequency

comb can then be extended to different wavelengths by nonlinear frequency shifting and frequency doubling, generating outputs at 1550 nm, 980 nm, 638 nm and 689 nm as shown in Fig. 4.8. For our experiment the outputs at 638 nm and 689 nm allow us to produce beat notes with both of our narrow linewidth lasers used for Rydberg excitation.

4.2.3 Beat Detection

Detecting the beat note between a continuous-wave (cw) laser and comb tooth is accomplished by two units: a beam combiner and detector. Both the comb and cw light are fibre coupled to the separate input couplers of the combiner. We typically work with 3 mW of 638 nm and 689 nm light respectively, however it is possible to increase this power if required. The comb power at these wavelengths is 2.5 mW and 1.4 mW respectively. Within the combiner unit the comb is superimposed with the cw laser, and a quarter wave-plate in the unit allows the relative intensities between both beams to be adjusted. The monochromatic detector then uses a grating-based adjustable filter to select a narrow spectrum, a few GHz wide at the beat note between the cw laser and frequency comb. The filter reduces the optical power of neighboring comb lines that do not contribute to the beat note in order to avoid saturation of the low-noise photo-diode. The output signal is then sent to a suitable device (i.e. spectrum analyser/frequency counter) for measuring the beat frequency.

Fig. 4.9 shows the signal direct from the photo-diode on a spectrum analyser for a 638 nm beat note. At $\sim$ 6.5 MHz there is a clear beat note, but a number of other peaks are visible. As the laser will beat with more than one comb line, we can see two other beat notes between the laser and comb to either side of the peak at 80 MHz. The 80 MHz peak is a comb with comb beat, and appears at multiples of f_{rep}. For the beat signal obtained between the cw laser and comb, a Lorentzian fit describes the lineshape, as shown in the inset of Fig. 4.9. Here the FWHM is limited by the comb linewidth (rather than our lasers) and gives a value of 378 ± 9 kHz.

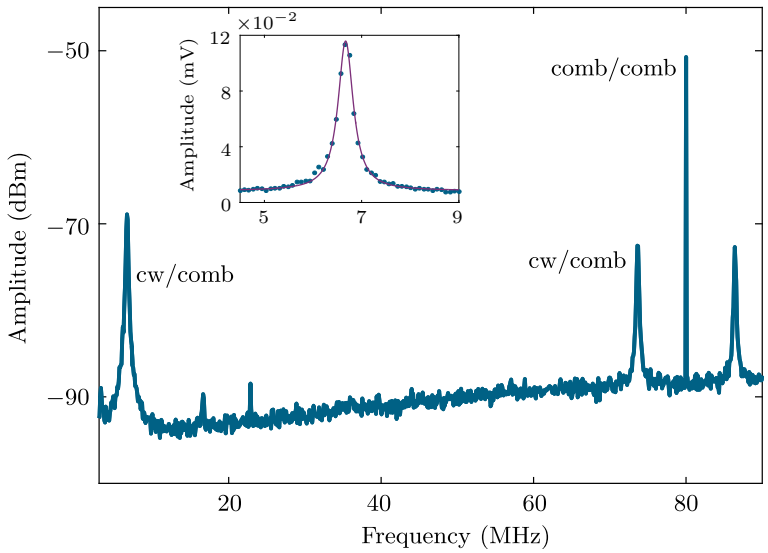

Figure 4.9: Signal from the beat note photodiode measured on a spectrum analyser over a span of 90 MHz. Inset shows a lorentzian fit to the beat note at 6.5 MHz, where the FWHM is 378 ± 9 kHz.

For the purposes of measuring our beat note accurately on a frequency counter, we select a single beat note by adding an appropriate low-pass filter. An amplifier is also added to the set-up to increase the beat amplitude. It is important to characterise the requirements of the counter to determine the signal necessary for correct frequency readings. For beat frequencies below a certain threshold of signal-to-noise ratio (SNR) and signal power level we observe errors in the frequency counter reading. A Tektronix FCA3100 frequency counter was used to measure our beat frequency, however similar reading errors on a different counter was observed in [124]. To determine the required criteria for correct frequency counting the counter capability was analysed as a function of the SNR and signal amplitude. The results of this analysis for a 689 nm beat note are shown in Fig. 4.10. In Fig. 4.10(a) the beat signal was kept constant at -3 dBm and the beat SNR was varied by changing the comb and 689 nm powers incident on the photodiode. The counter error appears at a SNR of 24 dB, where the maximum SNR is 29 dB. The lack of comb power at 689 nm limits the achievable SNR, where for the 638 nm a SNR of > 30 dB has been observed.

Fig. 4.10(b) shows the counter reading for different signal power levels. Here

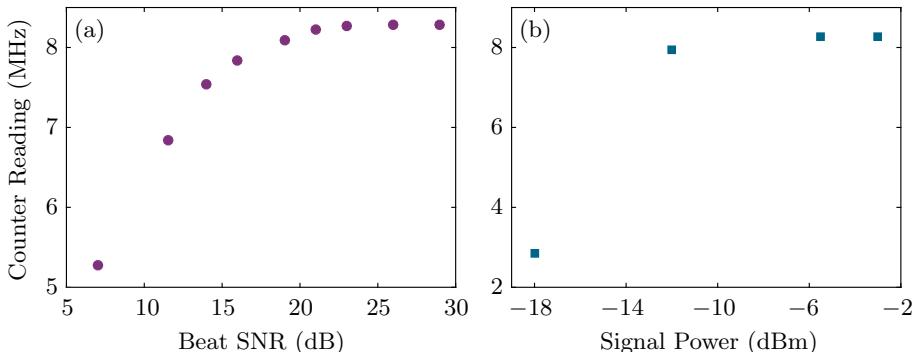

Figure 4.10: Counter frequency reading as (a) a function of beat signal-to-noise ratio (SNR) with signal power of −3 dBm and (b) a function of signal power with a SNR of 29 dB. The measured frequencies were obtained for a counter gate time of 1 s.

the SNR was kept constant at 29 dB, and the power level was varied using different combinations of amplifiers and RF attenuators. From Fig. 4.10(b) an error in the frequency reading appears below −5 dBm, where the lack of data points makes it hard to determine the exact signal level required. However for all measurements using the frequency counter the signal power is maintained at a level > -5 dBm, with a SNR > 25 dB. Similar measurements carried out with the 638 nm beat produced comparable results as in Fig. 4.10.

4.3 Long-term frequency Stability

4.3.1 Allan Deviation

For characterizing the long-term frequency instability of the 638 nm and 689 nm systems, we calculate the Allan deviation from heterodyne beat measurements with the frequency comb. The Allan variance [125], $\sigma_y^2(\tau)$, has been widely adopted for quantifying the phase and frequency instability of precision oscillators. The advantage of this variance is that it converges for most of the commonly encountered types of noise, whereas this is not the case for traditional statistical tools such as the standard deviation. A calculation of the Allan variance relies on measuring the difference between

successive readings of the fractional frequency, y, defined as:

$$y = \frac{f_b - \overline{f}_b}{f_0}, \tag{4.12}$$

where $\overline{f}_b$ is the mean beat frequency and f_0 is the laser frequency. The Allan variance then depends on the sampling period, τ, for the frequency measurements where

$$\sigma_y^2(\tau) = \frac{1}{2(M-1)} \sum_{i=1}^{M-1} [y_{i+1} - y_i]^2. \tag{4.13}$$

The conventional format for displaying the results of such a measurement is a log-log plot of the Allan deviation, given as $\sqrt{\sigma_y^2(\tau)}$ as a function of τ, where different noise types can be identified from the slope in particular time regions. The slope scales as τ^{-1} for white and flicker phase noise, $\tau^{-0.5}$ for white frequency noise, τ^0 for flicker frequency noise and $\tau^{0.5}$ for random walk. A modified Allan variance can be used for cases where distinguishing between white phase noise and flicker noise is a necessity. There are other options for measuring the stability of a device, and a list of the alternative types of variances are highlighted in [126]. The type of variance used in a particular case depends on the dominant noise processes, however the Allan variance has the advantage of being convergent for most types of clock noise, and therefore is usually the first choice in handling frequency instability. In general the stability of the device will improve as the averaging period increases, as some noise types are removed by averaging. At some point (known as the noise floor) averaging will no longer improve the results. The increase beyond this point is usually due to noise caused by environmental factors known as random walk noise.

In calculating the Allan deviation, both overlapping and non-overlapping binning schemes are typical, but overlapping bins are much more utilized in the clock community [126]. This is typically referred to as the overlapping

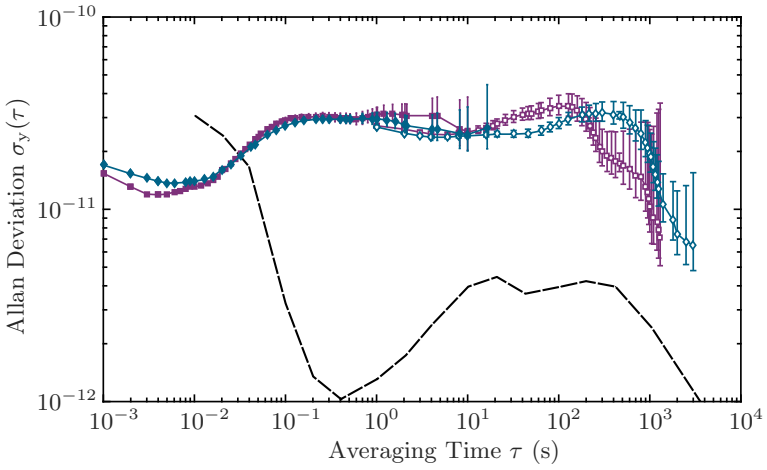

Figure 4.11: Allan deviation plots of the 638 nm (purple squares) and 689 nm (blue diamonds) lasers measured by beat notes with the optical frequency comb. Measurements were made with either a 1 ms or 1 s frequency counter gate time, as indicated by filled and empty symbols respectively. The black line shows the specified instability of the GPSDO from Jackson Labs [123].

Allan deviation, defined as:

$$\sigma_y^2(\tau) = \frac{1}{2m^2(M-2m+1)} \sum_{j=1}^{M-2m+1} \left\{ \sum_{i=j}^{j+m-1} [y_{i+m} - y_i] \right\}^2, \qquad (4.14)$$

where m is the averaging factor. This improves the confidence of the measurement, and in general the basic measurement interval is as short as practical to support larger number of overlaps at longer averaging times.

As mentioned in the previous section, a Tektronix FCA3100 frequency counter is used to monitor the beat note between our laser and the Toptica frequency comb. This counter has zero dead time, which is important for frequency stability measurements. Some counters have a delay between the stop of one measurement and the start of another due to processing time, during which the frequency is not monitored. The effects of this dead time can be removed using Bias functions [127], however these functions depend critically on the power noise law. As a result you need a relatively good understanding of the noise in a device when using them, and they are not particularly useful when multiple noise types are present.

The calculated overlapping Allan Deviation measurements for both the

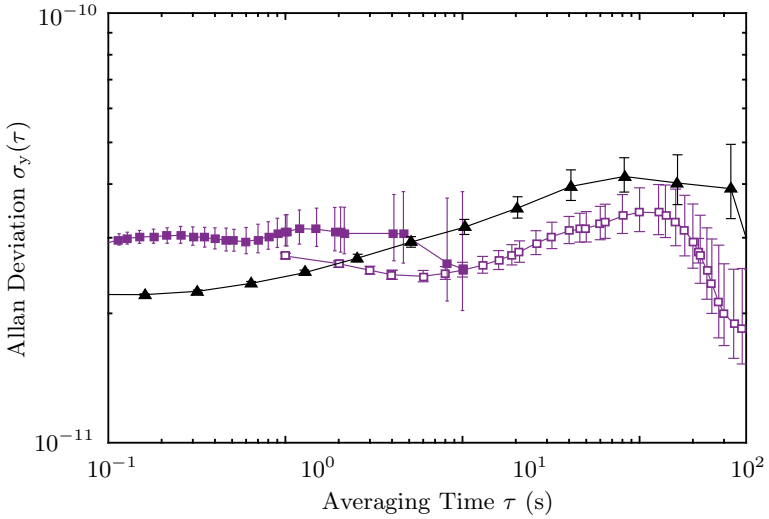

Figure 4.12: Allan deviation plots of the 638 nm laser for our homebuilt cavity (purple) as shown in Fig. 4.11, and for the new ULE cavity (black) with a 10 ms gate time.

689 nm and 638 nm beat notes are shown in Fig. 4.11, for counter gate times (or sampling periods) of both 1 ms and 1 s. The manufacturer's data for the GPS-disciplined quartz oscillator (GPSDO) reference used to stabilize the comb is plotted for comparison purposes, accessible from [123].

Both lasers have a comparable Allan deviation, starting to average down at around 1000 s. Longer measurements were difficult to obtain, with the main limitation depending on how long the lasers remain locked to the cavity. For $\tau < 0.1$ s, the beat frequency has less noise than the GPSDO, reflecting the lower noise of the oven-controlled crystal oscillator (OXCO). Above $\tau \sim 0.1$ s the ADEV should follow that of the GPSDO, assuming that the frequency comb and lasers are more stable than the GPS reference. Instead, the measurements reveal excess frequency noise. In [58] this noise was attributed to the performance of the transfer cavity length servo to the atomic reference. The cavity length was stabilised using a piezo, where we observed consistent problems with this piezo drifting. As this drift should typically correspond to a timescale of $\sim 1 \rightarrow 100$ s, we believed this to be the cause of the differences between the GPSDO and our measurements in Fig. 4.11.

However recent measurements with the new ULE cavity suggests that cav-

ity drift was not the cause of excess noise. This cavity is more stable (see next section), however a similar plateau is observed in the ADEV, shown in Fig. 4.12. Additionally, measurements with a 1550 nm laser locked to a different ULE cavity produces the same ADEV as for our lasers. This suggests another noise source is limiting the ADEV rather than laser noise. Before discussing possible sources of this noise, it is important to note that for the Fig. 4.11 the fractional frequency instability of both lasers systems is $< 4 \times 10^{-11}$ for all measurement times between 10^{-3} s and 10^{3} s. This corresponds to frequency deviations of just ~ 35 kHz for the UV laser and ~ 15 kHz for the 689 nm laser. This measured frequency instability is sufficiently small for performing high resolution spectroscopy of Rydberg states, where it is expected that our lasers should actually have a higher long-term stability than these measurements suggest.

The plateau of the ADEV can be attributed to a few things which are currently undergoing investigation. These are as follows: (1) fibre noise (2) the GPS reference and (3) the frequency comb lock.

As the comb is located in another laboratory the light from both our lasers first go through a ~ 70 m fibre before measuring the beat note. Fibre noise can result from any mechanical perturbations or temperature changes that lead to optical path length fluctuations shifting the optical frequency. This noise can be monitored by frequency shifting the light using an AOM before traveling through the long fibre. After traveling through the fibre the light will be frequency shifted by both the AOM and any Doppler effect in the fibre. This light is then reflected back down the fibre and overlapped with the original light, where the beat signal is detected on a photodiode. By taking an ADEV of this beat signal between the initial and reflected light it should be possible to determine if fibre noise is indeed the issue. The fluctuations could be compensated for by taking the detected beat signal just described and feeding it into a phase locked loop which regulates the frequency applied to the AOM. This scheme for active fibre noise compensation is regularly used [128–131].

The second possibility for the increased noise is that the RF reference is

not performing to the standard shown in Fig. 4.11. A test to determine if this is the case is more difficult, requiring a more stable 10 MHz reference. However the GPSDO reference is currently monitored during the ADEV measurements showing the number of satellites which are tracked, the crystal control voltage and the phase offset error of the internal crystal oscillator to the GPS reference. From monitoring these values the GPS seems to be operating to similar specifications as in [123].

Finally the issue could instead lie with the frequency comb and the locking parameters for f_{rep}. This would require a optimisation of the system in the future. Following more tests we should be able to determine the source of the excess noise. This will be carried out in the next few months, where in all cases there are clear solutions for increasing the stability.

4.3.2 Cavity Upgrade

The new ULE cavity has a higher finesse as confirmed through the ring-down measurement earlier in this section. This results in a narrower cavity resonance width which should lead to a narrower locked laser linewidth. The improved performance of the laser system can be inferred using the cold atoms, as the vertical position z of the narrowline MOT depends on the 689 nm MOT detuning δ. Fluctuations in the MOT position are observable for changes in δ of a few kHz. By running an experimental sequence to produce a narrowline MOT the shot-to-shot fluctuations in position can be observed which are shown in Fig. 4.13. Here $\delta = -100\,\mathrm{kHz}$, where the shift in vertical position is found by taking the average vertical position $\bar{z}$ over all the data points and plotting $\bar{z} - z$ for each experimental run. Comparing the change in vertical position for each cavity, the fluctuations are reduced by over an order of magnitude to $< 2\,\mu\mathrm{m}$ for the ULE cavity.

This highlights the higher frequency stability of the new cavity, leading to a more stable experiment that will be useful for future measurements. For example for the Rydberg dressing experiments of chapter 6, the improved position stability should allow any interaction effects to be more easily ap-

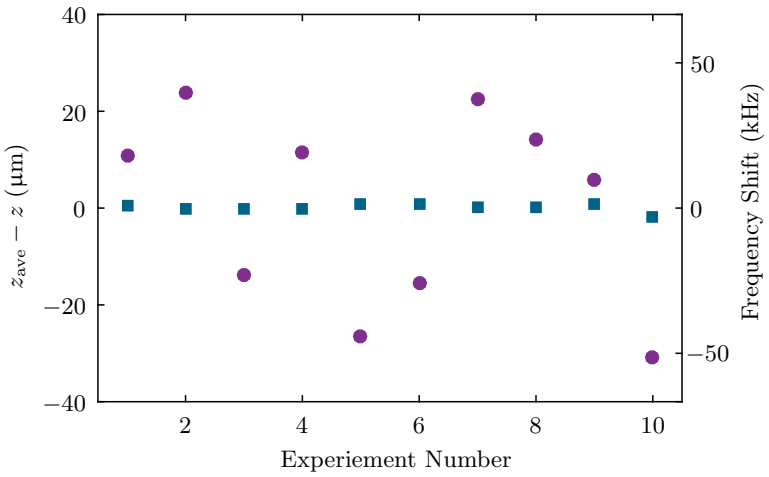

Figure 4.13: Vertical position shift $z_{\text{ave}} - z$ of the narrowline MOT for both the old cavity (purple circles) and new ULE cavity (blue squares). For each data point a new MOT is loaded. Also shown is the corresponding frequency shift, where the magnetic field gradient was $8\,\text{Gcm}^{-1}$.

parent.

Chapter 5

Rydberg Spectroscopy

The knowledge of Rydberg state properties is an interplay between experimental measurements and theory. By using experimentally determined quantum defects, quantum defect theory (QDT) can be used to calculate the properties of Rydberg atoms. This includes Rydberg state wave functions, transition dipole moments, eigenstates in external fields, lifetimes and dipole-dipole interactions energies. Here the knowledge of interactions properties is essential for many-body physics prospects. While single channel QDT is sufficient for describing alkali-metal atoms, for divalent atoms multichannel QDT is needed to take into account interactions between electrons [73].

Quantum defects are obtained by fitting experimentally measured Rydberg level energies with the Rydberg Ritz formula. For strontium, the best experimental measurements of the quantum defects have large associated uncertainties. In this work, improved Rydberg-Ritz formula coefficients (quantum defects) are calculated, giving the level energies for the $^3S_1$,$^3P_0$,$^3P_1$,$^3P_2$ and $^3D_1$ Rydberg series. The application of a small electric field during our experiments means that we can excite to the otherwise forbidden ^3P_J states. The field mixes a small amount of s- and d-states into the p-state, allowing for excitation from the 5s5p $^3P_1$ intermediate state. This chapter is divided into three main sections: the first section involves how we initially find the Rydberg states, the second shows the relevant ex-

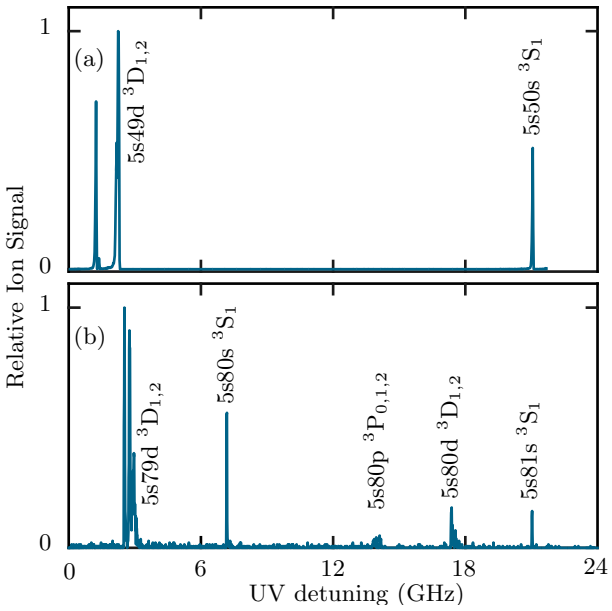

Figure 5.1: Measured ion signals while continuously scanning the UV laser at (a) $n \approx 50$ and (b) $n \approx 80$. A small electric field was applied during these scans.

periments conducted for characterising the states, and finally the last section focuses on absolute frequency measurements.

5.1 Finding Rydberg States

5.1.1 Initial Detection

Initial detection of the Rydberg states was carried out in a broadband MOT, while applying the UV laser for a duration of 2 s. The UV was unlocked from the reference cavity, and scanned via piezo tuning of the 1550 nm ECDL cavity length. At a transition frequency, the atoms are resonantly excited from the 5s5p $^3P_1$ state to a Rydberg state. During the experiments, a small electric field of $\sim$1 V/cm was applied to allow for excitation to the ^3P_J Rydberg states. The Rydberg atoms which spontaneously ionize were counted on the MCP. Additionally for a high enough UV intensity significant depletion of the MOT is evident.

UV scans carried out at both $n \sim 50$ and $n \sim 80$ are shown in Fig. 5.1.

When on resonance, we see high ion detection rates on the MCP. However the variation in signal height across the scan is largely due to depletion of atoms from the MOT, and is is not an indication of the transition strength. The Rydberg states were identified using the Rydberg-Ritz parameters in [53] to extrapolate from previous measurements at lower principal quantum numbers [46–48]. In Fig. 5.1(b), it is apparent that the applied electric field excitation results in excitation to the ^3P_J states, and additionally leads to to both a broadening and Stark splitting of the Rydberg states.

The absolute frequency accuracy of this technique is poor compared to other methods as the frequency of the laser can drift during the scan. Furthermore the wavemeter used to calibrate the scan has a relative accuracy of 40 MHz and an absolute accuracy of 3 GHz. Nevertheless it is a ideal method for initially finding the states as it is quick and allows the detection of multiple states at once. Furthermore, the scans in Fig. 5.1 highlight the large single-mode tuning range of the Rydberg excitation laser. The scanning range was limited by the mode-hop free range of the 1550 nm ECDL, which was $\sim$ 25 GHz.

5.1.2 Spectroscopy Methods

Before characterising the states, the Rydberg transitions were measured to a better accuracy than in Fig. 5.1. For this the laser was first locked to the high finesse cavity, and a spectrum was obtained by step-scanning over the transition in frequency steps of 250 kHz. The 408 nm autoionising laser was pulsed on with the UV for 10 ms to increase the ion detection level. First results were taken in the broadband MOT at the 5s49d $^3D_1$ state as shown in Fig. 5.2.

There are two methods for finding the Rydberg transitions, as following the experimental sequence we measure both the ion signal along with the atom number (using absorption imaging). The ion signal is the principal method we use for determining frequencies of the Rydberg transitions as it is much more sensitive than atom number. Results from scans without and with the

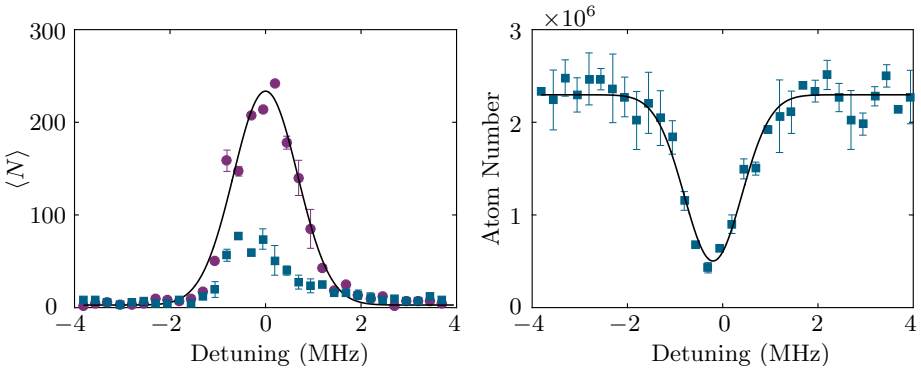

Figure 5.2: Measured ion signals (a) and atom number (b) as a function of UV frequency with (purple circles) and without (blue squares) the autoionisation laser. The solid lines show Gaussian fits to the data.

autoionising laser are shown in Fig. 5.2(a), where for the latter much higher signals are observed. Here the UV beam has a $1/e^2$ radius of 1 mm with a power of 5 mW, and pulse lengths of 10 ms were used. Significant depletion in atom number is measured for large enough UV powers as in Fig. 5.2(b), where the UV power was increased to 80 mW. The Gaussian fits for each detection method give widths of < 1 MHz.

5.1.3 Precision Spectroscopy

High precision measurements of the Rydberg states require first obtaining a narrow spectrum to find the centre of the transition. In this thesis, spectroscopy measurements are carried out in a broadband MOT, where the longer lifetime allows multiple excitations in a single MOT. As a result, it significantly increases the speed at which data can be attained.

The experimental sequence used for high precision spectroscopy is presented in Fig. 5.3. For obtaining the spectrum, atoms are released from a broadband MOT, before excitation to the Rydberg state. To distinguish between the magnetic sublevels a vertical quantisation field of 3.1 G was applied during the excitation sequence. The 689 nm laser is applied first, addressing the $m_J = -1$ state, and following a 2 µs delay we pulse on the 319 nm Rydberg excitation laser. Here we applied vertically polarised coupling light so that

only the $m_J = -1$ state was driven. The purpose of using a one-photon excitation sequence is to eliminate possible two-photon effects. The power in each of the excitation beams is typically $< 100\,\mu W$. The duration of each pulse is the same, and typically a $5\,\mu s$ pulse length is used. After Rydberg excitation, an autioionisation pulse is applied for $5\,\mu s$, directly followed by an electric field to direct ions towards the MCP. In order to map out the spectrum, the 689 nm laser is set on resonance, while the UV laser is stepped to a new detuning value on each iteration of the experiment.

The resulting spectrum for the 5s37s $^3S_1$ state is shown in Fig. 5.4. The lineshape is described by a Gaussian profile, where the fitted FWHM is $420 \pm 10\,kHz$. From the least squared fit, the centre of the transition is determined with a statistical uncertainty of $4\,kHz$.

To obtain an absolute frequency of the Rydberg state, the Zeeman splitting between the $m_J = 0$ and $m_J = -1$ states must first be determined. For this measurement, the coupling beam was changed to a combination of vertically and horizontally polarised light. This allows coupling to the different m_J states as shown in Fig. 5.5(a). The experiment used to obtain the spectrum for Fig. 5.4 was then repeated. The results are shown in Fig. 5.5(b), where both the $m_J = 0$ and $m_J = -1$ states are observed. By fitting to the two peaks, a frequency shift $6.568 \pm 0.008\,MHz$ was obtained.

After obtaining a narrow Rydberg spectrum, the next step is to determine the absolute frequency of the transition. This requires measuring the beat note between the frequency comb and each of the excitation lasers. The

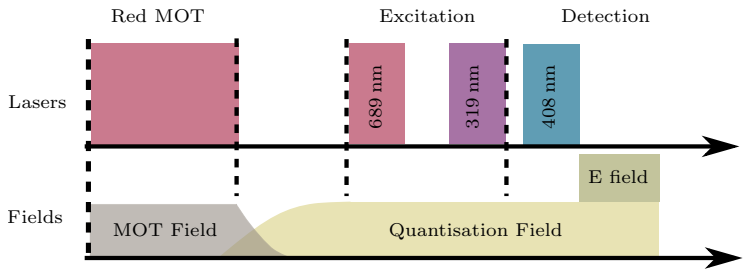

Figure 5.3: Experimental sequence used for high precision spectroscopy. The timing for each stage i.e. cooling, excitation and detection, is described in the text.

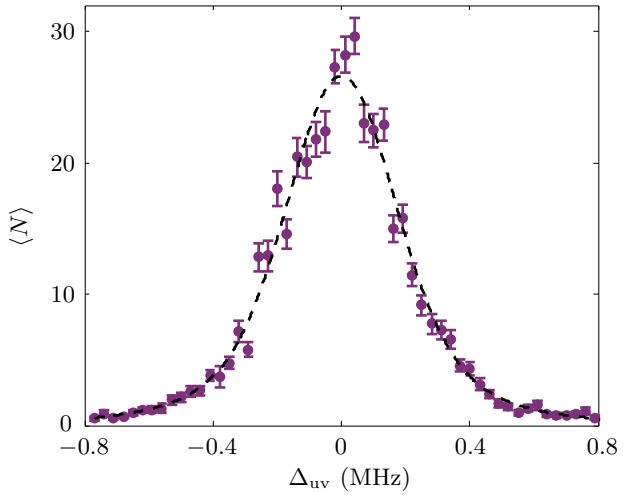

Figure 5.4: Ion signal as a function of UV detuning for an on-resonance 689 nm ($m_j = -1$) probe laser. The data was taken after releasing the atoms from a narrow-line MOT, and a vertical quantisation field of 3.1 G was applied during the excitation sequence. Here the dashed line shows a Gaussian fit to the data.

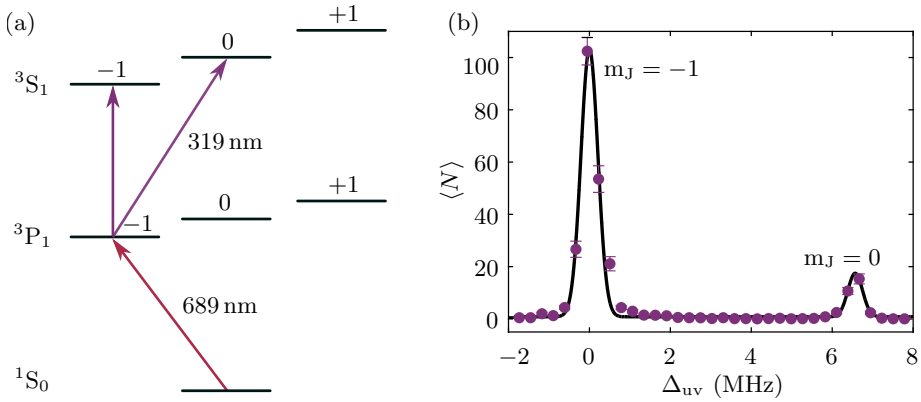

Figure 5.5: (a) By applying a quantisation field during Rydberg excitation, the different magnetic sublevels can be distinguished. By selecting the polarisation of the 319 nm light we can select a single m_J sublevel. When the coupling light is a combination of vertical and horizonal polsarisation, both the $m_J = 0$ and $m_J = -1$ can be driven as shown here. (b) Measured Zeeman splitting between the $m_J = 0$ and $m_J = -1$ states. By fitting a Gaussian to each peak a separation of 6.568 ± 0.008 MHz is determined.

method for attaining a beat note with the comb is outlined in chapter 4. Note that the beat note for the Rydberg excitation laser is taken at 638 nm (before doubling to the UV). Both excitation lasers were locked on-resonance before taking the beat measurement, and beat frequencies of 36.042 ± 0.001 MHz and 8.642 ± 0.001 MHz at 638 nm and 689 nm respectively.

In order to obtain the absolute frequency from this method, the light used for the beat notes at 689 nm and 638 nm is measured on a calibrated wavemeter. For the DFG comb (see chapter 4), the comb line used in the beat measurement, n, is then determined from the equation:

$$f_l = n f_{rep} \pm f_b \tag{5.1}$$

where f_l is the measured frequency on the wavemeter, f_b is the measured beat note and f_{rep} is the known repetition rate of the comb (80 MHz). Once n is known the same equation is then used to find f_l for both lasers to a higher level of precision. The transition frequency is then determined from the values obtained. While error in the line centre of the Rydberg spectrum is just $\sim$10 kHz, systematic frequency shifts effect the line position, leading to larger overall uncertainties. The expected magnitude of these uncertainties are discussed later, along with the results of absolute frequency measurements at a range of Rydberg states.

5.2 Rydberg State Characterisation

Following the initial detection of a Rydberg state, we can experimentally measure other Rydberg state properties. In particular, we determine the Rabi frequency, DC stark shift, state lifetime and autoionisation spectra. These properties are relevant for both the Rydberg spectroscopy and Rydberg dressing experiments detailed in this work.

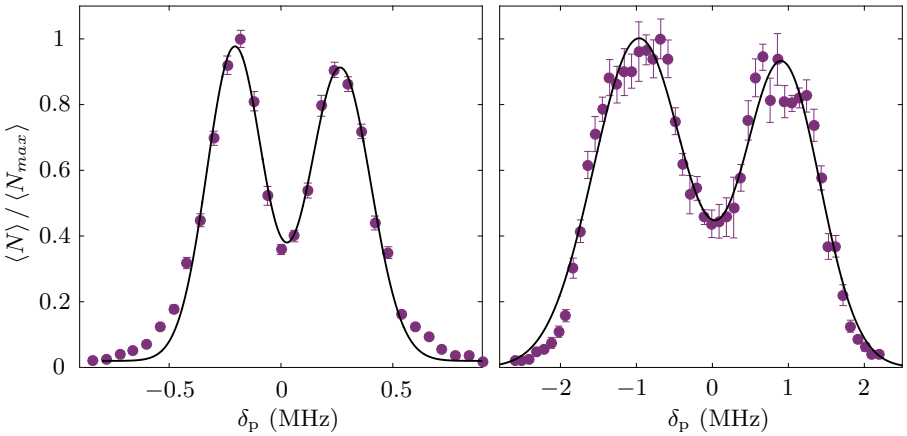

Figure 5.6: Ion signal as a function of probe beam detuning for a high intensity coupling beam with a $1/e^2$ radius of (a)0.93 mm (0.79 mm) and (b) 160 µm (120 µm) in the vertical (horizontal) direction. Solid lines are double Gaussian fits, where the splitting between the peaks is a direct measurement of the coupling beam Rabi frequency.

5.2.1 Autler-Townes Splitting

A measurement of the Autler-Townes splitting provides a direct measurement of the Rabi frequency of the UV beam. For the precision spectroscopy discussed in the next section, the achievable Rabi frequency is not important as typically very low coupling power is used. The reason for this is to eliminate power broadening so as to achieve as narrow a spectrum as possible. However, in chapter 6, a high Rabi frequency (Ω_d) on the Rydberg transition is a critical requirement for observing Rydberg dressing. Here we describe our technique for measuring Ω_d.

To measure the Rabi frequency, two-photon excitation is performed as before (see Fig. 5.3). However, here the coupling beam is set on resonance, while the 689 nm probe beam frequency is varied. As the coupling laser intensity is increased the spectrum splits into two peaks as shown in Fig. 5.6. This effect is known as Autler-Townes splitting and is caused by the AC Stark effect of the 689 nm transition in the presence of a strong coupling beam [132]. The separation between the peaks gives the value for the Rabi frequency at that intensity.

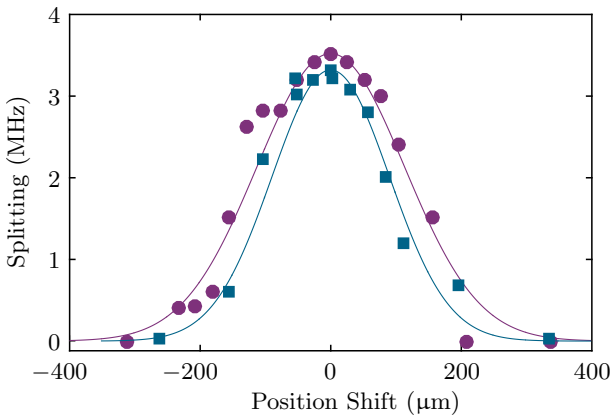

Figure 5.7: Autler-Townes splitting as a function of the MOT position in the vertical (purple circles) and horizontal (blue squares) directions. The solid lines are Gaussian fits to each data set.

For the results in Fig. 5.6 the excitation pulse was short, on the order of 10 μs, and the probe power is set as low as necessary so that the detector is not saturated. The results in Fig. 5.6 (a) and (b) were taken with the same UV power (70 mW), where the intensity was changed by focusing the UV beam. For (a) the $1/e^2$ radius was 0.93 mm (0.79 mm) in the vertical (horizontal) direction, while in (b) this was reduced to a $1/e^2$ radius of 160 μm (120 μm). The fits to the data give a Rabi frequency of 0.47 ± 0.01 MHz and 1.88 ± 0.03 MHz respectively.

Measuring the Autler-Townes splitting also proved to be a useful alignment tool for a small coupling beam size. Fig. 5.7 shows the Aulter-Townes splitting as a function of the cloud position. The MOT position is moved by changing the current in the external compensation coils. A better alignment of the coupling beam on the MOT leads to more pronounced splitting and a higher Rabi-frequency. From the fits in Fig. 5.7 the $1/e^2$ radii of the coupling beam can be obtained. A beam size of 160 μm in the vertical direction and 120 μm in the horizontal direction is obtained from the fit.

DC Stark Sensitivity

The high polarizability of Rydberg atoms ($\propto n^7$) means that the application of static electric fields results in transition shifts as well as state mixing, while for sufficiently large fields ioinisation occurs. Stark maps are a useful tool for the experimental results shown in this thesis. In particular, they can be used to determine the magnitude of any stray field in our experiment. This is useful when evaluating systematic uncertainties of measured Rydberg energy levels. Additionally, in chapter 6 the Rydberg dressed MOT is found to be extremely sensitive to electric fields, as a result of admixed Rydberg character. A complete understanding of the effects of electric fields on the dressed MOT require a knowledge of the static polarisibility of the bare Rydberg states.

At low electric fields, E, the DC Stark shift of the Rydberg state Δ_{DC} is described by:

$$\Delta_{\mathrm{DC}} = \frac{1}{2}\alpha E^2 \tag{5.2}$$

where α is the static polarisability. The Rydberg line shifts are commonly displayed in Stark maps, showing how the energy changes with applied field. Our experimental protocol used to obtain a Stark map is as follows: atoms are released from the MOT and data is taken using one-photon excitation. First an on-resonance 689 nm beam is pulsed on, and following $\sim$2 µs delay the Rydberg coupling laser is applied. During the excitation a uniform electric field is applied and at different field values a spectrum was taken by scanning the UV laser across resonance. The line centre is determined by fitting a Gaussian to the observed spectra and the energy shift is then mapped out for different field strengths.

An experimentally measured Stark map is shown in Fig. 5.8 for the 5s37p $^3\mathrm{P}_0$ Rydberg state. Here the fit to the data is given by a slight modification to equation 5.2, to include the effects of stray electric fields. By decomposing $\vec{E}$ into its perpendicular $E_\perp$ and parallel $E_\parallel$ components

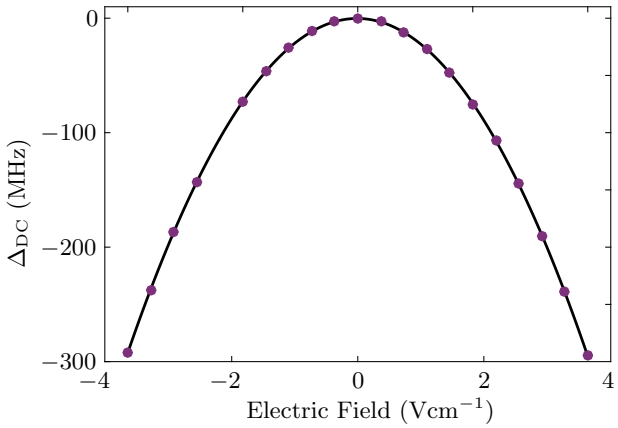

Figure 5.8: DC stark shift of the 5s5p $^3P_0$ Rydberg state as a function of the applied voltage on the electrodes. From the fit to the data (black line) the stray field can be estimated as described in the text.

($E^2 = E_\perp^2 + E_\parallel^2$), from equation 5.2 we find:

$$\Delta_{DC} = \frac{1}{2}\alpha(E_{\perp,\text{stray}}^2 + (E_{\parallel,\text{stray}} - \beta V)^2) \tag{5.3}$$

where β relates the voltage applied to the electrode pair V to the electric field created in Vcm^{-1}. In our experiment we obtain a value of 0.36 Vcm^{-1} for β [91]. In Fig. 5.8, equation 5.3 gives the solid line fit to the data, with fit parameters α, $E_{\perp,\text{stray}}$ and $E_{\parallel,\text{stray}}$. From the fit we can determine both the static polarisability of the Rydberg state, and the magnitude of the stray field.

5.2.2 Rydberg Lifetimes

Lifetime measurements of the Rydberg state are important for the dressing experiment in chapter 6. As the dressed MOT lifetime is dependant on the Rydberg lifetime, knowledge of decay rate allows a better understanding of our loss mechanisms.

To measure the lifetime of a Rydberg state the delay time, Δt, between Rydberg creation and autoionisation of the Rydberg atoms is varied, then any surviving Rydberg atoms for each Δt are detected. The sequence is again

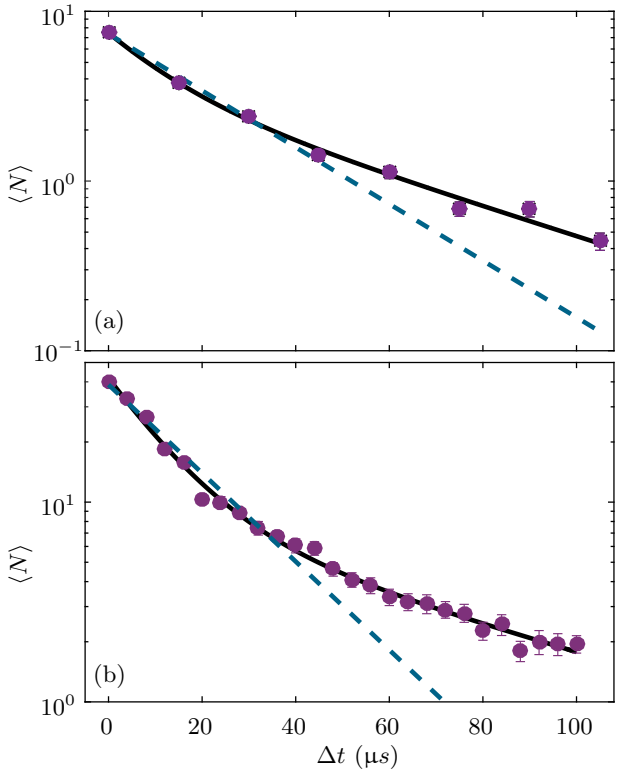

Figure 5.9: Measured ion signal as a function of the delay time, Δt, between excitation and autoionisation of the Rydberg atoms for the (a) 5s37s $^3S_1$ and (b) 5s36d $^3D_1$ Rydberg states. The y-axis is shown on a logarithmic scale, where the dashed (blue) line is a single exponential fit and the solid (black) line is a double exponential fit.

similar for the previous experiments outlined in this chapter. A broadband MOT is first formed, following which the MOT light and magnetic field are turned off before excitation. We use excitation pulses that are short compared to the Rydberg state lifetime to limit transfer to other states during excitation.

A lifetime measurement of the 5s37s $^3S_1$ state is shown in Fig. 5.9(a). A single exponential yields a poor fit to the data, where a double exponential fit provides far better agreement. This is attributed to Rydberg atoms decaying into other, longer-lived Rydberg states. Future analysis of the autoionization spectrum can be used to identify and quantitatively measure population transfer, as shown in [82] for the singlet Rydberg states. The fit in Fig. 5.9(a) gives lifetimes of $14 \pm 3\,\mu s$ and $49 \pm 10\,\mu s$. A previously

reported value of $20 \pm 1\,\mu s$ was obtained for the 5s38s $^3S_1$ state [133]. This value was measured using state selective field ionization and agrees with the shorter lifetime in Fig. 5.9(a), as the Rydberg lifetime scales as n^3.
A lifetime of the 5s36d $^3D_1$ state is shown in Fig. 5.9(b). The data is again well described by a double exponential fit, yielding lifetimes of $12 \pm 1\,\mu s$ and $63 \pm 13\,\mu s$. Rydberg lifetimes taken at various Rydberg states measured throughout the work of this thesis are tabulated in table 5.1. Excitation to the listed ^3P_J states was possible by applying a weak electric field during the coupling pulse.

5.2.3 Autoionisation Spectrum

The detection of Rydberg atoms in this thesis uses the autoionising technique as discussed in chapter 3. A study of the autoionization spectra for the singlet Rydberg states is presented in [82], allowing the identification of population transfer to other states. For the triplet Rydberg states a detailed characterisation of autoionisation has yet to be performed.
In Fig. 5.10, autoionising spectra for two different Rydberg states are presented. As before, a small electric field is applied during Rydberg excitation in order to couple to the 5s37p $^3P_0$ Rydberg state. For these measurements the 689 nm probe beam was pulsed on with the Rydberg coupling beam for

Rydberg State	Lifetime (μs)
5s37s $^3S_1$	14 ± 3
5s50s $^3S_1$	48 ± 3
5s37p $^3P_0$	38 ± 1
5s37p $^3P_1$	34 ± 4
5s37p $^3P_2$	38 ± 6
5s36d $^3D_1$	11 ± 1
5s36d $^3D_2$	20 ± 2

Table 5.1: Lifetimes tabulated for various Rydberg states of interest in this thesis.

3 µs. After excitation the autoionising laser was applied for 5 µs, and subsequently an electric field was used to direct the ions to the MCP.

Results of the experiment for the 5s37s $^3S_1$ state are shown in Fig. 5.10(a). The rapid ionization of the doubly excited autoionizing states leads to broad features on the order of 10s of GHz. The fit to the spectrum uses multi-channel quantum defect theory (MQDT) [134], where details of the fitting equations and parameters are given in the appendix. The shape of the autoionizing resonance is caused by the difference in quantum defect between the 5snl state and the 5pnl state [95]. More detail on MQDT fitting (for the singlet Rydberg states) is presented in [82]. A simple two-channel MQDT model is used in Fig. 5.10, as the autoionizing series for the triplet Rydberg states has not been studied before, and the MQDT parameters are unknown. In [82, 135], only considering a single autoionizing channel and it's coupling to the continuum (a two-channel MQDT model) was found to be over simplistic for the strontium Rydberg series. Generally a total of six channels were required to reproduce the autoionization spectra of the states. While the fit in Fig. 5.10(a) does not account for the second peak seen at ~ -12 GHz, otherwise the data and model are in reasonable agreement.

Fig. 5.10(b) shows the autoionizing spectrum of the 5s37p $^3P_0$. Coupling to this state is achieved by applying a weak electric field during the excitation. Compared to the 5s37s $^3S_1$ data there are two clear peaks. The maximum autoinizing signal is also shifted in frequency by a few GHz. By increasing the difference in quantum defects between the 5snl state and the 5pnl state, two peaks are generated by a two-channel MQDT. However, the separation of the peaks from the model is $\sim$ 150 GHz, which is much larger than the observed splitting in Fig. 5.10(b). Therefore a two-channel MQDT does not account for the shape of the spectrum, where more channels would need to be added for a full description. This is a possible avenue for future work, requiring more data at different Rydberg series.

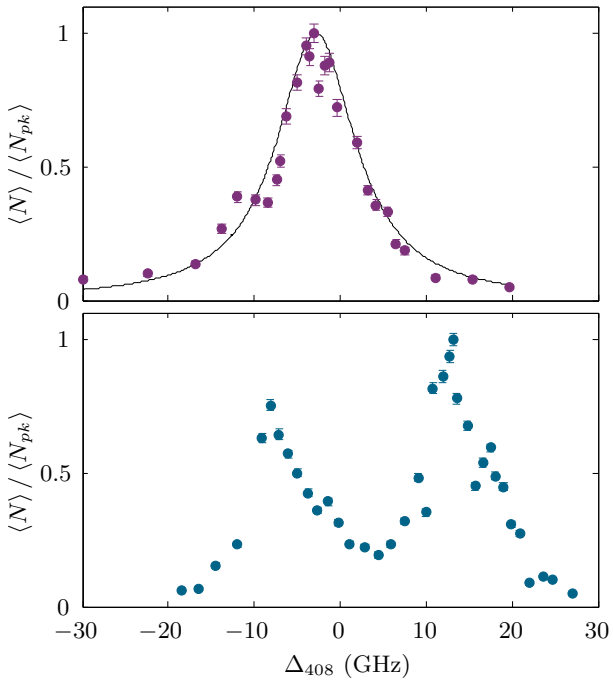

Figure 5.10: Ion signal as a function of the autoionising laser frequency for (a) the 5s37s $^3S_1$ state and (b) the 5s37p $^3P_0$ state. In (a) the solid line is a fit using a two-channel MQDT model. In both spectra the detuning is relative to the bare ion transition

5.3 Precision Frequency Measurements

The measured Rydberg energy levels acquired throughout this work are outlined in this section. First, both the statistical and systematic uncertainties for our current measurements are considered. We find that the current uncertainty of the absolute frequency measurements are dominated by systematic frequency shifts. However, the results already show a higher precision compared to previous measurements in strontium. Future methods to reduce the error from systematic shifts are outlined, where it should be possible to determine the absolute frequency of Rydberg states to $< 10\,\mathrm{kHz}$.

5.3.1 Systematic Uncertainties

In this experiment the systematic uncertainties include shifts in the resonance frequency due to external fields such as stray magnetic and electric

fields, and the blackbody radiation (BBR) from the environment. While highly excited Rydberg states are sensitive to BBR energy shifts, the magnitude of this is measured to be about 2.4 kHz at T =300 K [136]. Therefore this effect is not a dominant contribution to our uncertainties for the measurements outlined in this chapter.

Magnetic Fields

To compensate stray magnetic fields in our experiment three pairs of external coils, with orthogonal axes, are installed around the chamber. Two main methods are employed in order to measure any stray magnetic field. The first method uses the sensitivity of the 689 nm MOT to magnetic fields using the technique outlined in [84]. In the red MOT any weak, stray magnetic fields within the vacuum chamber shift the position of the zero of the quadrupole magnetic field gradients. By varying the current through the compensation coils the position r of the MOT formation (indicating the position of the magnetic field zero) is measured for three different quadrupole gradients ($\partial B/\partial r$). The result of such an experiment is illustrated in Fig. 5.11 for different $\partial B/\partial z$. The compensation current where the z positions cross each other determines where the external fields are compensated. Setting the current to this value the experiment is then repeated along another axis to find again find the required compensation field. Following compensation along all three axes, further cycles of optimisation are required until the values converge. Typically we take 2 to 3 iterative cycles using this method, and then use spectroscopic techniques to minimise the stray field further. Following this compensation technique, the stray field is minimised to $\sim$ 20 mG.

The second method for reducing the stray fields is a spectroscopic technique, highlighted in Fig. 5.12. Here the splitting between the 5s5p ^{3}P$_1$ m_J levels due to stray magnetic fields is measured by scanning the probe in small steps. Following creating a narrow-band MOT all fields, excluding the compensation fields, are switched off, and two-photon excitation to the

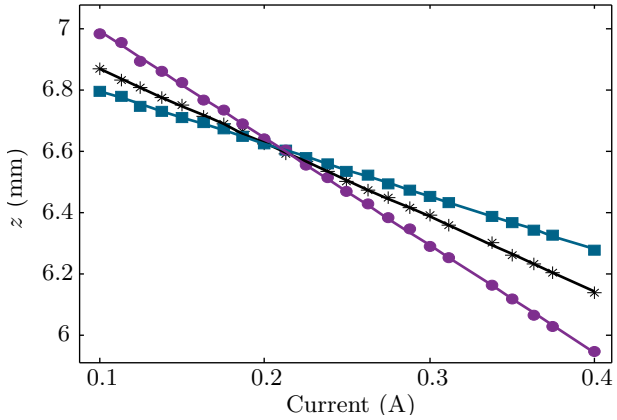

Figure 5.11: The MOT position z is changed by varying the current through a pair of compensation coils in the z direction. The three data sets are for different magnetic fields gradients: $\partial B/\partial z = 10\,\mathrm{Gcm}^{-1}$ (blue squares), $\partial B/\partial z = 8\,\mathrm{Gcm}^{-1}$ (black stars) and $\partial B/\partial z = 5\,\mathrm{Gcm}^{-1}$ (purple circles). Each data set is fitted with a linear fit, where the intersection determines the point of compensation for the stray field.

Rydberg state is performed, with the UV on resonance. For this experiment the MOT beams are used as the 689 nm probe, as a stray magnetic field splits the intermediate state where all magnetic sublevels are driven by the MOT beams. By mapping out the splitting as a function of the compensation coil current we find the minimum along each axis. Again this process is iterative and following optimisation for each compensation coil the procedure is repeated. In Fig. 5.12(a) a splitting of 400 kHz is observed before optimisation. Here a stray field was applied with the compensation coils to make the splitting more pronounced. However following an optimisation on each axis no splitting is observed for Fig. 5.12(b). Here the FWHM is 95 ± 3 kHz with probe frequency steps of 20 kHz.

Any background magnetic field can be reduced further by applying an external magnetic field orthogonal to the beam propagation direction. By driving to all the m_J levels as in Fig. 5.12 any background residual field can be constrained further using spectroscopy. Overall this method allows for stray fields to be reduced to the level of ~ 1 mG. Note that the method to reduce the effect of stray fields should be repeated on a regular basis, which was

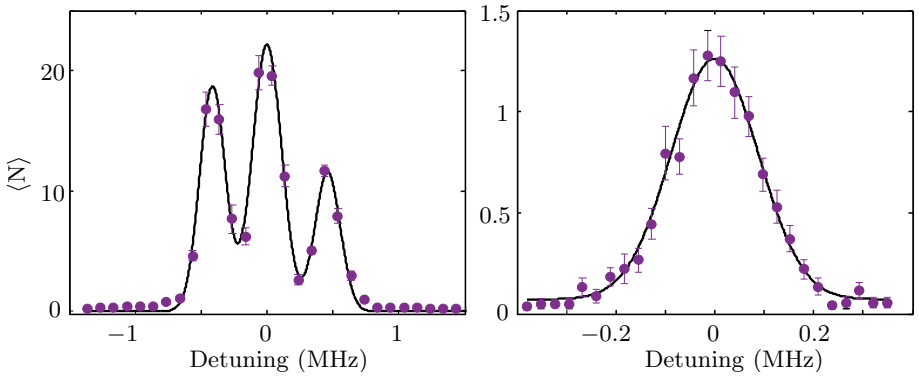

Figure 5.12: Two 689 nm probe scans are shown for different compensation currents along the x-axis. This methods allows for the stray field to be reduced further. In (a) a splitting of 400 kHz is observed from the $m_j = 0$ to $m_j = \pm 1$, where in (b) the splitting is no long visible. The FWHM in (b) is 95 ± 3 kHz.

not the case for the frequency measurements of this chapter. However the main systematic uncertainty of the frequency measurements taken to date was due to stray DC electric fields.

Stray DC Electric Fields

Before taking absolute frequency measurements, the stray DC fields should be compensated as they lead to systematic uncertainties in the measured frequency. The spectroscopy of this thesis was mainly exploratory in order to initially find Rydberg states, and determine which state to select for the undergoing Rydberg dressing experiments. Therefore a complete compensation for the stray DC fields was not carried out. Here the magnitude of the stray field was measured at each state by fitting to Stark maps, as shown in Fig 5.8.

The data for each Stark map was taken directly before measuring the Rydberg state frequency, therefore giving the magnitude of the stray field and resulting shift of the zero-field energy. The stray field is found to vary between different Rydberg state measurements, however this is not surprising as the data was taken months apart in some cases. The values calculated from fits to the stark map gave stray fields in the range of $0.1 \rightarrow 0.3\,\mathrm{Vcm}^{-1}$.

The smallest shift is for the 5s37p $^3S_1$ state, which is less sensitive to DC fields, giving a shift of $\sim 200\,\text{kHz}$. The other P and D states have resulting shifts of up to 2 MHz. Therefore, we find the stray electric fields are currently the dominant contribution to the uncertainty in our frequency measurements. These uncertainties are still lower than many previous measurements for the strontium Rydberg series. In the future compensating the stray field will allow us to obtain measurements with better accuracy, on the level of our statistical uncertainty.

Future Compensation of Stray DC Fields

To compensate stray fields a similar experiment to that in Fig. 5.8 is performed. By using the electrodes small field strengths can be applied, where our electrode configuration allows independent adjustment of the field in each spatial dimension. As states experience a quadratic Stark effect at low field strengths, the stray field can be measured and subsequently compensated for along each axis. This procedure should be carried out at high n values exploiting the n^7 scaling of the polarizability. Using this method it should be possible to reduce the stray field to $< 1\,\text{mVcm}^{-1}$ as achieved in [55, 137]. This reduces the stray field by $\sim$ two orders of magnitude from the stray fields measured in our Stark maps. Note that the procedure outlined should be repeated on a daily basis in order to maintain the stray field at this level. Following a thorough compensation of the stray DC fields, the uncertainties associated with absolute frequency measurements should be on the order of our statistical uncertainties. In particular, a line shift of $< 5\,\text{kHz}$ can be expected at Rydberg states for which $n < 100$.

5.3.2 Results

Here we give results of the Rydberg state energies measured to date on our experiment, and compare them to previous measurements. By fitting the new data, along with previous measurements to the Rydberg-Ritz formula (equation 2.6), an update of the Rydberg-Ritz coefficients from [73] are ob-

tained. To show the benefit of improved Rydberg spectroscopy, calculated Stark maps that rely on the Rydberg-Ritz coefficients are compared with experimental data.

The method for obtaining absolute frequencies was discussed earlier in section 5.1. Energy values for the triplet Sr Rydberg states using the procedure outlined are listed in table 5.2. Note that as for other cases throughout this chapter, the $3P_J$ Rydberg states are measured by applying a small DC field during the experimental sequence. The uncertainties associated with each measurement are given by the last digit in brackets, which includes the systematic errors due to stray fields. Where available the energy is compared with previously measured values. There is a lack of frequency measurements available for some Rydberg series, especially at high n (> 20) values. From the data in table 5.2 the states measured throughout this thesis already provide improved precision over the previous data. As this spectroscopy was mainly exploratory, in order to find required states for our experiments, the systematic uncertainties were not considered before the measurements. In the future better accuracy can be obtained by reducing the systematic uncertainties as outlined in the last section. In addition measurements of entire Rydberg series for $n > 35$ can be obtained, providing tighter constraints on fits to the quatum defect values. The experimentally obtained quantum defects are also tabulated in table 5.2.

Using the Rydberg-Ritz formula, the quantum defect coefficients for a Rydberg series can be obtained from the zero-field energies. The coefficients stated in [73] for the Rydberg series of interest in this thesis are listed in table 5.3. By using both our new measurements from table 5.2, along with the previous measurements taken at different n [46, 48, 73], and refitting to the Rydberg-Ritz formula (equation 2.6), updated coefficients can be calculated as shown in table 5.4.

The experimental quantum defect values and obtained fits (using equation 2.6) for the Rydberg series are shown in Fig. 5.13(a) for the 5sns $^3S_1$ Rydberg series, Fig. 5.13(b) for 5snd $^3D_1$, while Fig. 5.14 shows the 5snp $^3P_{0,1,2}$ series.

Rydberg State	$E_{previous}$ (cm^{-1})	E_{exp} (cm^{-1})	δ_{exp}	Reference ($E_{previous}$)
5s37s $^3S_1$	45835.15(15)	45835.162772(7)	3.369702(1)	[46]
5s37p $^3P_0$	none	45837.89106(2)	2.886669(4)	-
5s37p $^3P_1$	none	45837.91583(7)	2.88219(1)	-
5s37p $^3P_2$	45837.93(2)	45837.97319(7)	2.87180(1)	[48]
5s36d $^3D_1$	none	45833.48631(1)	2.656527(2)	-

Table 5.2: Our measured energies E_{exp} of triplet Rydberg states in Sr compared to previously values ($E_{previous}$). Also shown are the corresponding quantum defect values δ_{exp}. Uncertainties are given by the last digits given in brackets and references are provided in the last column where appropriate.

Series	δ_0	δ_2	δ_4
5sns $^3S_1$	3.371(3)	0.5(2)	$-1(2) \times 10^1$
5snp $^3P_0$	2.8866(1)	0.44(1)	-1.9(1)
5snp $^3P_1$	2.8824(2)	0.407(5)	-1.3(1)
5snp $^3P_2$	2.8719(2)	0.446(5)	-1.9(1)
5snd $^3D_1$	2.658(6)	3(2)	$-8.8(7) \times 10^3$

Table 5.3: Rydberg-Ritz coefficients for selected Rydberg series taken from [73].

Series	δ_0	δ_2	δ_4
5sns $^3S_1$	3.36924(2)	0.52(2)	-0.1(3)
5snp $^3P_0$	2.88627(1)	0.469(6)	-2.4(2)
5snp $^3P_1$	2.88180(2)	0.468(6)	-2.5(2)
5snp $^3P_2$	2.87139(1)	0.494(6)	-2.8(2)
5snd $^3D_1$	2.664(7)	-1(9)	$-8(2) \times 10^3$

Table 5.4: Newly calculated Rydberg-Ritz coefficients using the results from table 5.2, along with those for previous measurements of the Rydberg series [46, 48, 73], i.e. the measurements used in producing table 5.3.

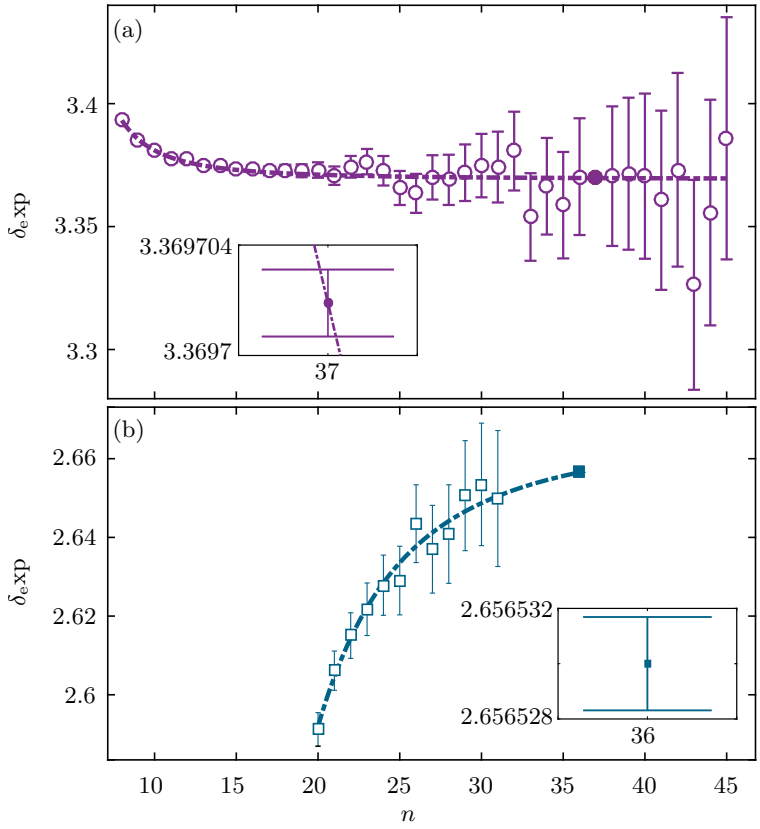

Figure 5.13: Quantum defects, δ_{exp}, for (a) 5sns $^3S_1$ (purple circles) and (b) 5snd $^3D_1$ (blue squares) Rydberg series. The hollow markers are previously measured values from other groups [46] while the filled markers show the results from our measurements. The solid lines are fits to the data using the Rydberg-Ritz formula. Insets show our data points, highlighting the size of the error bar.

In each graph our measurement is highlighted (filled marker) from previous data sets (unfilled markers). In Fig. 5.13 our measured points have a lower uncertainty than previous measurements, as is clear from the insets. While measurements up to $n = 45$ have been obtained for the 5sns $^3S_1$ Rydberg series, there is much less data at other Rydberg states. This is particularly clear for $^3P_{0,1,2}$ in Fig. 5.14 where our measured values at $n = 37$ are the last data point in the graph.

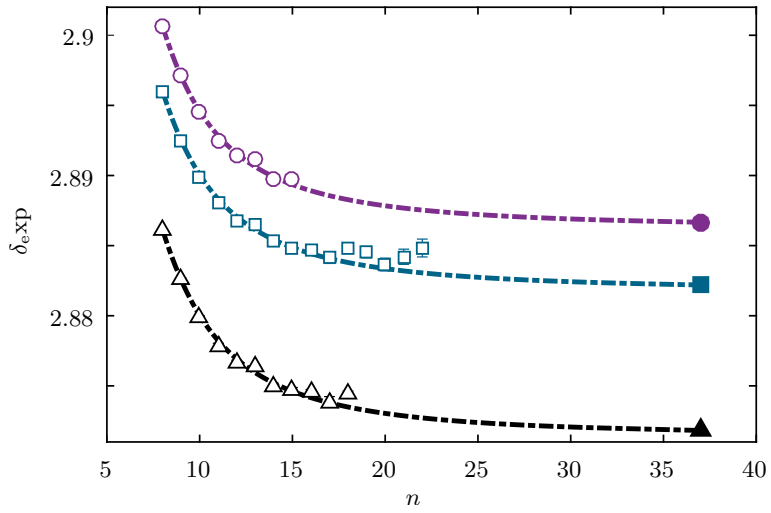

Figure 5.14: Quantum defects, δ_{exp}, for the 5snp $^3P_0$ (purple circles), $^3P_1$ (blue squares) and $^3P_2$ (black triangles) Rydberg series. The hollow markers are previously measured values from other groups [48] while the filled markers show the results from our measurements. The solid lines are fits to the data using the Rydberg-Ritz formula.

Calculated Stark Maps

As shown in Fig. 5.8, the large polarisabiliy of Rydberg states can be displayed in Stark maps, showing the energy level shift with applied electric field. The Stark maps can be calculated to a high degree of accuracy [138], while previous work in strontium has produced Stark maps that are in agreement with experimental measurements [55, 139].

The approach for calculating the Stark maps shown in this work was developed by P. Huillery [55] and relies on fitting experimentally measured zero-field energies to calculate the wavefunctions. Therefore as the calculations rely on the values for the fitted quantum defects in table 5.4, this provides a method to determine the accuracy of the current measurements.

In Fig. 5.15, experimental results are compared to the calculated Stark maps for various Rydberg states. For comparing the model to the experimental data, the only fit parameter is the electric field calibration factor. For all the data sets in Fig. 5.15, this is set as $0.36\,\mathrm{Vcm}^{-1}$. For each state, the experimental data and the model are shown to agree within the uncertain-

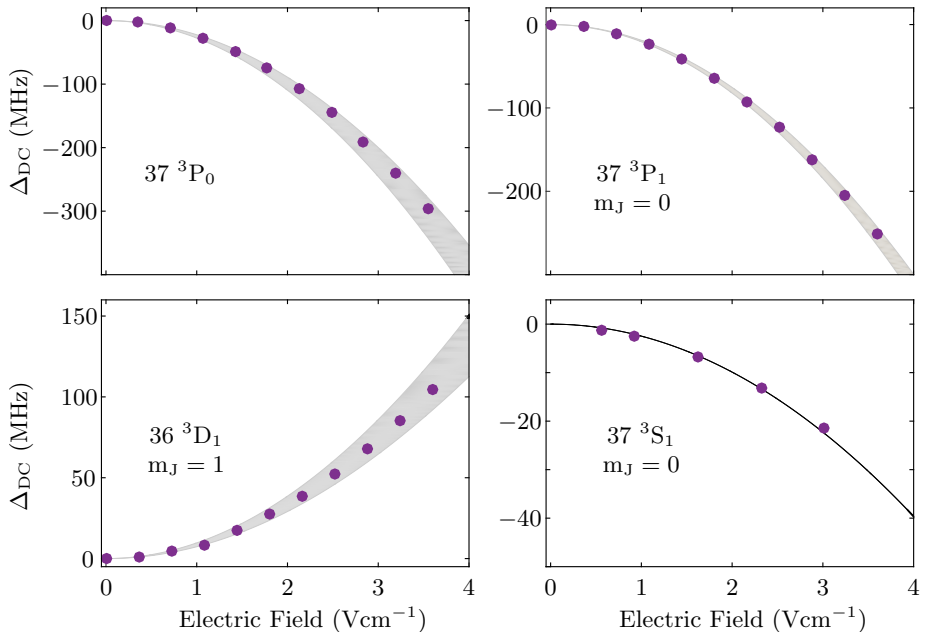

Figure 5.15: Predicted Stark shift (grey line) of the $37\ ^3P_0$, $37\ ^3P_1$ ($m_J = 0$), $36\ ^3D_1$ ($m_J = 1$) and $37\ ^3S_1$ ($m_J = 0$) Rydberg states. The shaded are represents the uncertainty arising from the experimental determination of the zero-field energy. Experimental data for each state is also shown (purple circles). Here a calibration factor of $0.36\,\mathrm{Vcm}^{-1}$ is used to convert the applied voltage to an electric field value.

ties. The theoretical uncertainty is indicated by the shaded band, and arises due to the uncertainty in the measured zero-field energies (table 5.4). The shaded region corresponds to the extremal cases where the 1-sigma errors on each series are combined to give the extremal overall polarisabilities. By performing improved Rydberg spectroscopy the uncertainty associated with the fitted quantum defect coefficients can be reduced. This would lead to a significant improvement in the calculated Stark maps and modeling of other Rydberg atom properties.

5.3.3 Future Measurements

The precision of our measurements to date are currently on the order of 10 kHz. However the linewidth of the Rydberg spectra could be reduced further in future measurements. This can be achieved by carrying out experiments in a narrow-band MOT, where the associated Doppler broadening

is $< 50\,\text{kHz}$. While Rydberg-Rydberg interactions causes additional spectral broadening, this can be eliminated by sufficiently reducing the number of excited Rydberg atoms.

From our earlier discussion of systematic uncertainties, methods for compensating stray magnetic and electric fields were outlined. Here we show that the associated shifts in the Rydberg energy levels are on the order of our statistical uncertainties, when optimally compensated. At this point the BBR energy shift of $2.4\,\text{kHz}$ [136] becomes comparable to other sources of error in the line position.

In summary, subsequent measurements using our apparatus should allow the Rydberg energy levels to be determined to $\sim 10\,\text{kHz}$. This provides an enhancement of more than three orders of magnitude over previous measured energy levels in strontium. Such significantly improved measurements would particularly be useful for quantum defect theories used to describe Rydberg atom properties.

Chapter 6

Rydberg Dressing in a MOT

In this chapter, the knowledge acquired over the course of this work is used to perform Rydberg dressing experiments in a narrow-line MOT. The results of this chapter have been published in [60]. For these experiments the MOT is first formed as described in chapter 3, and then an off-resonant Rydberg coupling laser is pulsed on for a time t_{d}, adding Rydberg character to the excited 5s5p $^3\mathrm{P}_1$ MOT state. The amount of Rydberg character in the MOT depends on the both the the Rabi-frequency Ω_{d} and the detuning Δ_{d} of the coupling laser.

For the first experiments on realising a Rydberg dressed MOT, I worked together with A. Bounds. Here we initially used the 5s36d $^3\mathrm{D}_1$ Rydberg state, for which the interactions are relatively weak [53]. At this state parameters of $\epsilon^2 = 0.03$ and $N_c \leq 0.5$, meant that the MOT was effectively in the non-interacting regime. This work showed that we were limited by atom loss during dressing, and further detail of the results in this regime can be found in the thesis of A. Bounds [91]. This thesis concentrates on measurements using the 5s36d $^3\mathrm{D}_2$ state for which we have stronger interactions. By working at this state we found that we could sufficiently reduce the atom loss. However we found the achievable densities, and hence N_c, were limited by the non-uniform intensity of the dressing beam. To enable the strongly interacting regime to be reached, the condition $V_{\mathrm{c}}/N_{\mathrm{c}} \geq \hbar\Gamma, k_{\mathrm{B}}T$ is required, with $N_{\mathrm{c}} > 1$ (see chapter 2).

6.1 Non-interacting regime

First experiments look at the characterisation of the dressed-MOT in the non-interacting regime, in particular:

- Observation of the AC Stark shift through changes in the MOT position.
- Proof of the added Rydberg character as the dressed atoms acquire a sensitivity to electric fields.
- A measurement of the dressed MOT temperature.
- A measurement of the trap lifetime in the dressed MOT.

6.1.1 Observation of a Rydberg dressed MOT

For the following results the Rydberg dressed MOT was formed by off-resonantly coupling the excited state $|\mathrm{e}\rangle = 5\mathrm{s}5\mathrm{p}\ {}^3\mathrm{P}_1$ to the Rydberg state $|r\rangle = 5\mathrm{s}36\mathrm{d}\ {}^3\mathrm{D}_1$ for which the interactions are weakly attractive [53]. Experimental parameters $\Omega_\mathrm{d}/2\pi = 4\,\mathrm{MHz}$ and $\Delta_\mathrm{d}/2\pi = 12\,\mathrm{MHz}$ give a dressing fraction of 3%, and $N_\mathrm{c} = 0.5$. As such the MOT is effectively in the the non-interacting regime.

Fig. 6.1 shows the effect of adding the coupling laser to the MOT. Fig. 6.1(a) is an image of the narrow-line MOT with no coupling laser applied, while in (b) the dressing laser was applied for a time $t_\mathrm{d} = 5\,\mathrm{ms}$. Continued trapping is observed on this timescale, however a consequence of applying the dressing laser is a significant shift in the vertical position. The shift is a result of the AC Stark shift, δ_ac. As the dressing laser is blue detuned from the Rydberg transition, the AC Stark shift results in the MOT transition shifting blue detuned compared to the bare transition. This increases the effective MOT beam detuning resulting in a larger MOT forming at lower vertical positions.

As the coupling laser is tightly focused on the MOT this vertical shift results in the MOT forming outside the dressing laser. This creates a potential

problem for experiments looking at the effects of dressed interactions over several ms. However we can eliminate the shift in position by adjusting δ during the dressing stage, such that we compensate for the change in detuning. A comparison of Fig. 6.1 (a) and (c) show this method is successful in keeping the MOT in its original position. In Fig. 6.1 (a) the undressed MOT is formed for $\delta/2\pi = -110\,\text{kHz}$. The calculated peak AC Stark shift from equation 2.14 is $\delta_{\text{ac}}/2\pi = 325\,\text{kHz}$, where the vertical shift is eliminated in Fig. 6.1 (c) for $\delta_{\text{ac}}/2\pi = 300\,\text{kHz}$. This corresponds to a MOT beam detuning $\delta/2\pi$ of 190 kHz, as is clear in Fig. 6.1 (d) which shows the position shift and atom number for different MOT beam detunings.

Of particular interest is the fact that at optimal compensation the cooling laser is blue-detuned with respect to the bare transition. As such the trap only operates in the presence of the coupling laser, trapping only the Rydberg-dressed atoms. Evidence of this is observed in Fig. 6.1 (c), where the undressed atoms outside the coupling beam are observed falling away, as they are no longer trapped.

6.1.2 Rydberg character

The result from Fig. 6.1 showed that the trap still operates when applying the coupling laser, and furthermore we can work in a regime where only the Rydberg dressed atoms are trapped. Here we demonstrate that even in the non-interacting case the dressed atoms acquire a Rydberg character. The experiment involved applying a static electric field in the horizontal (x, y) plane (30° angle to the coupling beam) during a dressing time $t_{\text{d}} = 10\,\text{ms}$. Here $\Delta_{\text{d}}/2\pi = 50\,\text{MHz}$ and $\Omega_{\text{d}}/2\pi$ is again 4 MHz. The results are shown in Fig. 6.2 and from the images (i) to (iv) it is clear that the dressed MOT is extremely sensitive to the applied DC electric field. This sensitivity is due to the high polarizability, α_{r}, of the Rydberg state. Importantly no effect is observed in the undressed MOT, and to our knowledge this is the first demonstration of an electric field sensitive MOT.

The underlying mechanism is understood by the Rydberg state DC Stark

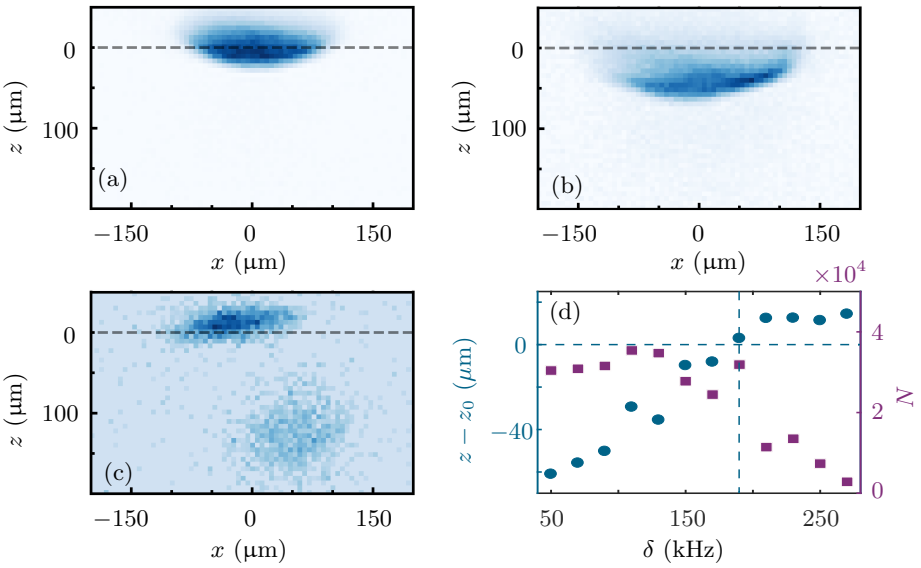

Figure 6.1: (a)-(c) are absorption images of the MOT with (a) no dressing beam, $\delta/2\pi$=−110 kHz, (b) 5 ms dressed MOT, $\Omega_d/2\pi$ = 4 MHz and $\Delta_d/2\pi$ = 12 MHz, (c) same parameters as in (b) but with $\delta/2\pi$=190 kHz while dressing. (d) shows the position shift (blue circles) and atom number (purple squares) for different compensated detunings, optimal compensated is denoted by the dashed lines.

shift, Δ_{DC}, translating as an AC Stark shift, δ_{ac}, of the dressed MOT excited state. The calculated Δ_{DC} for the Rydberg state is shown in Fig. 6.2(b). Due to the separation between the m_j states we find that resonance with the Rydberg state occurs at two electric fields where we strongly drive the transition, depleting the MOT. Images of the MOT close to resonance are shown in Fig. 6.2(a)(ii) and (iii). Here it is clear that atoms in the centre and wings of the cloud experience different coupling strengths due to the spatial inhomogeneity of the quadrupole field.

The dressed state picture remains valid away from resonance at both lower and higher electric field strengths (Fig. 6.2(a)(i)and (iv)). In this case, atoms in $|\tilde{e}\rangle$ acquire a polarizability given by $\alpha_e = \epsilon^2\alpha_r$. In Fig. 6.2 $\alpha_e \sim 10^{-33}\,\mathrm{cm^2V^{-1}}$ which is $\sim 10^5$ times larger than the bare 5s5p ^3P_J states [140, 141]. This change in δ_{ac} leads to a position shift of the MOT, forming at lower positions positions when $\delta_{ac} > 0$ and at higher positions when $\delta_{ac} < 0$ (i.e. at higher fields).

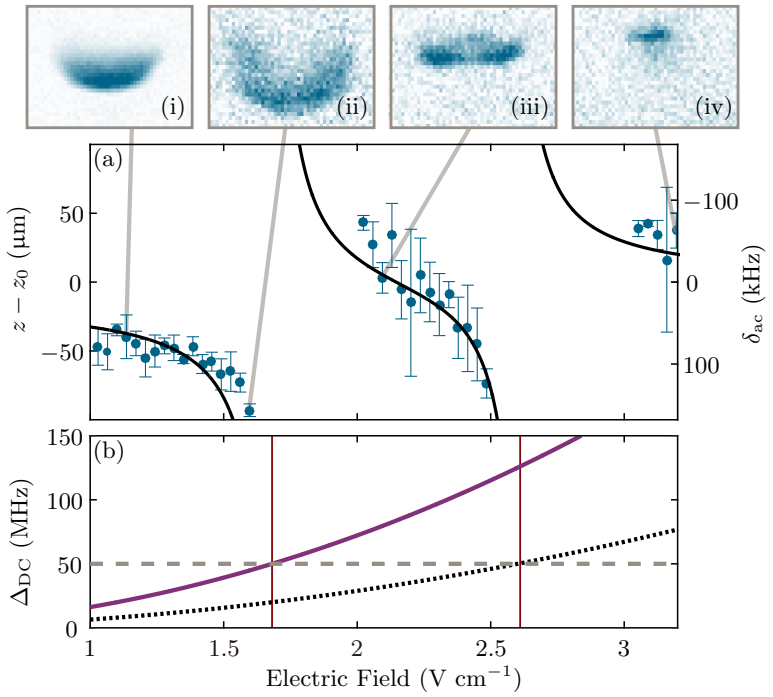

Figure 6.2: (a) The measured (blue circles) and predicted (black line) change in vertical MOT versus electric field with t_d=10 ms, $\Omega_d/2\pi$ = 50 MHz, and $\delta/2\pi$ = −110 kHz. Images (i)-(iv) show the MOT at fields of 1.1, 1.6, 2.1 and 3.2 V cm^{-1} respectively. (b) DC Stark shift of the $|m_J| = 1$ (dotted black line) and $|m_J| = 0$ (purple line) components of the 36d $^3D_1$ state. Dashed grey line indicates $\Delta_d/2\pi$ = 50 MHz.

The position shift shown in Fig. 6.2(a) is found to be in good agreement with a simple model. Here we calculate the AC Stark shift of the $^3P_1$ m_j states independently. As the MOT sags under gravity, atoms primarily experience a vertical magnetic and horizontal electric field, resulting in stronger Rydberg coupling to the 36d $|m_j| = 0$ state than the 36d $|m_j| = 1$ state due the polarisation of the laser beams [91]. Taking this into account in the model the coupling to the $|m_j| = 0$ state is weighted twice as strongly as the $|m_j|$ = 1 state.

More details on the electric field sensitive MOT can be found in [91]. These results highlight that a trap exists for all values of electric field for which the dressing beam is sufficiently far from resonance. The Rydberg-dressed MOT can thus be viewed as a novel type of hybrid trap whose size, shape and po-

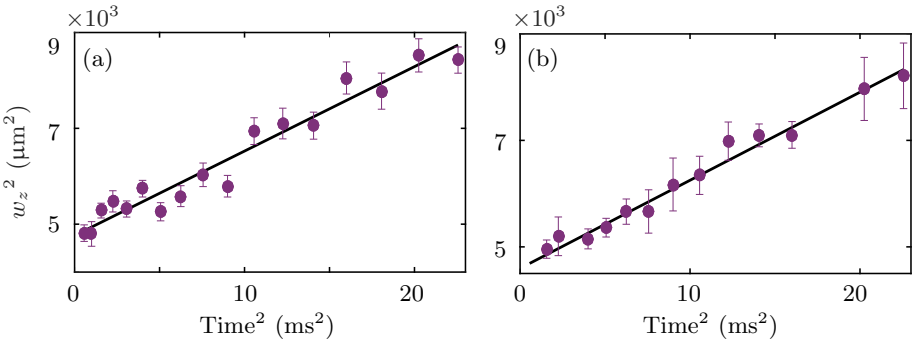

Figure 6.3: Ballistic expansion measurements in the undressed MOT (a) and after 4 ms of dressing (b). By fitting a straight line to the graph the temperature is obtained from equation 6.1.

sition can be controlled by a relatively weak electric as well as magnetic fields. This result could find applications in electrometry measurements using Rydberg states, for instance in optical lattice clocks [55].

6.1.3 Temperature

The dressed MOT temperature was measured to provide evidence that the atoms are laser cooled as well as trapped. A ballistic expansion measurement was taken for different dressing times, t_d, in a compensated dressed MOT, for the same parameters as in Fig. 6.1(c). For a ballistic expansion, all laser beams and fields are turned off following the experiment, and the temperature is determined through the rate of expansion following details in [142]. Here if the initial position is Gaussian, described by the standard deviation $\sigma_z(0)$, and the velocity distribution is Maxwellian, the expansion of the cloud with time follows the form

$$\sigma_z(t) = \sqrt{\sigma_z(0)^2 + \frac{k_\mathrm{B} T_z t^2}{m}}, \tag{6.1}$$

where T_z is the temperature.

An example of ballistic expansion measurements at t_d values of 0 ms and 4 ms, are shown in Fig. 6.3. The width the cloud is found by fitting the atom distribution to a Gaussian. The temperature can be then be calculated from the slope of the straight line fit using equation 6.1. By repeating

this measurement at different dressing times the evolution of the temperature as a function of t_d can be obtained, as shown in Fig. 6.4. Here the temperatures in both the vertical T_z and horizontal T_x direction are shown. As the fractional change in cloud size with expansion time is smaller in the horizontal direction, it results in larger uncertainties in T_x.

Both T_z and T_x are seen to increase after initially applying the dressing beam. This is due to the change in resonant position leading to heating. Once the atoms reach the new resonant position, subsequent cooling occurs. After 3 ms of dressing, T_z returns to 0.8 μK, which is the same temperature as the undressed MOT. The cooling rate for T_z is quicker than T_x, as the atoms predominately interact with the vertical MOT beam. In addition to a temperature change, we also observe a movement in the cloud position. A vertical shift of ∼15 μm is observed, which corresponds to the cloud reaching its new equilibrium position. However in the horizontal direction there is a ∼35 μm shift. We attribute this shift to the dressing beam alignement. If the dressing beam is not centered on the cloud, this leads to different AC Stark shifts on each side of the cloud. As a result there is stronger scattering from one direction, resulting in a net force on the cloud.

The data in Fig. 6.4 is compared to the Monte-Carlo MOT model, described in chapter 2. The simulation is in quantitative agreement with the experimental data T_z, where the only fit parameter was the position of the dressing beam relative to the center of the quadrupole magnetic field. In the horizontal direction there is less agreement between the simulation and the data. This is likely due to the large uncertainty in the coupling beam position and the ballistic expansion fits for T_x. From the Monte-Carlo MOT model we have studied the dependence of the temperature on the coupling beam alignment. As expected, we find that the heating is minimised for optimum alignment and compensation. From this we can conclude that the initial heating is due to the spatial dependence of the AC Stark shift, as the change in resonant position leads to increased scattering from the MOT beams. Subsequent cooling then occurs over the timescale taken for the MOT to reach equilibrium.

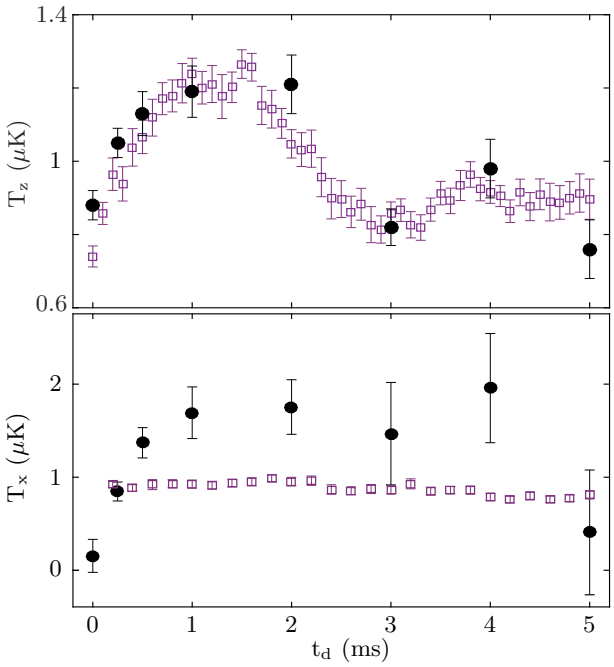

Figure 6.4: Measured (black circles) and simulated (purple squares) temperature in the vertical direction T_z (top) and horizontal direction T_x (bottom) for different dressing times t_d. Data was taken at the 36d $^3\mathrm{D}_1$ state for $\Omega_\mathrm{d}/2\pi = 4\,\mathrm{MHz}$ and $\Delta_\mathrm{d}/2\pi = 12\,\mathrm{MHz}$.

6.1.4 Lifetime

A measurement of the dressed MOT trap lifetime is important to ensure that a sufficient density is maintained over the timescale required for the MOT to reach equilibrium ($\sim 3\,\mathrm{ms}$, from Fig. 6.4). Additionally it is important for comparing with other dressing experiments in randomly distributed ensembles, where uncontrollable loss mechanisms have been observed [29–32]. In the absence of the dressing laser the narrow-line MOT has a trap lifetime on the order of tens of milliseconds. Applying the dressing laser introduces a number of new loss mechanisms. Additionally, we find the non-uniform AC Stark shift across the cloud, as a result of the Gaussian coupling beam, leads to an increase in atoms lost from the trap. Fig. 6.5 shows the atom number as a function of t_d for the same dressing parameters as in the previous sections. At short times rapid loss is observed with a decay constant of $0.4 \pm 0.1\,\mathrm{ms}$, followed by a slower exponential decay. The rapid loss results

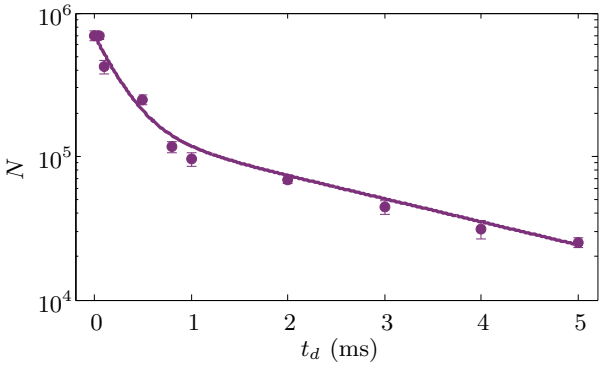

Figure 6.5: Atom number as a function of t_d showing the dressed MOT trap lifetime for the 36d $^3\mathrm{D}_1$ state. The line shows a double exponential fit to the data.

in a drop in the cloud density, which is a problem when moving towards experiments looking for observables of interactions.

An in-depth study of the short-term loss processes are discussed in [91]. There using time-resolved ion detection with a micro-channel plate, the loss is shown to be attributed to substantial ionisation and the formation of an ultra-cold plasma. At the current Rydberg state (5s36d $^3\mathrm{D}_1$), the DC Stark shift due to ions in the cloud has the same sign as the dressed laser detuning. Therefore the ion formation results in a frequency shift bringing the laser closer to resonance. Once a plasma threshold is reached, trapped electrons in the cloud lead to further ionization through collisions and a stronger DC Stark shift aiding in further loss. The details of this are not discussed in this thesis. Instead the focus is on methods for reducing this loss as we move towards experiments which attempt to measure dressed interaction effects.

6.2 Reducing Loss

In order to reach an interacting regime in the dressed MOT, the short-term loss due to plasma formation must be suppressed. Here we discuss methods for avoiding this loss, where two main approaches were successful in increasing the dressed MOT lifetime. The first approach was to apply an electric field in order to extract the ions, while the second is simply a more careful selection of Rydberg state.

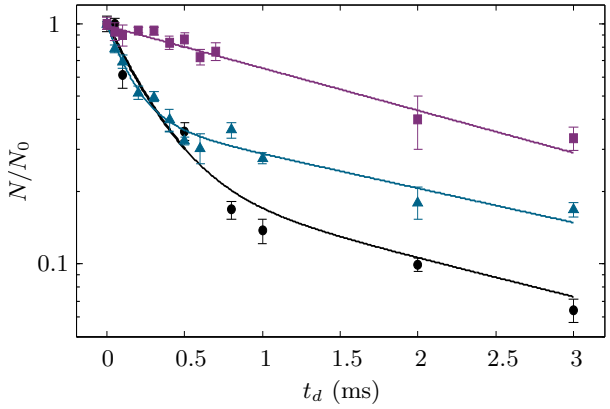

Figure 6.6: Trap lifetimes at the 36d $^3D_1$ state for different electric fields of $0\,\mathrm{Vcm^{-1}}$ (black circles), $1.75\,\mathrm{Vcm^{-1}}$ (blue triangles) and $5.25\,\mathrm{Vcm^{-1}}$ (purple squares). Fits to the data are two-term exponential for $0\,\mathrm{Vcm^{-1}}$ and $1.75\,\mathrm{Vcm^{-1}}$, and a single exponential at $5.25\,\mathrm{Vcm^{-1}}$.

6.2.1 Applying an electric Field

In our experiment, a plasma forms when the number of ions within the MOT volume reaches a critical threshold. Initially the spontaneously created electrons rapidly escape until there are enough cold ions present to trap the electrons. At this point, further created electrons are bound by the positive charge forming a plasma. By applying an electric field for the duration of the dressing experiment allows ions to be continuously extracted, making it harder to reach this threshold.

Fig. 6.6 shows the effect of applying a DC electric field to extract the ions, with the same Rydberg state and parameters as for previous data. The initial density in this case was $\sim 1 \times 10^{12}\,\mathrm{cm^3}$. The associated DC Stark shift was compensated by adjusting the frequency of the dressing laser to keep Δ_d constant. The field was applied in the horizontal plane at an angle of 30° to the coupling beam. Compared to the case with no field we clearly see an increase in the lifetime with increasing electric field.

While this method is successful in reducing the loss at short times, as discussed earlier in the chapter, the application of an electric field leads to atoms at different positions experiencing different coupling strengths. This

in turn leads to a change in the MOT shape. As a result it is more difficult to compensate for the AC Stark shift, and additionally the coupling strength could be reduced (as it is split across transitions). Therefore the increasing lifetime with electric field may be partially be attributed to this effect. As a result our preferred method to reduce the loss was instead to use a different Rydberg state.

6.2.2 Changing Rydberg state

For the previous experimental data the DC Stark shift due to ions in the cloud brings the dressing laser closer to resonance, resulting in enhanced Rydberg excitation. Therefore avoidance of this loss should be possible by choosing a state where the DC Stark shift is opposite in sign to the coupling laser detuning. The 5snd $^3D_2$ states for $n < 37$ satisfy this requirement, where the van der Waals interactions are repulsive [73] and the DC Stark shift is positive. Here any ion formation instead shifts atoms out of resonance with the red-detuned dressing laser.

However working with a red-detuned laser introduces a different problem, which requires understanding the impact of the dressing laser on the resonance condition of the MOT. The effect of the dressing laser when either red or blue detuned is highlighted in Fig. 6.7. The resonance condition of the MOT with no dressing laser applied is shown by the contours of constant energy in Fig. 6.7(a), forming an elliptical shell around the quadrupole centre. The application of the dressing beam induces a spatially dependent AC Stark shift of the MOT transition, due to its Gaussian intensity profile. This leads to a distortion of the elliptical energy contours, that is dependent on the sign of Δ_d. Fig. 6.7(b) and (c) show the energy contours for $\Delta_d < 0$ and $\Delta_d > 0$ respectively. For the case $\Delta_d < 0$, the resonance condition becomes shallower and 'double-welled', leading to a spreading of the MOT and a weakening of the confinement. Conversely for $\Delta_d > 0$, the resonance condition becomes more deeply furrowed, allowing for strong confinement and making it easier to maintain a compensated MOT. Therefore, before

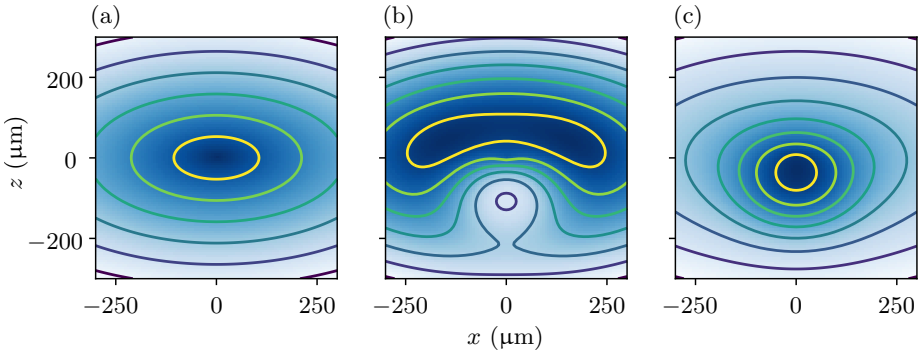

Figure 6.7: Contours of constant energy at 5s36d ^{3}D$_2$ of the $m_j = -1$ state in the presence of the magnetic quadrupole field, with a vertical gradient of $8\,\mathrm{Gcm}^{-1}$, for (a) the case of no dressing (b) dressing with $\Delta_\mathrm{d} < 0$ ($-12\,\mathrm{MHz}$) and (c) $\Delta_\mathrm{d} > 0$ ($12\,\mathrm{MHz}$).

performing experiments at the $^3D_2$ state, it was not clear whether it was possible to create a stable dressed MOT when $\Delta_\mathrm{d} < 0$.

The comparison of the trap lifetimes at the 5s36d ^{3}D$_1$ (as shown in Fig. 6.5) and the 5s36d ^{3}D$_2$ states are shown in Fig. 6.8. For the latter we clearly observe reduced trap loss at short times, where the fit gives a lifetime of $1.2 \pm 0.5\,\mathrm{ms}$ (compared to $0.4 \pm 0.1\,\mathrm{ms}$ at ^{3}D$_1$), and is significantly larger than the Rydberg state lifetime of $18 \pm 1\,\mu\mathrm{s}$. Experiments were carried both with and without an electric field at the ^{3}D$_2$ state where no effect on the loss was observed. This suggests the short-term decay is not due to ion creation. Instead the loss seems to be associated with the change in sign of AC Stark shift as shown in Fig. 6.7. This effect also limited the maximum interaction strength, because larger detunings were required to produce a stable MOT. Here we use $\Omega_\mathrm{d}/2\pi = 5\,\mathrm{MHz}$ and $\Delta_\mathrm{d}/2\pi = -30\,\mathrm{MHz}$.
The longer lifetime in Fig. 6.8 of $5 \pm 1\,\mathrm{ms}$ is comparable to the decay in the undressed MOT. Therefore these results show promise for reaching a regime where one could expect to observe dressed interactions.

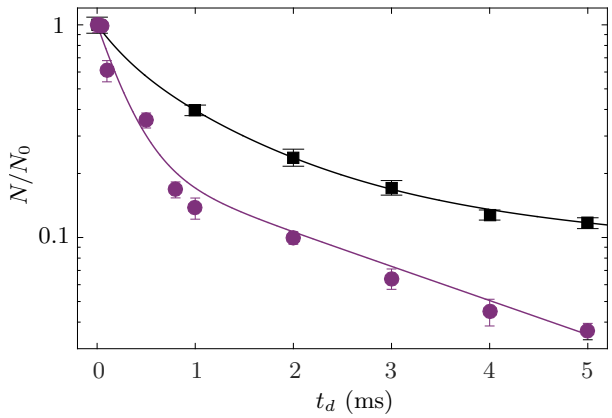

Figure 6.8: Normalised atom number $N/N_{\mathrm{t=0}}$ as a function of time for the 5s36d ^{3}D$_2$ Rydberg state (black squares), and the 5s36d ^{3}D$_1$ state (purple circles). The solid lines represent double exponential fits to the data.

6.3 Reaching the Interacting Regime

In the previous section the measured lifetimes of the dressed MOT were shown to be >1 ms, after eliminating loss due to ionisation by either applying an electric field, or using an appropriate Rydberg state. Here we discuss the selection of a Rydberg state for observing interactions, along with the experimental results and planned improvements for the future.

6.3.1 Selecting Rydberg States

For the 5s36d ^{3}D$_1$ Rydberg state (which was the main state used for investigations in the previous sections) the number of atoms per dressed blockade sphere (N_c, equation 2.17) was <1, hence we did not expect to see evidence of interaction effects. In selecting a Rydberg state for observing interactions we require $V/N_{\mathrm{c}} \geq \hbar\Gamma, k_{\mathrm{b}}T$, as discussed in chapter 2. Additionally, we require a $N_{\mathrm{c}} > 1$ to be maintained over the timescale associated with the atomic motion. Experiments looking for the effects of interactions were carried out at 5snd ^{3}D$_2$ states (for $n \leq 37$). The reason for choosing these states is the reduced loss discussed in the previous section, along with favorable dressing parameters which are are highlighted in Table. 6.1.

As shown in Table. 6.1 the C_6 coefficients at the 5snd ^{3}D$_2$ (for $n = 34 \rightarrow 37$)

State	$\Omega_d/2\pi$ (MHz)	$\Delta_d/2\pi$ (MHz)	V_0 (kHz)	C_6 (GHz μm^6)	R_c (μm)	N_c	Plasma Free?
36 ^{3}D$_1$	4	12	19	-0.115	1.3	0.5	×
50 ^{3}S$_1$	2	-6	9	24.5	3.6	13.2	×
34 ^{3}D$_2$	5	-30	3	0.32	1.3	0.7	✓
36 ^{3}D$_2$	5	-30	3	2.2	1.8	1.8	✓
37 ^{3}D$_2$	5	-30	3	446	4.4	25.2	✓

Table 6.1: Different Rydberg states used for our experiments with the values used to calculate the interaction strengths and the number of atoms per dressed blockade sphere at each state.

are larger than for the 5s36d ^{3}D$_1$ and of opposite sign. The increase in C_6 is due to a nearby Förster resonance at 5s37d ^{3}D$_2$, resulting in a larger R_c and $N_c > 1$ for our achievable densities.[1] Over the range of $n = 34 \rightarrow 37$, N_c varies from 0.7 to 25 allowing for comparisons between the interacting and non-interacting regime. Unfortunately due to the wavelength range of our UV laser system it is not possible to reach lower Rydberg states, and for $n > 37$ the interactions are repulsive.

Another option for increasing N_c, is to select a state with higher principal quantum number n, where values for the 5s50s ^{3}S$_1$ state are shown in Table. 6.1. However while N_c is larger, the Rabi frequency reduces with increasing n, and at the time these experiments were conducted we were limited by the amount of available UV power. A Rabi frequency of 2 MHz was measured for this state, hence for large enough interaction strengths a smaller detuning is needed, leading to more Rydberg loss. In Table. 6.1 a detuning of 6 MHz is considered giving the same Rydberg fraction as at 5s36d ^{3}D$_1$. As for the ^{3}D$_1$ states, the ^{3}S$_1$ series have a DC Stark shift that is the same sign as the dressed laser detuning, meaning an electric field is required for reducing short-term loss.

For these reasons the 5snd ^{3}D$_2$ states were selected, due to the encouraging

[1] The $n = 37$ state has a large and uncertain C_6 coefficient, due to a nearby Förster resonance.

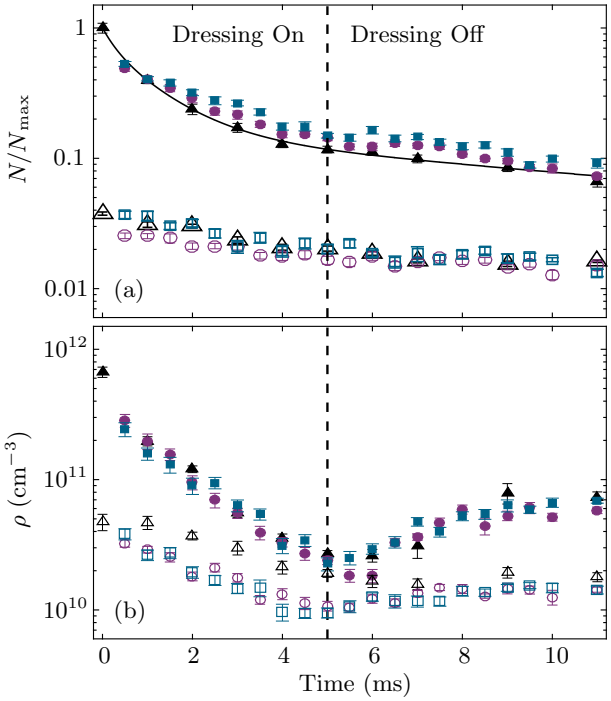

Figure 6.9: (a) Atom number as a function of time for three different states: 5s34d ^{3}D$_2$ (blue squares), 5s36d ^{3}D$_2$ (black triangles) and 5s37d ^{3}D$_2$ (purple circles). Different initial densities of $1 \times 10^{12}\,\mathrm{cm}^{-3}$ (filled data points) and $5 \times 10^{10}\,\mathrm{cm}^{-3}$ (hollow data points) are shown. The vertical dashed line indicates where the UV beam is turned off (after 5 ms). (b) Density as a function of time for the same states.

lifetimes already measured in section 6.2.2 in the absence of an electric field, along with the large change in N_c across the available n shown in Table. 6.1.

6.3.2 Experimental Results

Experiments were conducted for three Rydberg states: the 5s34d ^{3}D$_2$, 5s36d ^{3}D$_2$ and 5s37d ^{3}D$_2$ states. The dressing time t_d was varied from 1 to 5 ms, after which the dressing laser was switched off for a further 10 ms. The purpose of this was to return to a normal MOT after dressing to understand the effect of the coupling laser on the MOT shape. Here $\delta = -110\,\mathrm{kHz}$, and the AC Stark shift was compensated during the 5 ms of dressing to keep atoms in the UV beam. The dressing parameters used were $\Omega_d/2\pi = 5\,\mathrm{MHz}$ and $\Delta_d/2\pi = -30\,\mathrm{MHz}$. Any interaction effect should have a density

dependance, therefore the experiments were also conducted for a range of densities.

Fig. 6.9 shows the atom numbers and densities for both a high initial density of $1 \times 10^{12}\,\mathrm{cm}^{-3}$ and a lower density of $5 \times 10^{10}\,\mathrm{cm}^{-3}$. The y-axis in both graphs are plotted on a log scale, with the same overall range, highlighting the differences between atom loss and density loss mechanisms. Comparing Fig. 6.9(a) and (b) for the high density data (filled markers) there is clearly a density decay which is much quicker than the atom loss over the 5 ms of dressing. The decay is independent of principal quantum number, indicating that this effect is not caused by the dressed interaction as there is a large variation in N_c over this range of states (see Table. 6.1). After the dressing laser is switched off (denoted by the dashed lines in Fig. 6.9) the density is largely restored. In particular, after 5 ms it returns to the level you would expect from the atom number loss.

In Fig. 6.9(a) the atom number at high densities is fit to a two-term exponential giving lifetimes of 1.2 ± 0.7 ms and 5 ± 1 ms. For the low density data (hollow markers) a single exponential fits the data giving a lifetime 6.4 ± 0.8 ms. This reduced atom loss at low densities is accompanied by less density decay as seen in Fig. 6.9(b). Here applying the dressing laser does still have an effect on the low density MOT but not to the same extent as at high initial densities.

Fig. 6.10 shows the reason for the density decay, where images of the MOT are shown both with and without the coupling laser applied, for the 5s36d $^3\mathrm{D}_2$ state. For a high initial density (top row) there is a significant expansion of the cloud in the horizontal direction during dressing. Subsequently the UV is turned off, and the cloud returns to its original size. However interestingly this seems to be a density dependent effect. In the bottom row of Fig. 6.10 the initial density is lower and there the expansion in the horizontal direction is much less significant. For both densities shown the shape of the MOT changes on application of the dressing laser. Later we will show that this can be attributed to the the spatial inhomogeneity of the AC Stark shift due to the Gaussian intensity profile of the dressing

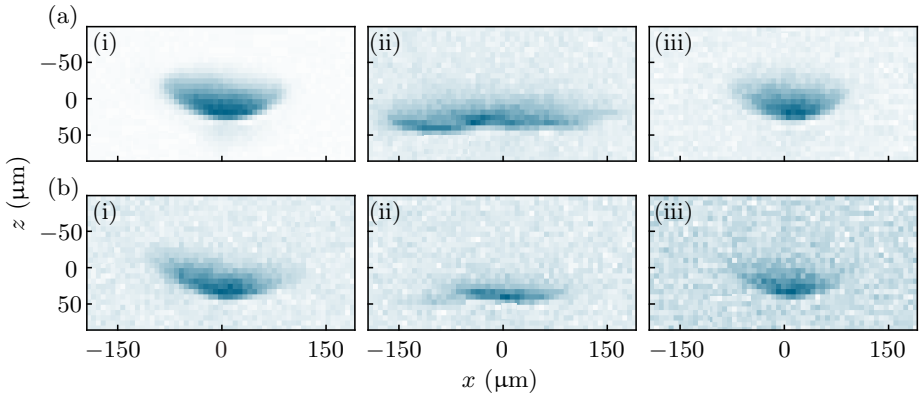

Figure 6.10: Images of the 5s36d $^3D_2$ MOT for (a) an an initial density of $1 \times 10^{12}\,\mathrm{cm}^{-3}$ and (b) an initial density of $5 \times 10^{10}\,\mathrm{cm}^{-3}$ where (i) no coupling laser applied (ii) t_d =5 ms and (iii) t_d =5 ms, then UV is turned off for 6 ms.

beam.

The effect on the MOT horizontal width w_x is shown in Fig. 6.11 by plotting w_x versus time for all three $^3D_2$ states considered in Fig. 6.9. For high densities the MOT expands to almost double its initial width over the 5 ms of dressing. However after removing the dressing laser the MOT width starts to reduce. In the high and low density cases, the final width of the cloud is the same, and is equivalent to the initial size of the low density cloud.

6.3.3 Radiation Pressure Effects

Our hypothesis is that the cloud expansion shown in Fig. 6.11 is caused by the deformation of the trap potential shown in Fig. 6.7, coupled with radiation pressure, which provides the driving force behind the expansion.
The signatures of radiation trapping have been studied in a number of experiments [143–148], where the re-absorption of spontaneously emitted photons results in a repulsive force between the atoms which limits the maximum achievable density. For MOTs formed on inter-combination lines (as in our experiment) there is a suppression of this effect due to the reduced scattering rate compared to that of conventional MOTs, leading to larger achievable densities. However at high enough densities a slow heating rate is observed, that is due to radiation trapping [35]. In order to estimate the magnitude

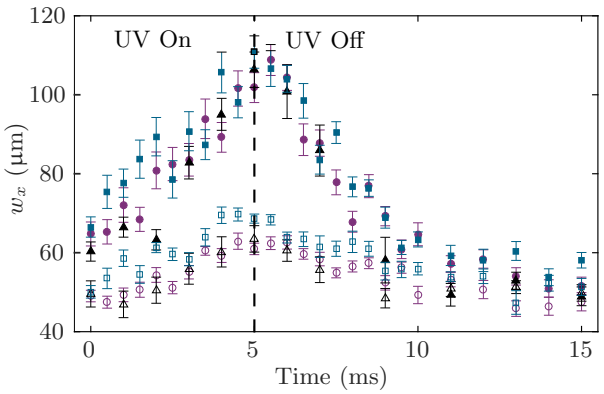

Figure 6.11: Dressed MOT width w_x as a function of time for three different states: 5s34d $^3D_2$ (blue squares), 5s36d $^3D_2$ (black triangles) and 5s37d $^3D_2$ (purple circles). Initial densities are $1 \times 10^{12}\,\mathrm{cm}^{-3}$ (filled markers) and $5 \times 10^{10}\,\mathrm{cm}^{-3}$ (hollow markers)

of the force of radiation trapping F_R in our MOT, the force between two atoms separated by a distance d as defined in [149, 150] is considered:

$$F_\mathrm{R} = \frac{\sigma_\mathrm{l}\sigma_\mathrm{r} I}{4\pi c d^2}, \tag{6.2}$$

where σ_l is the cross-section for absorption of a laser photon, σ_r a re-radiated photon and I is the beam intensity. We define σ_l using the on resonance cross-section, $\sigma_0 = 3\lambda^2/2\pi$,

$$\sigma_\mathrm{l} = \frac{\sigma_0}{1 + S + 4(\Delta/\Gamma)^2}. \tag{6.3}$$

From [149], the ratio $\sigma_\mathrm{r}/\sigma_\mathrm{l}$ can be determined from ρ_max, the maximum attainable density in the multiple scattering regime. Due to the repulsive force between the atoms at higher trap densities, the MOT radius is determined by the number of atoms N, rather than the temperature, and scales as $N^{1/3}$. Fig. 6.12(a) shows the undressed MOT volume (V) as a function of atom number. Here the increase in volume for atom numbers $> 2.5 \times 10^5$ indicates the onset of radiation trapping. As $\rho_\mathrm{max} \propto N/V$, fitting a straight line to the data in this regime predicts an $\rho_\mathrm{max} = 1.1 \pm 0.6 \times 10^{12}\,\mathrm{cm}^{-3}$. The cross section ratio can then be obtained from the relation [149]:

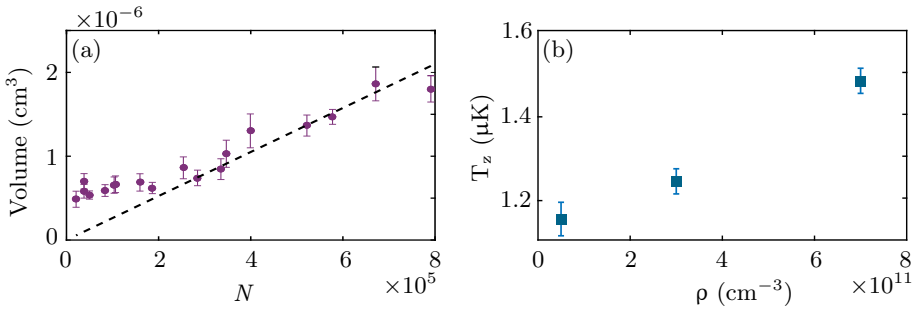

Figure 6.12: (a) MOT volume versus the number of trapped atoms (purple circles). Dashed line is a fit through the origin for atoms numbers $> 2.5 \times 10^5$. (b) MOT temperature as a function of density. In both graphs $\delta = -110\,\text{kHz}$ and the saturation parameter s is ~ 10

$$\rho_{\text{max}} = \frac{3\kappa c}{I_{\text{tot}}\sigma_{\text{l}}^2\,(\sigma_{\text{r}}/\sigma_{\text{l}} - 1)} \tag{6.4}$$

where σ_{l} is calculated from equation 6.3, and κ is the spring constant of the trap. This gives the value $\sigma_{\text{r}}/\sigma_{\text{l}} \sim 1$. Fig. 6.12(b) shows an increase in temperature of $0.3\,\mu\text{K}$ over a range ρ of $(1\text{–}7 \times 10^{11})\,\text{cm}^{-3}$, providing further evidence of radiation trapping. This is in agreement with data shown in [35].

The data in Fig. 6.12 shows that densities in the narrow-band MOT are high enough for radiation pressure effects to start altering the MOT dynamics. In the dressed MOT the radiation pressure force can dominate, due to the weakening trap confinement as a result of the Gaussian profile of the coupling beam (see Fig. 6.7).

For understanding why this is the case, a simple model of radiation pressure was developed. To a first approximation, the instantaneous 'switch-on' of the dressing beam means initially the atoms do not strongly interact with the MOT beams, due to the change in resonance condition (see Fig. 6.7). This implies that radiation pressure is the dominant force in the first $\sim 2\,\text{ms}$ and forces attributed to MOT beam scattering can be neglected. We simulate the initial expansion of the MOT whilst dressing using a simple one-dimensional model which is based upon equation 6.2. Initially we use a normal distribution of atoms with a $1/e^2$ radius of $60\,\mu\text{m}$, similar to the

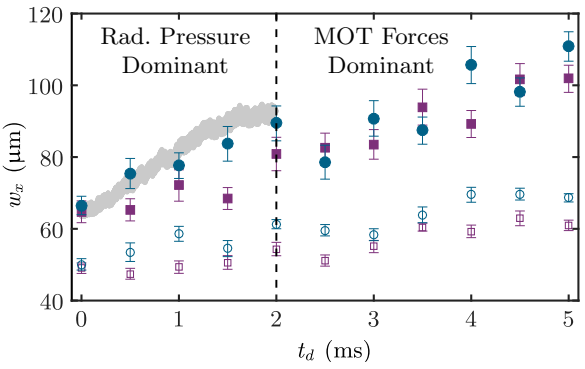

Figure 6.13: Dressed MOT width w_x plotted as a function of dressing time t_d for the 5s34d $^3D_2$ (blue circles) and 5s37d $^3D_2$ (purple squares) at high (filled markers) and low (hollow markers) initial densities. Also shown is the cloud width determined from the model (grey) as described in the text.

experimentally measured value. The total simulation is broken down into a series of time steps. At each time-step, we calculate the force and velocity of each atom due to the presence of all others. The atoms are then allowed to evolve following Newtonian dynamics, before the force is re-calculated. At each time step, the position of the atoms is recorded from which the width of the resulting distribution is measured.

Fig. 6.13 shows the widths produced by the model along with the experimental data. We find a similar expansion rate of the atoms in the first 2 ms, compared to the experimentally measured widths, w_x, of the high density MOT. For a low initial density the increase in width is much less significant, but at longer times as MOT forces become dominant we see similar gradients at both low and high densities. As a result this provides evidence that the decay in density is a result of radiation trapping along with the weakening confinement for a red-detuned coupling laser.

6.3.4 Outlook

The results shown give evidence that due to the rapid density decay while dressing we can not observe the effects of interactions. The achievable values for the density (hence N_c) along with the interaction strength V_c, are both limited by the combination of radiation pressure and the non-uniform

intensity of the dressing beam. However these results are still encouraging as the loss is not due to Rydberg excitation, as confirmed from the measured trap lifetimes. A clear solution to overcome the current limitation in density and interaction strength is to use commercially available beam shapers to produce a uniform intensity profile of the dressing beam. This would allow improved compensation, reducing radiation pressure effects by creating a trap potential matching that of the undressed MOT and may also result in less atom loss at short times. Importantly, this upgrade means larger interaction strengths V_c could be achieved, as there would no longer be a weakening of the MOT confinement when compensating for the AC Stark shift. Therefore the coupling beam parameters Ω_d and Δ_d would no longer be limited by this effect.

As mentioned in chapter 4, an upgrade to the current 319 nm laser system from using a PPLST crystal to a PPLN crystal would result in ~ 1 W UV power. If using a flat top beam with a size of $300\times100\,\mu$m, 1 W of UV power would correspond to $\Omega_d/2\pi = 16$ MHz, for the $^3D_2$ states considered in this section. Therefore interaction strengths where $V_c/N_c \geq \hbar\Gamma, k_bT$ should be easily achievable. These upgrades are currently been added to the experiment, allowing further Rydberg dressing experiments looking at the effects of interactions in the future. As discussed in chapter 2 the interactions should result in a position shift in the MOT, as predicted through our mean-field model. Additionally we expect to be able to measure beyond mean-field effects, where it is not clear what effect will dominant the MOT behaviour. The strong correlations in the scattering of neighbouring atoms may lead to spatial and dynamical effects not captured by the mean-field model. More information is again given at the end of chapter 2, where in the future we hope our experimental results should answer some of these open questions.

Chapter 7

Conclusions and Outlook

7.1 Overview

The work of this thesis has demonstrated new and improved methods of Rydberg spectroscopy and Rydberg dressing in strontium. Both objectives required first developing a laser source at 319 nm, for Rydberg excitation from the 5s5p $^3P_1$ state. In chapter 4 we show that the resulting laser system was suitable for our requirements. In particular the laser system allows excitation to a large range of Rydberg states in the triplet series of strontium, with a sufficiently narrow laser linewidth, and powers of > 200 mW. By using this laser source, methods were then developed for performing Rydberg spectroscopy in a MOT. Experiments were carried out for a MOT formed on the $5s^2\ ^1S_0 \rightarrow 5s5p\ ^3P_1$ transition. Chapter 5 presents our results for precision measurements of the Rydberg states, along with a characterisation of the states through a variety of measurements (e.g. Rydberg state lifetimes and autoionisation spectra). Recently, precision Rydberg spectroscopy has been significantly improved by measuring against a frequency comb, while for a MOT formed on the narrow-line transition in strontium, we can obtain Rydberg spectra with widths of < 300 kHz. This combination allows us to determine the line centre of the spectrum with a precision on the order of 10 kHz. While clearly systematic uncertainties limit the overall accuracy of our measurements to date, we outline future procedures that can

reduce the error to a similar level as our statistical uncertainties. This compares well to current state of the art frequency measurements of Rydberg energies [42, 43]. Furthermore, in comparison to previous measurements in strontium, this technique should provide absolute frequencies with uncertainties improved by approximately three orders of magnitude [46–52].

Following our discussion on Rydberg spectroscopy, we then move towards describing experiments which focus on Rydberg dressing in a narrow-line MOT. This work provide the world's first demonstration of Rydberg dressed laser cooling, and provides strong evidence that the interacting regime can be reached. An overview of our scheme for Rydberg dressing is introduced in chapter 2, and the experimental results are then presented in chapter 6. This work in particular builds on the thesis of A. Bounds [91], where details are given on our understanding of a non-interacting dressed MOT. By building on this knowledge we find methods for reducing the loss that before limited the dressed MOT lifetime. Much longer lifetimes have now been observed as shown in chapter 6. However rather than atom loss, we find that the cloud expands during dressing, reducing the density below that required for strong interactions. Through analysis of the data we find that the cloud expansion is due to combined effects of radiation pressure and the non-uniform AC Stark shift, which results from the Gaussian profile of the coupling beam. Fortunately there are clear solutions to prevent this by acquiring beam shaping optics which instead produce a coupling beam with uniform intensity.

7.2 Future Directions

Over the last year the experiment has been upgraded extensively during a laboratory move, producing a more reliable experiment. From the results produced in this work there are a number of obvious paths for future directions of the project. However, in addition to these experiments, the upgrades should allow the research group to investigate other research areas.

Firstly, in terms of Rydberg spectroscopy there are a number of straight-

forward objectives for future experiments. By using the new electrode configuration, which is now a hexagonal split ring rather than a set of four pairs, any stray DC fields can be eliminated using the technique highlighted in chapter 5. In addition to the DC fields, any stray magnetic field will also compensated. Following compensation of any stray fields that can shift the line, a comprehensive study of the Rydberg series can be completed. Our 319 nm laser will allow us to measure across a large range of principal quantum number, and the unprecedented precision we can achieve permits detailed study of the quantum defects. As pointed out in chapter 5 there is little known about the autoionisation spectra of the triplet Rydberg series. Therefore further study into MQDT fitting of the spectra across a range of Rydberg series could also prove to be a area of future interest. As the experimental chamber now includes a pair of in-vacuum lenses, the group is moving towards dipole trapping of strontium. The addition of a dipole trap may also aid in spectroscopy measurements, increasing the rate at which spectroscopy can be performed.

From the experimental results on a Rydberg dressed MOT there are also obvious planned objectives. Initially we will add beam shaping optics to the Rydberg coupling laser, creating a uniform intensity beam. At the same time the SFG crystal will be switched to PPLN, to achieve larger powers at 638 nm and hence in the UV. With these improvements it should be possible to reach the interacting regime for Rydberg states considered in chapter 6. Furthermore, due to the higher frequency stability of the MOT light after incorporating the new ULE cavity into our experimental set-up, less jitter is observed in the MOT position on shot-to-shot runs of the experiment. This means that any interaction observable should be easier to detect, in particular any position shifts, which we expect to be on the order of the cloud width. Other observables which could be observed include temperature changes or modifications in the MOT shape, as discussed in chapter 2. As the next generation of the experiment is moving towards dipole trapping of the cloud, the dipole trap laser will allow magic wavelength trapping on either the $5s^2\ {}^1S_0 \rightarrow 5s5p\ {}^3P_1$ or $5s5p\ {}^3P_0$ transitions. Using a similar

one-photon dressing scheme as in the MOT, spin-squeezing experiments in a dipole trap as proposed in [24] can be investigated in the future. This would have applications in high precision frequency metrology, improving the performance of atomic lattice clocks. Other directions include exploring charge and excitation-hopping by moving to an array of single atoms.

In conclusion, the advantages of studying Rydberg physics using divalent electron atoms show promise for a wide variety of novel and interesting research. There are many areas of research to explore in the future, which can build upon the work in this thesis.

Appendix A

Fits to autoioinising spectra

In chapter 5, two-channel MQDT theory was used for describing an autoionising spectrum. This appendix gives a brief overview of MQDT theory, before showing the resulting fit parameters for the spectra. The two-channel theory was found to be over-simplistic in most cases. Details on why this is the case, along with future methods to fully describe the autoionization process are also given.

A.1 Two-channel MQDT

Here a short introduction to MQDT theory is provided, where a more complete review can be found in [134]. Previous work studying the autoionising series of strontium is described several publications [82, 135, 151]. The isolated core excitation (ICE) scheme we use is shown in Fig. A.1. For a two-channel MQDT model we consider an autoioninzing channel (channel 1) which is coupled to the continuum (channel 2). An atom is initially in a 5snl Rydberg state, with a bound state effective quantum number ν_b, that depends on the bound state quantum defect δ_b. Using a laser at 408 nm the atom is excited from the Rydberg state to the autoioninsing series $5p_{3/2}nl$. The energy of the state is given by the quasibound channel effective quantum number ν_a, that depends on the quasibound channel quantum defect δ_a. Note that the effective quantum number is a continuous variable defined

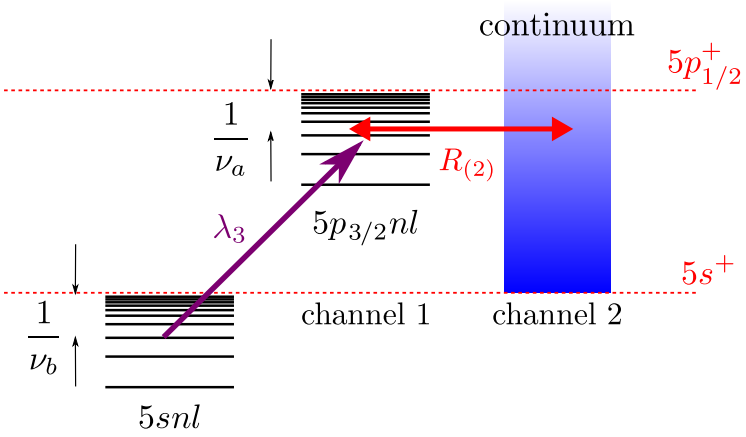

Figure A.1: A two-channel MQDT model for isolated core excitation in strontium. The atom is excited from a Rydberg state 5snl to an autoionizing state $5p_{3/2}nl$, which is coupled to the continuum. Figure taken from [82]

as:

$$\nu = \sqrt{\frac{R_{\mathrm{Sr}}}{E_{\mathrm{ion}} - E}}, \tag{A.1}$$

where R_{Sr} is the Rydberg constant for strontium, E_{ion} the ionisation limit, and E the energy of the excitation laser.

The optical cross, σ, for the autoionisation process, where a single autoionizing state is coupled to the continuum, has the following form [151]:

$$\sigma = \frac{4\pi^2\omega}{c} |Z|^2 |\langle \nu_a l | \nu_b l \rangle|^2 \left| \left\langle 5p || \hat{T} || 5s \right\rangle \right|^2, \tag{A.2}$$

where $\langle \nu_a l | \nu_b l \rangle$ is the overlap integral for the Rydberg electron, Z the density of the autoionising states, ω the optical frequency of the transition and $\hat{T}$ is the transition dipole operator. Note that here the reduced dipole matrix-element for the inner valence electron transition ($\left\langle 5p || \hat{T} || 5s \right\rangle$) is a constant. The overlap integral is given by the following equation [152]:

$$\langle \nu_a l | \nu_b l \rangle = \frac{2{\nu_a}^2{\nu_b}^2}{\pi\left({\nu_a}^2 - {\nu_b}^2\right)} \sin\left[\pi\left(\nu_{\mathrm{a}} - \nu_{\mathrm{b}}\right)\right]. \tag{A.3}$$

Note that the above equation is different from the expression obtained in

[152] by a factor of $(\nu_a\nu_b)^{1/3}$ due to different normalizations of the wave functions [153].

The density of the autoionising states, Z, in equation **??** is described by the following equation [3]:

$$Z^2 = \frac{R^2\left(1+\tan^2\left[\pi\left(\nu_\mathrm{a}+\delta_\mathrm{a}\right)\right]\right)}{R^4+\tan^2\left[\pi\left(\nu_\mathrm{a}+\delta_\mathrm{a}\right)\right]}. \tag{A.4}$$

Here R is the is the coupling between the quasibound (autoionizing) channel and the continuum, given by the non-zero R matrix element [151].

Therefore when producing fits to the data the three fit parameters required are A, R and δ_a. The autoionising spectra shown in this thesis (see chapter 5) plot the ion signal versus the frequency of the 408 nm light. The shape of such an autoionising spectrum depends on the difference $\delta_a - \delta_b$ as shown in [82]. In general if $\delta_a = \delta_b$ there is a single dominant peak, as the outer electron wavefunction for a 5snl Rydberg state only has significant overlap with one $5p_{3/2}nl$ autoionising state. However when the outer electron wavefunction overlaps with two autoionising states i.e. $\delta_a - \delta_b = 0.5$, then a double peaked structure is observed.

A.2 Fit Parameters

Referring back to Fig. 5.10 in chapter 5, the fit to the experimental data for the 5s37s $^3S_1$ spectrum, using equation A.2, is shown by the solid black line. The fit gives the coupling parameter $R = 0.32$ and autoionising quantum defect $\delta_a = 3.39$. This fit agrees well with the data, where the FWHM

$$\Gamma_a = \frac{2R^2}{\pi {\nu_a}^3} \tag{A.5}$$

has a value of 5.6 GHz. The other state shown in Fig. 5.10 (5s37p $^3P_0$) cannot be described by the two-channel model outlined in this appendix. Here two autoionising peaks are observed showing a separation of ~ 20 GHz. As already mentioned, increasing the difference in the quantum defects δ_a

and δ_b can produce two peaks in the model. However when changing the value of δ_a to obtain two peaks, we find it still does not agree with the experimental data, as it results in a separation between the peaks of $\sim$ 150 GHz.

In conclusion more channels should be added to the model for describing the spectrum. This was also the case for previous work on singlet Rydberg states [82, 135], where a total of six channels were required to reproduce the autoionization spectra. Six channels would require more free parameters to be included in the fit, as all the coupling parameters R_{ij} between channels i and j need to be considered, along with the quantum defects for the different quasibound channels. While these values can be constrained for the singlet states from previous experimental studies [135, 151], this is not the case for the triplet Rydberg series. Therefore possible future work could look at performing a comprehensive experimental study for such autoionising spectra.

Bibliography

[1] J. R. Rydberg. Xxxiv. on the structure of the line-spectra of the chemical elements. *The London, Edinburgh, and Dublin Philosophical Magazine and Journal of Science*, 29(179):331–337, 1890.

[2] H.E. White. *Introduction to atomic spectra*. International series in pure and applied physics. McGraw-Hill book company, inc., 1934.

[3] Thomas F. Gallagher. *Rydberg Atoms*. Cambridge Monographs on Atomic, Molecular and Chemical Physics. Cambridge University Press, 1994.

[4] C. E. Wieman, D. E. Pritchard, and D. J. Wineland. Atom cooling, trapping, and quantum manipulation. *Rev. Mod. Phys.*, 71:S253–S262, 1999.

[5] H. J. Metcalf and P. van der Straten. Laser cooling and trapping of atoms. *J. Opt. Soc. Am. B*, 20(5):887–908, 2003.

[6] W. R. Anderson, J. R. Veale, and T. F. Gallagher. Resonant dipole-dipole energy transfer in a nearly frozen Rydberg gas. *Phys. Rev. Lett.*, 80:249–252, 1998.

[7] M. D. Lukin, M. Fleischhauer, R. Cote, L. M. Duan, D. Jaksch, J. I. Cirac, and P. Zoller. Dipole blockade and quantum information processing in mesoscopic atomic ensembles. *Phys. Rev. Lett.*, 87:037901, 2001.

[8] H. Labuhn, D. Barredo, S. Ravets, S. de Léséleuc, T. Macri, T. Lahaye,

and A. Browaeys. Tunable two-dimensional arrays of single rydberg atoms for realizing quantum ising models. *Nature*, 534, 2016.

[9] H. Bernien, S. Schwartz, A. Keesling, H. Levine, A. Omran, H. Pichler, S. Choi, A. Zibrov, M. Endres, M. Greiner, V. Vuletic, and M. D. Lukin. Probing many-body dynamics on a 51-atom quantum simulator. *Nature*, 551, 2017.

[10] L. Isenhower, E. Urban, X. L. Zhang, A. T. Gill, T. Henage, T. A. Johnson, T. G. Walker, and M. Saffman. Demonstration of a neutral atom controlled-not quantum gate. *Phys. Rev. Lett.*, 104:010503, 2010.

[11] M. Saffman, T. G. Walker, and K. Mølmer. Quantum information with rydberg atoms. *Rev. Mod. Phys.*, 82:2313–2363, 2010.

[12] T. Wilk, A. Gaëtan, C. Evellin, J. Wolters, Y. Miroshnychenko, P. Grangier, and A. Browaeys. Entanglement of two individual neutral atoms using rydberg blockade. *Phys. Rev. Lett.*, 104:010502, 2010.

[13] J. D. Pritchard, D. Maxwell, A. Gauguet, K. J. Weatherill, M. P. A. Jones, and C. S. Adams. Cooperative atom-light interaction in a blockaded rydberg ensemble. *Phys. Rev. Lett.*, 105:193603, 2010.

[14] Y. O. Dudin and A. Kuzmich. Strongly interacting rydberg excitations of a cold atomic gas. *Science*, 336:887–9, 2012.

[15] O. Firstenberg, C. S. Adams, and S. Hofferberth. Nonlinear quantum optics mediated by rydberg interactions. *J. Phys. B: At., Mol. Opt. Phys.*, 49(15):152003, 2016.

[16] T. Peyronel, O. Firstenberg, Q.-Y. Liang, S. Hofferberth, A. Gorshkov, T. Pohl, M. D. Lukin, and V. Vuletic. Quantum nonlinear optics with single photons enabled by strongly interacting atoms. *Nature*, 488:57–60, 2012.

[17] D. Maxwell, D. J. Szwer, D. Paredes-Barato, H. Busche, J. D. Pritchard, A. Gauguet, K. J. Weatherill, M. P. A. Jones, and C. S.

Adams. Storage and control of optical photons using rydberg polaritons. *Phys. Rev. Lett.*, 110:103001, 2013.

[18] N. Henkel, R. Nath, and T. Pohl. Three-dimensional roton excitations and supersolid formation in rydberg-excited bose-einstein condensates. *Phys. Rev. Lett.*, 104:195302, 2010.

[19] G. Pupillo, A. Micheli, M. Boninsegni, I. Lesanovsky, and P. Zoller. Strongly correlated gases of rydberg-dressed atoms: Quantum and classical dynamics. *Phys. Rev. Lett.*, 104:223002, 2010.

[20] M. Boninsegni and N. V. Prokof'ev. Colloquium: Supersolids: What and where are they? *Rev. Mod. Phys.*, 84:759–776, 2012.

[21] F. Maucher, N. Henkel, M. Saffman, W. Królikowski, S. Skupin, and T. Pohl. Rydberg-induced solitons: Three-dimensional self-trapping of matter waves. *Phys. Rev. Lett.*, 106:170401, 2011.

[22] R. M. W. van Bijnen and T. Pohl. Quantum magnetism and topological ordering via rydberg dressing near förster resonances. *Phys. Rev. Lett.*, 114:243002, 2015.

[23] A. W. Glaetzle, M. Dalmonte, R. Nath, C. Gross, I. Bloch, and P. Zoller. Designing frustrated quantum magnets with laser-dressed rydberg atoms. *Phys. Rev. Lett.*, 114:173002, 2015.

[24] L. I. R. Gil, R. Mukherjee, E. M. Bridge, M. P. A. Jones, and T. Pohl. Spin squeezing in a rydberg lattice clock. *Phys. Rev. Lett.*, 112:103601, 2014.

[25] Isabelle Bouchoule and Klaus Mølmer. Spin squeezing of atoms by the dipole interaction in virtually excited rydberg states. *Phys. Rev. A*, 65:041803, 2002.

[26] Y.-Y. Jau, A. M. Hankin, T. Keating, I. H. Deutsch, and G. W. Biedermann. Entangling atomic spins with a rydberg-dressed spin-flip blockade. *Nat. Phys.*, 12:71, 2015.

[27] J. Zeiher, R. van Bijnen, P. Schauß, S. Hild, J.-Y. Choi, T. Pohl, I. Bloch, and C. Gross. Many-body interferometry of a Rydberg-dressed spin lattice. *Nat. Phys.*, 12:1095–1099, 2016.

[28] J. Zeiher, J.-Y. Choi, A. Rubio-Abadal, T. Pohl, R. van Bijnen, I. Bloch, and C. Gross. Coherent many-body spin dynamics in a long-range interacting ising chain. *Phys. Rev. X*, 7:041063, 2017.

[29] J. A. Aman, B. J. DeSalvo, F. B. Dunning, T. C. Killian, S. Yoshida, and J. Burgdörfer. Trap losses induced by near-resonant rydberg dressing of cold atomic gases. *Phys. Rev. A*, 93:043425, 2016.

[30] E. A. Goldschmidt, T. Boulier, R. C. Brown, S. B. Koller, J. T. Young, A. V. Gorshkov, S. L. Rolston, and J. V. Porto. Anomalous broadening in driven dissipative rydberg systems. *Phys. Rev. Lett.*, 116:113001, 2016.

[31] S. Helmrich, A. Arias, and S. Whitlock. Scaling of a long-range interacting quantum spin system driven out of equilibrium. *ArXiv e-prints, arXiv:1605.08609*, 2016.

[32] T. Boulier, E. Magnan, C. Bracamontes, J. Maslek, E. A. Goldschmidt, J. T. Young, A. V. Gorshkov, S. L. Rolston, and J. V. Porto. Spontaneous avalanche dephasing in large rydberg ensembles. *Phys. Rev. A*, 96:053409, 2017.

[33] F. B. Dunning, T. C. Killian, S. Yoshida, and J. Burgdörfer. Recent advances in Rydberg physics using alkaline-earth atoms. *J. Phys. B: At., Mol. Opt. Phys.*, 49(11):112003, 2016.

[34] A. V. Taichenachev, V. I. Yudin, C. W. Oates, C. W. Hoyt, Z. W. Barber, and L. Hollberg. Magnetic field-induced spectroscopy of forbidden optical transitions with application to lattice-based optical atomic clocks. *Phys. Rev. Lett.*, 96:083001, 2006.

[35] H.i Katori, T. Ido, Y. Isoya, and M. Kuwata-Gonokami. Magneto-

optical trapping and cooling of strontium atoms down to the photon recoil temperature. *Phys. Rev. Lett.*, 82:1116–1119, 1999.

[36] G. Lochead, D. Boddy, D. P. Sadler, C. S. Adams, and M. P. A. Jones. Number-resolved imaging of excited-state atoms using a scanning autoionization microscope. *Phys. Rev. A*, 87:053409, 2013.

[37] P. McQuillen, X. Zhang, T. Strickler, F. B. Dunning, and T. C. Killian. Imaging the evolution of an ultracold strontium rydberg gas. *Phys. Rev. A*, 87:013407, 2013.

[38] R Mukherjee, J Millen, R Nath, M P A Jones, and T Pohl. Many-body physics with alkaline-earth rydberg lattices. *J. Phys. B: At., Mol. Opt. Phys.*, 44(18):184010, 2011.

[39] F Robicheaux. Transfer of a wavepacket between atoms. *Journal of Physics B: Atomic, Molecular and Optical Physics*, 43(21):215004, 2010.

[40] Th. Udem, R. Holzwarth, and T. W. Hänsch. Optical frequency metrology. *Nature*, 416(6877):233–237, 2002.

[41] Arman Cingoz, Dylan Yost, Thomas Allison, Axel Ruehl, Martin Fermann, Ingmar Hartl, and Jun Ye. Direct frequency comb spectroscopy in the extreme ultraviolet. *Nature*, 482:68–71, 2012.

[42] J. Deiglmayr, H. Herburger, H. Saßmannshausen, P. Jansen, H. Schmutz, and F. Merkt. Precision measurement of the ionization energy of cs i. *Phys. Rev. A*, 93:013424, 2016.

[43] Wenhui Li, I. Mourachko, M. W. Noel, and T. F. Gallagher. Millimeter-wave spectroscopy of cold rb rydberg atoms in a magneto-optical trap: Quantum defects of the ns, np, and nd series. *Phys. Rev. A*, 67:052502, 2003.

[44] N. Watanabe, H. Tamura, M. Musha, and K. Nakagawa. Optical frequency synthesizer for precision spectroscopy of rydberg states of rb atoms. *Jpn. J. Appl. Phys.*, 56(11):112401, 2017.

[45] Markus Mack, Florian Karlewski, Helge Hattermann, Simone Höckh, Florian Jessen, Daniel Cano, and József Fortágh. Measurement of absolute transition frequencies of ^{87}Rb to nS and nD rydberg states by means of electromagnetically induced transparency. *Phys. Rev. A*, 83:052515, 2011.

[46] R. Beigang, K. Lücke, D. Schmidt, A. Timmermann, and P. J. West. One-photon laser spectroscopy of rydberg series from metastable levels in calcium and strontium. *Phys. Scr.*, 26(3):183, 1982.

[47] J R Rubbmark and S A Borgström. Rydberg series in strontium found in absorption by selectively laser-excited atoms. *Phys. Scr.*, 18(4):196, 1978.

[48] J. A. Armstrong, J. J. Wynne, and P. Esherick. Bound, odd-parity j = 1 spectra of the alkaline earths: Ca, Sr, and Ba. *J. Opt. Soc. Am.*, 69(2):211–230, 1979.

[49] Peter Esherick. Bound, even-parity $j = 0$ and $j = 2$ spectra of Sr. *Phys. Rev. A*, 15:1920–1936, 1977.

[50] R. Beigang and D. Schmidt. Two-channel mqdt analysis of bound 5 snd 3 d 1,3 rydberg states of strontium. *Phys. Scr.*, 27(3):172, 1983.

[51] C. J. Dai. Perturbed $5snd^{1,3}d_2$ rydberg series of Sr. *Phys. Rev. A*, 52:4416–4424, 1995.

[52] P. Esherick, J. J. Wynne, and J. A. Armstrong. Spectroscopy of 3p0 states of alkaline earths. *Opt. Lett.*, 1(1):19–21, 1977.

[53] C. L. Vaillant, M. P. A. Jones, and R. M. Potvliege. Long-range rydberg–rydberg interactions in calcium, strontium and ytterbium. *J. Phys. B: At., Mol. Opt. Phys.*, 45(13):135004, 2012.

[54] C. L. Vaillant, M. P. A. Jones, and R. M. Potvliege. Multichannel quantum defect theory of strontium bound Rydberg states. *J. Phys. B: At., Mol. Opt. Phys.*, 47(15):155001, 2014.

[55] W. Bowden, R. Hobson, P. Huillery, P. Gill, M. P. A. Jones, and I. R. Hill. Rydberg electrometry for optical lattice clocks. *Phys. Rev. A*, 96:023419, 2017.

[56] Jean-Philippe Uzan. The fundamental constants and their variation: observational and theoretical status. *Rev. Mod. Phys.*, 75:403–455, 2003.

[57] C. Gaul, B. J. DeSalvo, J. A. Aman, F. B. Dunning, T. C. Killian, and T. Pohl. Resonant rydberg dressing of alkaline-earth atoms via electromagnetically induced transparency. *Phys. Rev. Lett.*, 116:243001, 2016.

[58] E. M. Bridge, N. C. Keegan, A. D. Bounds, D. Boddy, D. P. Sadler, and M. P. A. Jones. Tunable CW UV laser with<35 khz absolute frequency instability for precision spectroscopy of Sr Rydberg states. *Opt. Express*, 24(3):2281–2292, 2016.

[59] R. Kliese, N. Hoghooghi, T. Puppe, F. Rohde, A. Sell, A. Zach, P. Leisching, W. Kaenders, N. C. Keegan, A. D. Bounds, E. M. Bridge, J. Leonard, C. S. Adams, S. L. Cornish, and M. P.A. Jones. Difference-frequency combs in cold atom physics. *Euro. Phys., Special Topics*, 225(15):2775–2784, 2016.

[60] A. D. Bounds, N. C. Jackson, R. K. Hanley, R. Faoro, E. M. Bridge, P. Huillery, and M. P. A. Jones. Rydberg-dressed magneto-optical trap. *Phys. Rev. Lett.*, 120:183401, 2018.

[61] Y. Castin, H. Wallis, and J. Dalibard. Limit of doppler cooling. *J. Opt. Soc. Am. B*, 6(11):2046–2057, 1989.

[62] T. H. Loftus, T. Ido, M. M. Boyd, A. D. Ludlow, and J. Ye. Narrow line cooling and momentum-space crystals. *Phys. Rev. A*, 70:063413, 2004.

[63] R. K. Hanley, P. Huillery, N. C. Keegan, A. D. Bounds, D. Boddy, R. Faoro, and M. P. A. Jones. Quantitative simulation of a magneto-

optical trap operating near the photon recoil limit. *J. Mod. Opt.*, 0(0):1–10, 2017.

[64] N. Bohr. I. on the constitution of atoms and molecules. *The London, Edinburgh, and Dublin Philosophical Magazine and Journal of Science*, 26(151):1–25, 1913.

[65] I. S. Lim, J. K. Laerdahl, and P. Schwerdtfeger. The static electric dipole polarizability of rb +. *J. Phys. B: At., Mol. Opt. Phys.*, 33(3):L91, 2000.

[66] D. Tong, S. M. Farooqi, J. Stanojevic, S. Krishnan, Y. P. Zhang, R. Côté, E. E. Eyler, and P. L. Gould. Local blockade of rydberg excitation in an ultracold gas. *Phys. Rev. Lett.*, 93:063001, 2004.

[67] J. Honer, H. Weimer, T. Pfau, and H. P. Büchler. Collective many-body interaction in rydberg dressed atoms. *Phys. Rev. Lett.*, 105:160404, 2010.

[68] J. E. Johnson and S. L. Rolston. Interactions between rydberg-dressed atoms. *Phys. Rev. A*, 82:033412, 2010.

[69] J. B. Balewski, A. T. Krupp, A. Gaj, S. Hofferberth, R. Löw, and T. Pfau. Rydberg dressing: understanding of collective many-body effects and implications for experiments. *New J. Phys.*, 16(6):063012, 2014.

[70] B. J. DeSalvo, J. A. Aman, C. Gaul, T. Pohl, S. Yoshida, J. Burgdörfer, K. R. A. Hazzard, F. B. Dunning, and T. C. Killian. Rydberg-blockade effects in autler-townes spectra of ultracold strontium. *Phys. Rev. A*, 93:022709, 2016.

[71] L.A. Girifalco. *Statistical Mechanics of Solids*. Monographs on the Physics & Ch. Oxford University Press, USA, 2003.

[72] S. Chandrasekhar. Stochastic problems in physics and astronomy. *Rev. Mod. Phys.*, 15:1–89, 1943.

[73] C. Vaillant. *Long-Range Interactions in One- and Two-Electron Rydberg Atoms.* PhD thesis, Durham University, 2014.

[74] T. Macri and T. Pohl. Rydberg dressing of atoms in optical lattices. *Phys. Rev. A*, 89:011402, 2014.

[75] M. Genkin, S. Wuster, S. Mobius, A. Eisfeld, and J. M. Rost. Dipole–dipole induced global motion of rydberg-dressed atom clouds. *J. Phys. B: At., Mol. Opt. Phys.*, 47(9):095003, 2014.

[76] L. F. Buchmann, K. M'olmer, and D. Petrosyan. Creation and transfer of nonclassical states of motion using rydberg dressing of atoms in a lattice. *Phys. Rev. A*, 95:013403, 2017.

[77] N. Malossi, M. M. Valado, S. Scotto, P. Huillery, P. Pillet, D. Ciampini, E. Arimondo, and O. Morsch. Full counting statistics and phase diagram of a dissipative rydberg gas. *Phys. Rev. Lett.*, 113:023006, 2014.

[78] M. Marcuzzi, E. Levi, S. Diehl, J. P. Garrahan, and I. Lesanovsky. Universal nonequilibrium properties of dissipative rydberg gases. *Phys. Rev. Lett.*, 113:210401, 2014.

[79] H. Weimer, M. Müller, I. Lesanovsky, P. Zoller, and H.P. Büchler. A rydberg quantum simulator. *Phys. Rev. Lett.*, 113:210401, 2014.

[80] B. Zhao, A. W. Glaetzle, G. Pupillo, and P. Zoller. Atomic rydberg reservoirs for polar molecules. *Phys. Rev. Lett.*, 108:193007, 2012.

[81] U. Vogl and M. Weitz. Laser cooling by collisional redistribution of radiation. *Nature*, 461:70–73, 2009.

[82] James Millen. *A cold strontium Rydberg gas.* PhD thesis, Durham University, 2011.

[83] G. Lochead. *Excited state spatial distributions in a cold strontium gas.* PhD thesis, Durham University, 2012.

[84] D. Boddy. *First observations of Rydberg blockade in a frozen gas of divalent atoms.* PhD thesis, Durham University, 2014.

[85] D. Sadler. *Many-Body Interactions in a Dissipative Frozen Strontium Rydberg Gas.* PhD thesis, Durham University, 2016.

[86] C. J. Dedman, J. Nes, T. M. Hanna, R. G. Dall, K. G. H. Baldwin, and A. G. Truscott. Optimum design and construction of a zeeman slower for use with a magneto-optic trap. *Rev. Sci. Instrum.*, 75(12):5136–5142, 2004.

[87] D. J. McCarron, S. A. King, and S. L. Cornish. Modulation transfer spectroscopy in atomic rubidium. *Meas. Sci. Technol.*, 19(10):105601, 2008.

[88] M Boyd. *High Precision Spectroscopy of Strontium in an Optical Lattic: Towards a New Standard for Frequency and Time.* PhD thesis, Colorado University, 2007.

[89] P. G. Mickelson, Y. N. Martinez de Escobar, P. Anzel, B. J. DeSalvo, S. B. Nagel, A. J. Traverso, M. Yan, and T. C. Killian. Repumping and spectroscopy of laser-cooled Sr atoms using the (5s5p) 3 p 2 –(5s4d) 3 d 2 transition. *J. Phys. B: At. Mol. Opt. Phys.*, 42(23):235001, 2009.

[90] N. Poli, R. E. Drullinger, G. Ferrari, J. Léonard, F. Sorrentino, and G. M. Tino. Cooling and trapping of ultracold strontium isotopic mixtures. *Phys. Rev. A*, 71:061403, 2005.

[91] A. Bounds. *A Rydberg-dressed Magneto Optical Trap.* PhD thesis, Durham University, 2017.

[92] R. W. P. Drever, J. L. Hall, F. V. Kowalski, J. Hough, G. M. Ford, A. J. Munley, and H. Ward. Laser phase and frequency stabilization using an optical resonator. *Appl. Phys. B*, 31:97, 1983.

[93] E. D. Black. An introduction to Pound-Drever-Hall laser frequency stabilization. *American journal of physics*, 69:79, 2001.

[94] E. C. Cook, P. J. Martin, T. L. Brown-Heft, J. C. Garman, and D. A. Steck. High passive-stability diode-laser design for use in atomic-physics experiments. *Rev. Sci. Instrum.*, 83(4):043101, 2012.

[95] W. E. Cooke, T. F. Gallagher, S. A. Edelstein, and R. M. Hill. Doubly excited autoionizing rydberg states of Sr. *Phys. Rev. Lett.*, 40:178–181, 1978.

[96] X. Xu, T. H. Loftus, M. J. Smith, J. L. Hall, A. Gallagher, and J. Ye. Dynamics in a two-level atom magneto-optical trap. *Phys. Rev. A*, 66:011401, 2002.

[97] G. Reinaudi, T. Lahaye, Z. Wang, and D. Guéry-Odelin. Strong saturation absorption imaging of dense clouds of ultracold atoms. *Opt. Lett.*, 32(21):3143–3145, 2007.

[98] A. G˙ℓ-state selective field ionization of rubidium rydberg states. *Phys. Lett. A*, 324(4):315 – 320, 2004.

[99] A. C. Wilson, C. Ospelkaus, A. P. VanDevender, J. A. Mlynek, K. R. Brown, D. Leibfried, and D. J. Wineland. A 750 mw, continuous-wave, solid-state laser source at 313 nm for cooling and manipulating trapped 9be+ ions. *Appl. Phys. B*, 105(4):741–748, 2011.

[100] L. E. Myers and W. R. Bosenberg. Periodically poled lithium niobate and quasi-phase-matched optical parametric oscillators. *IEEE Journal of Quantum Electronics*, 33(10):1663–1672, 1997.

[101] A. Bruner, D. Eger, M. B. Oron, P. Blau, M. Katz, and S. Ruschin. Temperature-dependent sellmeier equation for the refractive index of stoichiometric lithium tantalate. *Opt. Lett.*, 28(3):194–196, 2003.

[102] G. D. Boyd and D. A. Kleinman. Parametric interaction of focused gaussian light beams. *J. Appl. Phys.*, 39(8):3597–3639, 1968.

[103] D. S. Hum, R. K. Route, G. D. Miller, V. Kondilenko, A. Alexandrovski, J. Huang, K. Urbanek, R. L. Byer, and M. M. Fejer. Optical properties and ferroelectric engineering of vapor-transport-equilibrated, near-stoichiometric lithium tantalate for frequency conversion. *J. Appl. Phys.*, 101(9):093108, 2007.

[104] S. Sinha, D. S. Hum, K. E. Urbanek, Y. Lee, M. J. F. Digonnet, M. M. Fejer, and R. L. Byer. Room-temperature stable generation of 19 watts of single-frequency 532-nm radiation in a periodically poled lithium tantalate crystal. *J. Lightwave Technol.*, 26(24):3866–3871, 2008.

[105] M. Katz, R. K. Route, D. S. Hum, K. R. Parameswaran, G. D. Miller, and M. M. Fejer. Vapor-transport equilibrated near-stoichiometric lithium tantalate for frequency-conversion applications. *Opt. Lett.*, 29(15):1775–1777, 2004.

[106] A. C. Wilson, C. Ospelkaus, A. P. VanDevender, J. A. Mlynek, K. R. Brown, D. Leibfried, and D. J. Wineland. A 750-mw, continuous-wave, solid-state laser source at 313 nm for cooling and manipulating trapped 9be+ ions. *Appl. Phys. B*, 105(4):741–748, 2011.

[107] D. L. Hart, L. Goldberg, and W. K. Burns. Red light generation by sum frequency mixing of er/yb fibre amplifier output in qpm linbo3. *Electron. Lett.*, 35(1):52–53, 1999.

[108] K. Kitamura, Y. Furukawab, S. Takekawa, M. Nakamura, A. Alexandrovski, and M.M. Fejer. Optical damage and light-induced absorption in near-stoichiometric litao3 crystal. In *Conference on Lasers and Electro-Optics*. Optical Society of America, 2001.

[109] R. Y. Chiao, C. H. Townes, and B. P. Stoicheff. Stimulated brillouin scattering and coherent generation of intense hypersonic waves. *Phys. Rev. Lett.*, 12:592–595, 1964.

[110] P. Dainese and J. C. Knight G .S. Wiederhecker H. L. Fragnito V. Laude A. Khelif P. St. J. Russell, N. Joly. Stimulated brillouin scattering from multi-ghz-guided acoustic phonons in nanostructured photonic crystal fibres. *Nat. Phys.*, 2:388–392, 2006.

[111] J.-C. Beugnot, T. Sylvestre, D. Alasia, H. Maillotte, V. Laude, A. Monteville, L. Provino, N. Traynor, S. Foaleng Mafang, and

L. Thévenaz. Complete experimental characterization of stimulated brillouin scattering in photonic crystal fiber. *Opt. Express*, 15(23):15517–15522, 2007.

[112] I. Bongrand, É. Picholle, and C. Montes. Coupled longitudinal and transverse stimulated brillouin scattering in single-mode optical fibers. *Eur. Phys. D.*, 20(1):121–127, 2002.

[113] J. I. Thorpe, K. Numata, and J. Livas. Laser frequency stabilization and control through offset sideband locking to optical cavities. *Opt. Express*, 16(20):15980–15990, 2008.

[114] H. Ludvigsen, M. Tossavainen, and M. Kaivola. Laser linewidth measurements using self-homodyne detection with short delay. *Opt. Commun.*, 155(1):180 – 186, 1998.

[115] D. Fehrenbacher, P. Sulzer, A. Liehl, T. Kälberer, C. Riek, D. V. Seletskiy, and A. Leitenstorfer. Free-running performance and full control of a passively phase-stable er:fiber frequency comb. *Optica*, 2(10):917–923, 2015.

[116] MenloSystems. *FC1500 Optical Frequency synthesizer operator manual*. Menlo systems GmbH.

[117] S. Rausch, T. Binhammer, A. Harth, J. Kim, R. Ell, F. X. Kärtner, and U. Morgner. Controlled waveforms on the single-cycle scale from a femtosecond oscillator. *Opt. Express*, 16(13):9739–9745, 2008.

[118] L. Xu, G. Tempea, A. Poppe, M. Lenzner, C. Spielmann, F. Krausz, A. Stingl, and K. Ferencz. High-power sub-10-fs ti:sapphire oscillators. *Appl. Phys. B*, 65(2):151–159, 1997.

[119] A. Sell, G. Krauss, R. Scheu, R. Huber, and A. Leitenstorfer. 8-fs pulses from a compact er:fiber system: quantitative modeling and experimental implementation. *Opt. Express*, 17(2):1070–1077, 2009.

[120] K. Tamura, E. P. Ippen, H. A. Haus, and L. E. Nelson. 77-fs pulse generation from a stretched-pulse mode-locked all-fiber ring laser. *Opt. Lett.*, 18(13):1080–1082, 1993.

[121] R. Holzwarth, Th. Udem, T. W. Hänsch, J. C. Knight, W. J. Wadsworth, and P. St. J. Russell. Optical frequency synthesizer for precision spectroscopy. *Phys. Rev. Lett.*, 85:2264–2267, 2000.

[122] T. Fuji, A. Apolonski, and F. Krausz. Self-stabilization of carrier-envelope offset phase by use of difference-frequency generation. *Opt. Lett.*, 29(6):632–634, 2004.

[123] Jackson Labs Technologies. *Fury User Manual. Version 1.2.*

[124] W.-K. Lee, D.-S. Yee, and H. S. Suh. Direct frequency counting with enhanced beat signal-to-noise ratio for absolute frequency measurement of a he-ne/i2 laser at 633 nm. *Appl. Opt.*, 46(6):930–934, 2007.

[125] D. W. Allan. Statistics of atomic frequency standards. *Proceedings of the IEEE*, 54(2):221–230, 1966.

[126] W.J. Riley, Physics Laboratory (U.S.). Time, and Frequency Division. *Handbook of Frequency Stability Analysis.* U.S. Department of Commerce, National Institute of Standards and Technology, 2008.

[127] J.A. Barnes. *NBS Technical Note 375.*

[128] L.-S. Ma, P. Jungner, J. Ye, and J. L. Hall. Delivering the same optical frequency at two places: accurate cancellation of phase noise introduced by an optical fiber or other time-varying path. *Opt. Lett.*, 19(21):1777–1779, 1994.

[129] S. M. Foreman, A. D. Ludlow, M. H. G. de Miranda, J. E. Stalnaker, S. A. Diddams, and J. Ye. Coherent optical phase transfer over a 32-km fiber with 1 s instability at 10^{-17}. *Phys. Rev. Lett.*, 99:153601, 2007.

[130] N. R. Newbury, P. A. Williams, and W. C. Swann. Coherent transfer of an optical carrier over 251 km. *Opt. Lett.*, 32(21):3056–3058, 2007.

[131] H. Jiang, F. Kéfélian, S. Crane, O. Lopez, M. Lours, J. Millo, D. Holleville, P. Lemonde, Ch. Chardonnet, A. Amy-Klein, and G. Santarelli. Long-distance frequency transfer over an urban fiber link using optical phase stabilization. *J. Opt. Soc. Am. B*, 25(12):2029–2035, 2008.

[132] S. H. Autler and C. H. Townes. Stark effect in rapidly varying fields. *Phys. Rev.*, 100:703–722, 1955.

[133] F. Camargo, J. D. Whalen, R. Ding, H. R. Sadeghpour, S. Yoshida, J. Burgdörfer, F. B. Dunning, and T. C. Killian. Lifetimes of ultra-long-range strontium rydberg molecules. *Phys. Rev. A*, 93:022702, 2016.

[134] M. Aymar, C. H. Greene, and E. Luc-Koenig. Multichannel rydberg spectroscopy of complex atoms. *Rev. Mod. Phys.*, 68:1015–1123, 1996.

[135] E. Y. Xu, Y. Zhu, O. C. Mullins, and T. F. Gallagher. Sr 5pnd j=3 autoionizing series and interference of excitation due to bound-state perturbation. *Phys. Rev. A*, 35:1138–1148, 1987.

[136] L. Hollberg and J. L. Hall. Measurement of the shift of Rydberg energy levels induced by blackbody radiation. *Phys. Rev. Lett.*, 53:230–233, 1984.

[137] H. Saßmannshausen, F. Merkt, and J. Deiglmayr. High-resolution spectroscopy of rydberg states in an ultracold cesium gas. *Phys. Rev. A*, 87:032519, 2013.

[138] M. L. Zimmerman, M. G. Littman, M. M. Kash, and D. Kleppner. Stark structure of the rydberg states of alkali-metal atoms. *Phys. Rev. A*, 20:2251–2275, 1979.

[139] J. Millen, G. Lochead, G. R. Corbett, R. M. Potvliege, and M. P. A. Jones. Spectroscopy of a cold strontium rydberg gas. *J. Phys. B: At., Mol. Opt. Phys.*, 44(18):184001, 2011.

[140] T. Middelmann, S. Falke, C. Lisdat, and U. Sterr. High accuracy correction of blackbody radiation shift in an optical lattice clock. *Phys. Rev. Lett.*, 109:263004, 2012.

[141] J. A. Sherman, N. D. Lemke, N. Hinkley, M. Pizzocaro, R. W. Fox, A. D. Ludlow, and C. W. Oates. High-accuracy measurement of atomic polarizability in an optical lattice clock. *Phys. Rev. Lett.*, 108:153002, 2012.

[142] K. Weatherill. *A CO_2 laser lattice experiment for cold atoms.* PhD thesis, Durham University, 2007.

[143] K. R. Overstreet, P. Zabawa, J. Tallant, A. Schwettmann, and J. P. Shaffer. Multiple scattering and the density distribution of a cs mot. *Opt. Express*, 13(24):9672–9682, 2005.

[144] C. G. Townsend, N. H. Edwards, C. J. Cooper, K. P. Zetie, C. J. Foot, A. M. Steane, P. Szriftgiser, H. Perrin, and J. Dalibard. Phase-space density in the magneto-optical trap. *Phys. Rev. A*, 52:1423–1440, 1995.

[145] M. Drewsen, Ph. Laurent, A. Nadir, G. Santarelli, A. Clairon, Y. Castin, D. Grison, and C. Salomon. Investigation of sub-doppler cooling effects in a cesium magneto-optical trap. *Appl. Phys. B*, 59:283–298, 1994.

[146] S Grego, M Colla, A Fioretti, J.H Müller, P Verkerk, and E Arimondo. A cesium magneto-optical trap for cold collisions studies. *Opt. Commun.*, 132(5):519 – 526, 1996.

[147] C. Gabbanini, A. Evangelista, S. Gozzini, A. Lucchesini, A. Fioretti, J. H. Müller, M. Colla, and E. Arimondo. Scaling laws in magneto-optical traps. *EPL*, 37(4):251, 1997.

[148] A. Vorozcovs, M. Weel, S. Beattie, S. Cauchi, and A. Kumarakrishnan. Measurements of temperature scaling laws in an optically dense magneto-optical trap. *J. Opt. Soc. Am. B*, 22(5):943–950, 2005.

[149] D. W. Sesko, T. G. Walker, and C. E. Wieman. Behavior of neutral atoms in a spontaneous force trap. *J. Opt. Soc. Am. B*, 8(5):946–958, 1991.

[150] A. M. Steane, M. Chowdhury, and C. J. Foot. Radiation force in the magneto-optical trap. *J. Opt. Soc. Am. B*, 9(12):2142–2158, 1992.

[151] E. Y. Xu, Y. Zhu, O. C. Mullins, and T. F. Gallagher. Sr $5p_{1/2}\mathrm{ns}_{1/2}$ and $5p_{3/2}\mathrm{ns}_{1/2}$ j=1 autoionizing states. *Phys. Rev. A*, 33:2401–2409, 1986.

[152] S. A. Bhatti, C. L. Cromer, and W. E. Cooke. Analysis of the rydberg character of the $5d7d^1d_2$ state of barium. *Phys. Rev. A*, 24:161–165, 1981.

[153] N. H. Tran, P. Pillet, R. Kachru, and T. F. Gallagher. Multistep excitation of autoionizing rydberg states. *Phys. Rev. A*, 29:2640–2650, 1984.